# DEVELOPMENT AND APPLICATIONS OF FLUORESCENT CORE-SHELL SILICA NANOPARTICLES FOR BIOIMAGING AND SENSING

A Dissertation

Presented to the Faculty of the Graduate School

of Cornell University

In Partial Fulfillment of the Requirements for the Degree of

Doctor of Philosophy

by

Andrew Arthur Burns

January 2009

# DEVELOPMENT AND APPLICATIONS OF FLUORESCENT CORE-SHELL SILICA NANOPARTICLES FOR BIOIMAGING AND SENSING

Andrew Arthur Burns, Ph. D.

Cornell University 2009

Nano-sized fluorescent materials have demonstrated great potential in the emergent fields of nanobiotechnology and nanomedicine. To create effective probes for these applications, high brightness, photostability and size control are key parameters for particle design. Core-shell silica nanoparticles incorporating covalently bound dyes in the particle core have been shown to exhibit significant enhancements in dye brightness and photostability while allowing independent control of particle size, color and surface chemistry.

Building on this platform, the first part of this dissertation explores a family of quantitative chemical sensors based on the incorporation of analyte-sensitive dyes into the particle shell. By co-localizing sensor and reference dye molecules onto a single particle, local analyte concentration changes can be discerned from local sensor concentration variations by comparison of the sensor and reference intensities facilitating quantitative "ratiometric" chemical imaging. The core-shell architecture is ideal for this application because it sequesters the reference dye in the particle core, while allowing analyte interactions with the sensor dyes near the particle surface. Traditional Stöber-derived sol-gel routes as well as reverse micelle-based methods were employed to generate pH- and $Ca^{+2}$-sensitive nanoparticles. Specific sensor architectures were applied to intracellular as well as large-scale functional volumetric imaging of intact biofilms and their metabolic activities.

To fully realize the potential of fluorescent nanomaterials for biomedical applications, one of the key obstacles is clearance from the body. The second part of this dissertation investigates several of the key parameters for effective clearance (size and surface chemistry) and highlights the development of a series of particles capable of rapid and efficient bodily clearance and demonstrates their efficacy in mice as a model system.

## BIOGRAPHICAL SKETCH

Andrew grew up on the North Shore of Long Island, New York, attending pre- and elementary school in Port Washington before moving further east to Greenlawn, NY where he attended Oldfield Middle and Harborfields High Schools. Andrew had many of the classic aspirations of American childhood: astronaut, construction worker, archaeologist, LEGO Engineer, *etc*. and developed a keen interest in science and engineering. This interest was fostered by the support of his parents and maternal grandfather (a Grumman aeronautical engineer) and grew during summers spent at local science and space camps.

As his education progressed, Andrew was drawn to the science of materials in part by his love for cycling and windsurfing, and the amazing properties that carbon-fiber and other composite materials brought to frames, sails and boards. Andrew's first exposure to materials research came during a summer internship program at Brookhaven National Laboratories where he worked with Dr. Carl Czajkowski on several projects including thermally sprayed thermite welds and spent nuclear fuel container corrosion.

Andrew attended the University of Delaware in 1999 on a DuPont Scholarship and graduated in 2003 with a B.S. in Chemistry and a minor in Physics. While there, he pursued research in the Dept. of Materials Science & Engineering with Prof. S. Ismat Shah, where he studied the sol-gel growth of nanostructured, Neodymium-doped titanium dioxide photocatalysts for the degradation of organic contaminants in water.

In 2003, Andrew arrived at Cornell University and began working in the group of Prof. Ulrich Wiesner on the growth, characterization and application of fluorescent silica nanoparticles for bioimaging and sensing, from which he graduated in 2008.

To all who have helped me

and made the trip worthwhile.

# ACKNOWLEDGMENTS

I would first like to thank my parents and family for fueling my interest in science at an early age and supporting me throughout. Thanks also to all my friends for putting up with the bad days and helping me to celebrate the good ones. I would particularly like to thank my colleagues, advisors and mentors at Cornell for making this experience far more than a degree or a job – studying science has been my life for the past five years, and I hope always to be in the company of such dedicated individuals. It has been a privilege to work with Prof. Uli Wiesner, whose enthusiasm and optimism for new ideas has helped my research to evolve in new directions I would never have anticipated at the start.

Among my Wiesner group colleagues, a few deserve special mention: Hooisweng Ow for her pioneering work on the core-shell architecture that made this possible; my doppelganger, Erik Herz, who has been an ally, a colleague and above all a friend; Marleen Kamperman for livening many hungry hours of staring at SEM images with jokes and discussions of food; and Tara, George, Bill, Akeisha, Yoong and Mareli, who I hope learned as much from me as I learned in teaching them.

Finally, I thank Erin, the wonderfully patient, loving and supportive love of my life for helping to keep me sane, making me laugh, and being there for me all along.

TABLE OF CONTENTS

LIST OF FIGURES

LIST OF TABLES

# LIST OF ABBREVIATIONS

%ID – Percent of initial dose, a measure of nanoparticle retention/excretion *in vivo*

3D – Three-dimensional

APTS – 3-aminopropyltriethoxysilane, an amine-containing silanizing agent

BAPTA – 1,2-*bis*(*o*-aminophenoxy) ethane-N,N,N',N'-tetraacetic acid, $Ca^{+2}$-chelating group

BET Analysis – Brunauer-Emmet-Taylor analysis for gas adsorption/desoprtion behavior, used to determine surface area and porosity

BJH Analysis – Barret-Joyner-Hallenda analysis for gas adsorption/desoprtion, used to determine pore volumes

BSA – Bovine Serum Albumin

*c* – Molar ratio of TEOS:seed particles in seeded reverse microemulsion particle synthesis

C Dot – CU/Cornell Dot, core-shell silica nanoparticle based on covalently-bound organic dyes in the particle core

C Dot Sensor – Cornell Dot Sensor, characterized by a core-shell architecture containing a reference dye in the particle core, with a sensor dye embedded in the particle shell to facilitate quantitative ratiometric imaging

CG – Calcium Green, a $Ca^{+2}$-sensitive green-emitting fluorophore

CLSM – Confocal Laser Scanning Microscopy

CT – Computed Tomography Imaging

Cy5 – Organic Dye, far-red (670nm) emission

DICOM – Digital Imaging and Communications in Medicine, a standard format for viewing medical image data

DLS – Dynamic Light Scattering, a method for particle size determination based on autocorrelation of scattered light intensity

DMSO – Dimethylsulfoxide

*E. coli* PHL628 – *Escherichia coli* bacteria

$E_{total}$ – Total percent of particle excreted at a specific timepoint

EDTA – Ethylenediaminetetraacetic acid

$F_i$ – Ratio of fluorescent intensity of sensor to reference dye in ratiometric sensing

$F_{max}$, $F_{min}$ – High and low analyte concentration values of $F_i$, respectively

FCS – Fluorescence Correlation Spectroscopy, a method for fluorescent particle / molecule size, size dispersity and brightness determination, based on autocorrelation of fluorescence intensity within a small focal volume of known size

FcεRI – Cell surface receptor for IgE expressed on the surface of RBL Mast Cells

FITC – Fluorescein Isothiocyanate, a green-emitting reactive organic fluorophore and pH sensor

Fluo-4 – Dichlorofluorescein-derived $Ca^{+2}$-sensitive dye

FWHM – Full-width at half-maximum

GFP – Green Fluorescent Protein

IgE – Immunoglobulin E, antibody

IODOGEN – A method for radioiodination

LB media – Luria-Bertani media

M41S – Structural family including many molecular sieve materials

MCM-41 – Hexagonal pore structure class

MCM-48 – Cubic bicontinuous pore structure class

microPET – High-resolution PET measurements

MRI – Magnetic Resonance Imaging

MWCO – Molecular weight cut-off

N – Number of monomer units in a polymer

NA – Numerical Aperture

NBD – 7-nitrobenz-2-oxa-1,3-diazole, a green-emitting reactive organic

NIR – Near-infrared wavelength range (650-900nm)

NIRF – Near-infrared fluorescence

OD – Optical Density

*p* – cosurfactant-to-surfactant molar ratio

PBS – Phosphate-Buffered Saline

PDB – Phorbol (12,13) dibutyrate, a phorbol diester which mediates macropinocytosis of extracellular fluid in RBL Mast cells.

PEBBLE – Probes encapsulated by biologically localized embedding

PEG – poly(ethylene glycol), a biologically compatible polymer

PET – Positron Emission Tomography

PET-CT – co-registered Positron Emission Tomographic imaging with Computed X-ray Tomographic imaging.

PLGA – Poly(lactic-*co*-glycolic acid)

QD – Quantum Dot, semiconductor nanocrystal fluorophore

*R* – $H_2O$:surfactant molar ratio in reverse micelle systems

$R_{total}$ – Total particle retention *in vivo*

RBL(-2H3) Cell – Rat Basophilic Leukemia Mast Cell

SEM – Scanning Electron Microscope

SNARF – semi-napthorhodafluor, an internally-ratiometric pH sensor dye

$t_{1/2}$ – half-life

TCA cycle – Tricarboxylic Acid cycle/Citric Acid cycle/Krebs cycle, a key metabolic pathway in degradation of carbohydrates and fats to release chemical energy

TEM – Transmission Electron Microscope

TEOS – tetraethoxysilane/tetraethyl orthosilicate, a pure silica precursor

TIF – Tagged Image Format

TRITC – Tetramethylrhodamine Isothiocyanate, an orange-emitting reactive organic fluorophore

Triton X-100 – Polyethylene glycol *p*-(1,1,3,3-tetramethylbutyl)-phenyl ether

# CHAPTER 1

# FLUORESCENT SILICA NANOPARTICLES: TOWARDS "LAB ON A PARTICLE" ARCHITECTURES FOR NANOBIOTECHNOLOGY*


## *1.0 Abstract*

Novel nanoscale fluorescent materials are integral to the progress of emergent fields such as nanobiotechnology and facilitate new research in a variety of contexts. Sol-gel derived silica is an excellent host material for creating fluorescent nanoparticles by the inclusion of covalently bound organic dyes. Significant enhancements in the brightness and stability of organic dye emission can be achieved for silica-based core-shell nanoparticle architectures at length scales down to the tens of nanometers with narrow size distributions. This review chapter will highlight these findings and describe the evolution of the fluorescent core-shell silica nanoparticle concept towards integration of multiple functionalities including mesoporosity, metal nanoshells and quantitative chemical sensing. These developments point towards the development of "lab on a particle" architectures with promising prospects for nanobiotechnology, drug development and beyond.



* Originally Published as: Andrew Burns, Hooisweng Ow, Ulrich Wiesner. "Fluorescent Silica Nanoparticles: Towards 'Lab on a Particle' Architectures for Nanobiotechnology" *Chemical Society Reviews*, 2006, 35(11), 1028-1042, Reprinted with permission of the Royal Society of Chemistry

### *1.1 Introduction*

In this review, recent progress in the field of core-shell fluorescent silica nanomaterials will be described, with special emphasis on applications in the emerging field of nanobiotechnology. Rather than attempting a general overview of this exciting and rapidly growing research field, general features, challenges and future trends will be highlighted through examples of the recent work of the Wiesner group and collaborators at Cornell University. This work encompasses water-soluble, non-toxic fluorescent core-shell silica nanoparticles of various compositions and architectures with unusually high brightness and photostability levels, as well as narrow particle size distributions suited for applications in the life sciences and beyond, as illustrated in Figure 1.1.

The section will begin with an introduction to nanoscale fluorescent materials, focusing on the materials issues central to creating effective emitters, including a brief review of several common classes of photoemitters. We will then introduce fluorescent core-shell silica nanoparticles as a materials platform, focusing on their photophysical and materials characterization. The versatility of the silica-based particle synthesis will be demonstrated through control of specific particle characteristics such as color and size, as well as through the integration of novel particle properties such as mesoporosity or metal shells. Further, we will cover two applications of specific core-shell silica nanoparticle architectures in nanobiotechnology, emphasizing the integration of two different functionalities to create effective probes of biology on the nanoscale. Finally, we will begin to explore some of the possibilities for future research, building on the versatility of silica as a host material and the modularity of the core-shell architecture to build highly integrated “lab on a particle” architectures.

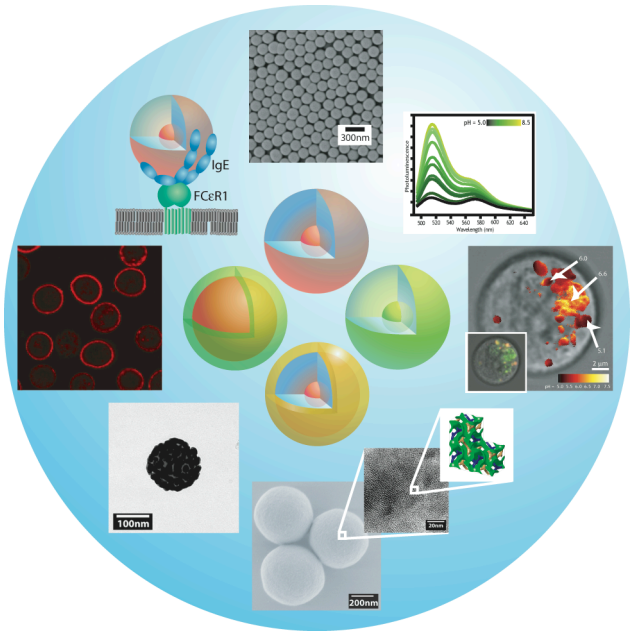


Figure 1.1 - An overview of the versatility of the fluorescent core-shell silica nanoparticle platform: illustrations of single and dual-emission particles as well as gold-nanoshell encapsulated core-shell particles are shown at the heart of the figure, while a variety of applications including bioimaging, drug delivery, sensing and therapeutics are shown in the periphery

### *1.1.0 Fluorescent Nanoscale Materials*

The phenomenon of fluorescence is ubiquitous in fields from biology to information technology and beyond. The excellent spatial (diffraction limit or better) and temporal (nanosecond) resolution, as well as the high signal-to-noise ratios inherent to fluorescent analyses, make fluorescent materials ideally suited to explore the nanoscale. The development of novel fluorescent materials is integral to the progress of emergent fields such as nanobiotechnology, photonics and optoelectronics. Every application has its own particular constraints, but the fundamental issues for any fluorescent material are the same: brightness and stability. There are several classes of materials that are currently employed as fluorescent emitters/probes, including organic and metallorganic dye molecules, fluorescent proteins, semiconductor quantum dots, polymer/dye-based nanoparticles and silica/dye hybrid particles (Figure 1.2), each with their own advantages and disadvantages as recently reviewed by Wang *et al*[1].

### *1.1.1 Organic and Metallorganic Dye Molecules*

The smallest (and generally dimmest) fluorescent emitters in use today are single organic or metallorganic dye molecules, which generally consist of π-conjugated ring structures such as xanthenes, pyrenes or cyanines[2]. These fluorophores are commercially available with emissions across the spectrum from UV to the near infrared (~300-900 nm) and may be fine-tuned to particular wavelengths or applications by changing the chemistry of their substituent groups. As shown in Figure 1.2 a, the small size of individual dye molecules (~1 nm) make them an excellent choice for many applications, especially in biology where researchers seek to minimize the physical perturbations to the system under investigation. However, small size can also be detrimental, leading to non-specific labeling and high background signals as dyes diffuse away from their intended targets. Spectrally,

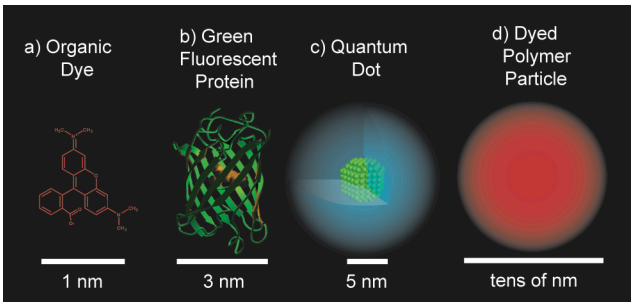


Figure 1.2 - Several common fluorescent nanoscale materials including (a) organic dye molecules (tetramethylrhodamine), (b) green fluorescent protein, (c) polymer-coated, water-soluble semiconductor quantum dots and (d) dyed polymer particles.

organic dyes tend to have fairly wide absorption and emission spectra (FWHM ~ 50nm), which can lead to spectral overlap and re-absorption when using multiple dye species simultaneously[3]. In normal use, dye molecules are exposed to a variety of harsh environments and often suffer from photobleaching and quenching due to interactions with solvent molecules and reactive species such as oxygen or ions dissolved in solution. Further, the lack of protection manifests itself in the π-π stacking behavior that many dyes exhibit at high local concentrations, *e.g.* when deposited on surfaces or interfaces, leading to energy transfer and dye quenching[4]. The fluorescent and chemical properties of these single molecule fluorophores are detailed in texts by Haugland[2] and Lakowicz[3] and were recently reviewed by Wang *et al*[1].

### *1.1.2 Fluorescent Proteins*

Increasing in size from single dye molecules, green fluorescent proteins (GFP), such as those originally isolated from *Aequora* jellyfish (Figure 1.2 b), are of great interest to biologists for their ability to indicate genetic expression levels in living systems by the addition of the GFP sequence genes to the host's genome (reviewed by Wang[1] and Tsien[5]). A variety of related fluorescent proteins have been generated, covering much of the visible spectrum, permitting simultaneous labeling of multiple genetic activities within the same system. Although their fluorescence emission is similar to organic dyes, fluorescent proteins are fundamentally different from other labels, as their synthesis and localization are dependent primarily upon the gene transcription activity of the host cell or organism, rather than any external targeting. Similar to dyes, the fluorescent proteins tend to exhibit excited state interactions, which can lead to stochastic blinking, quenching and photobleaching[5].

### *1.1.3 Semiconductor Quantum Dots*

Colloidal semiconductor quantum dots (QDs) were among the first nanomaterials to attract the attention of the biological community. These nanoparticles (hundreds to thousands of atoms) are traditionally made from crystals of II-VI or III-V elements (PbS, CdSe, etc) or other semiconductors and may be synthesized in many different colors by tuning the particle size (2-50nm) to change the Bohr exciton radius, and thus the wavelength of the emitted light (Figure 1.2 c). QDs exhibit fundamentally different absorption and emission behavior from dyes and fluorescent proteins, characterized by wide absorptions with large absorption cross-sections (10-100x dye), large Stokes' shifts, narrow emission bands (FWHM ~20-40nm) and minimal photobleaching[6].

Most QDs are hydrophobic by nature, requiring layers of polymeric or inorganic material to compatiblize them with the aqueous conditions of biology and other fields, increasing their effective hydrodynamic radii to 15nm or more. Additionally, QDs are generally made from heavy metal ions such as $Pb^{2+}$ or $Cd^{2+}$, so their use exposes researchers and their experimental systems to these toxic materials as well as generating a toxic waste stream into the environment.[7] In addition to the stochastic blinking phenomena seen in all single emitter systems, recent work has shown that more than 40% of quantum dots used under biological conditions may exhibit dark states,[8] requiring the use of higher labeling concentrations to yield the desired brightness. The biological applications and photophysical properties of quantum dots were recently detailed in reviews by Mattoussi[6] and Parak[9].

### *1.1.4 Dyed Polymer Nanoparticles*

Another common class of fluorescent materials is based on polymers such as dextran or polystrene latex beads in combination with organic dyes (Figure 1.2 d). These approaches generally incorporate the dye by covalent attachment of the dye molecules to the polymer chain or physical entrapment in a cross-linked particle[1,2]. This often leads to low incorporation rates and offers little protection to the dye molecules, making these probes prone to leaching, quenching and photobleaching interactions under working conditions.

### *1.1.5 Fluorescent Silica Nanoparticles*

In order to create more robust emitters, researchers have developed hybrid organic/inorganic nanoparticles from organic dye molecules and amorphous silica. As a matrix material for fluorescent probes, silica provides a chemically and mechanically stable vehicle, which can protect the encapsulated dye molecules from external perturbations, while exposing a biocompatible and easily functionalized surface to the environment and in some cases enhancing the photophysical properties of the encapsulated dyes[10].

Spherical silica nanoparticles are generally made by one of two chemical approaches: reverse microemulsion and sol-gel synthesis. Reverse microemulsion techniques rely on the controlled aqueous environment within surfactant-confined micelles in a non-polar solvent to create monodisperse spherical colloids. Such nanoparticle syntheses were extensively explored by Arriagada and Osseo-Asare[11] in the 1990s, and are continued today by the Tan group that began developing fluorescent nanoparticles in the mid-1990s by physically entrapping metallorganic dyes such as tris (2,2'-bipyridyl)dichlororuthenium in silica nanoparticles[12]. The confined "nanoreactor" environment within the reverse micelle has been shown to

yield highly monodisperse particles and increase the incorporation of nonpolar molecules, which are often difficult to incorporate into the hydrophilic silica matrix. However, the lack of covalent attachment of the fluorophore to the silica matrix means that the dye molecules can leach out of the particles over time, decreasing per-particle brightness, increasing background signal and exposing the dyes to their environment. Further, these syntheses often have low yields and the use of surfactants necessitates extensive washing to remove the surfactant molecules before any biological application to avoid disruption or lysis of biomembranes by the surfactant molecules.

Alternatively, in the late 1960s, Stöber and co-workers developed a mild synthetic protocol for growing monodisperse spherical silica nanoparticles (~100 nm) based on the sol-gel chemistry of silicon alkoxides[13]. Stöber's method involves the hydrolysis and condensation of tetraethoxysilane (TEOS) in ethanol solution in the presence of water with ammonia as a catalyst to create monodisperse, spherical, electrostatically-stabilized particles. The Stöber synthesis was investigated by several groups to determine the effects of the various reagents on size, reaction kinetics, monodispersity and sphericity of the particles[14]. The van Blaaderen group expanded on this work by covalently incorporating organic fluorophores into the silica matrix by coupling them to reactive organosilicates[15]. Throughout this work, the particle sizes reported remained in the hundreds of nanometers to microns regime, which are useful for many applications such as the study of colloid dynamics and photonic crystals, but are generally too large to be truly effective probes for biology.

### *1.2 Bright and Stable Fluorescent Core-Shell Silica Nanoparticles: C Dots*

In 2005, we reported the synthesis of organic dye/silica-based core-shell nanoparticles referred to as C dots, with hydrodynamic radii on the order of 10-15 nm and per-particle brightness levels approaching those of quantum dots[10]. Size control

and brightness are achieved by encapsulating the emitters within the core of a core-shell nanoparticle (Figure 1.3 a). Towards this end, we have built upon the work of the van Blaaderen group to develop fluorescent silica precursors by the coupling of a reactive dye species with an organosilicate source. The hybrid precursors are then hydrolyzed and condensed with pure silica to yield hybrid organic/inorganic cores. These cores act as heterogeneous nuclei for the growth of a pure silica shell, further protecting the encapsulated dyes. This concept was originally demonstrated by incorporating multiple tetramethylrhodamine (TRITC) dye molecules into uniform, monodisperse 25nm diameter core-shell particles (Figure 1.3 b)[10].

### *1.2.1 Photophysical Characterization*

The photophysical properties of these core-shell particles and their constituent parts were further characterized to determine, *e.g.*, the effects of encapsulation on dye brightness and stability. In order to probe the behavior of single particles, multi-photon fluorescence correlation spectroscopy (FCS) was employed[16]. This technique is similar to dynamic light scattering (DLS) except that the detected light used for analysis is from fluorescence, rather than scattering. From the autocorrelation of the time-domain signal, the diffusion coefficient of the emitters can be determined, giving the particle size via the Stokes-Einstein equation. The signal intensity scales with the number of emitters within the multi-photon focal volume (~100 attoliters[17]) resulting in very accurate concentration information that can be employed to determine per-particle brightness for each of the diffusing species. Finally, analysis of the accuracy of the fit to the FCS autocorrelation decay curves gives a precise measure of the particle size distribution[16,18].

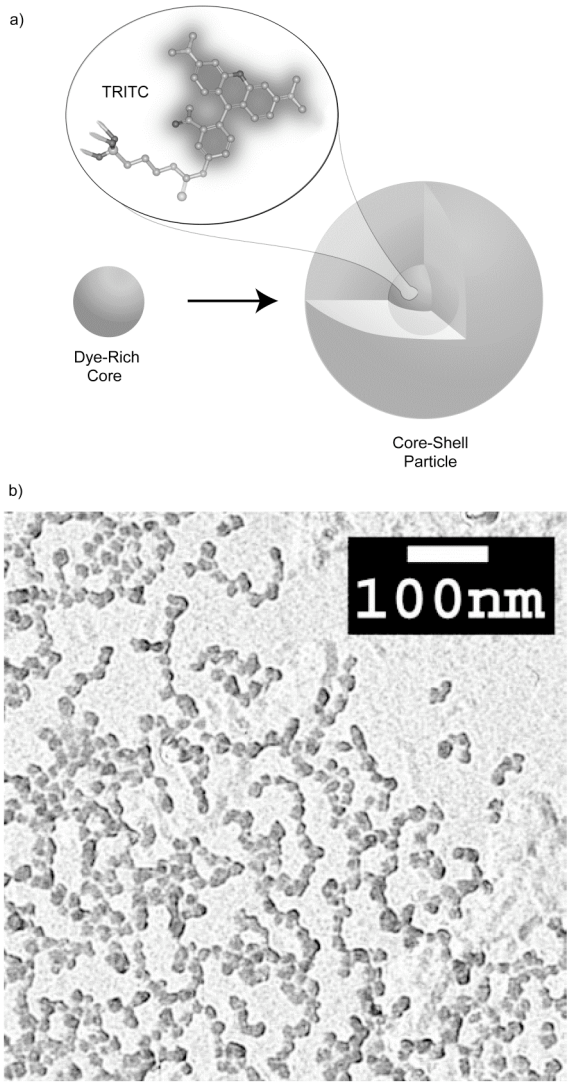


Figure 1.3 - (a) A schematic representation of the dye-rich core-shell architecture of the C dot particles, in this case covalently incorporating the organic dye tetramethylrhodamine isothiocyanate (TRITC) and (b) a representative TEM image of 30 nm diameter TRITC-based core-shell silica nanoparticles with a narrow particle size distribution. Reproduced (in part) with permission from *Nano Lett.* 2005, *5*, 113-117. Copyright 2005 American Chemical Society.

First, FCS measurements were made on a series of the parent fluorophores, cores, and core-shell particles made from the same batch of core particles. The TRITC dye molecules were found to have hydrodynamic radii of approximately 1.0 nm, while the core particles were found to be 2.2 nm in radius, and the final core-shell particles were 15 nm in radius (Figure 1.4 a) with a narrow particle size distribution. Interestingly, it was found that although containing multiple fluorophores, the per-particle brightness of the cores was less than that of both the core-shell particles and the free dye molecules, suggesting mutual quenching of the dyes, see Figure 1.4 b. Figure 1.4 further demonstrates that the addition of the silica shell onto the core significantly enhances the brightness of the core-shell particles. Fluorescence lifetime measurements show that this phenomenon can be attributed to an increase in the radiative and a decrease in the non-radiative decay rates for the dyes upon encapsulation in the core-shell architecture leading to an enhanced dye quantum yield[19]. Further, rotational anisotropy measurements show that the decrease in the non-radiative decay rate correlates well with the rigidity of the dye environment in the silica particle as compared to the free dye in solution[19].

The sequestered, pseudo-solid state environment that the dyes experience within the silica matrix yields a variety of benefits. Beyond the brightness enhancement evident in Figure 1.4 b, the core-shell architecture prevents the dyes from freely interacting with solvent molecules as indicated in Figure 1.5 a and b. Free dye molecules exhibit different fluorescent behavior in different solvents (solvatochromic shift) owing to changes in the excited state energies in solvents of different polarity. This is evinced by the ~10nm blue-shift in absorption and emission peaks for TRITC in ethanol relative to water as shown in Figure 1.5 a. Once incorporated into the core-shell particles, the same dyes show negligible

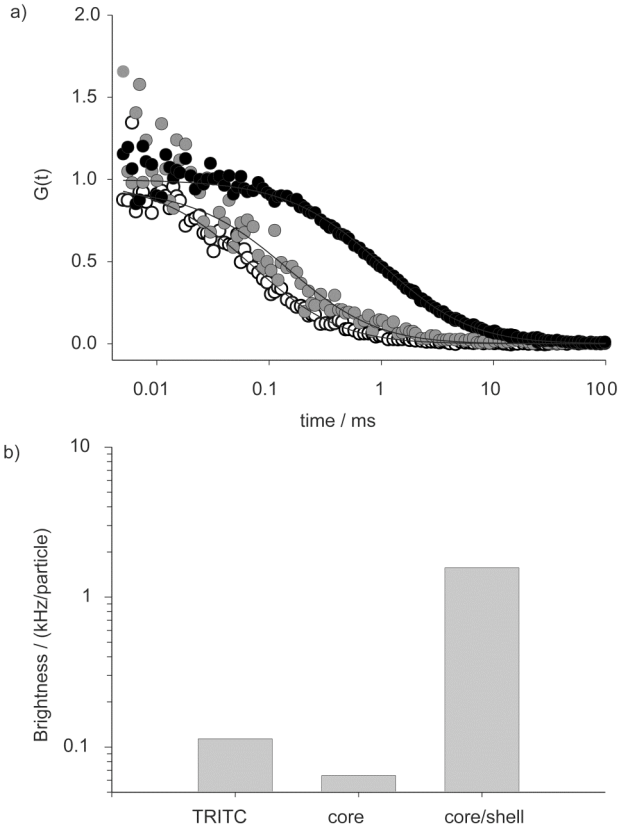


Figure 1.4 - (a) FCS autocorrelation curves for free TRITC dye (white), TRITC-based silica core particles (grey) and 30nm core-shell TRITC-based silica nanoparticles (black) and (b) a comparison of per-particle brightness values for TRITC dye, core particles and core-shell nanoparticles. Reproduced with permission from *Nano Lett.* 2005, *5*, 113-117. Copyright 2005 American Chemical Society.

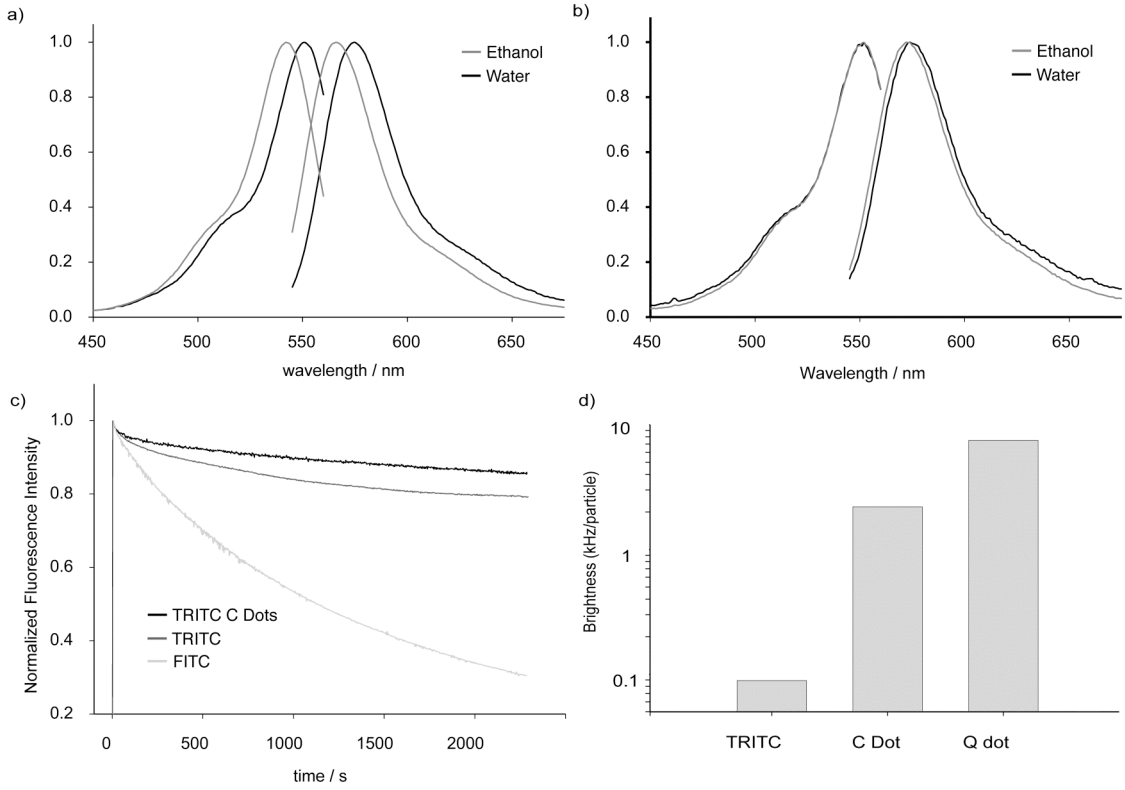


Figure 1.5 - Absorption and emission spectra for (a) free TRITC dye in water (black) and ethanol (grey) and (b) core-shell TRITC-based silica nanoparticles in water (black) and ethanol (grey) showing the decreased solvatochromic shifts induced by the protective core-shell architecture, (c) Photobleaching measurements of fluorescein (light grey), TRITC free dye (dark grey) and TRITC-based C dots (black) showing the enhanced stability of the core-shell particle architecture, and (d) a comparison of the brightness of free TRITC dye with same-sized C dots and quantum dots in water at the same optical density. Reproduced with permission from *Nano Lett.* 2005, *5*, 113-117. Copyright 2005 American Chemical Society.

solvatochromic shifts between the two solvents (Figure 1.5 b) demonstrating that the dye molecules are effectively removed from interactions with the solvent environment[10].

In addition to enhanced brightness, narrow size distributions and diminished solvatochromic shifts, encapsulating dyes into the core-shell silica particles also improves their stability against photobleaching. TRITC is inherently a quite stable dye, and thus exhibits less photobleaching than fluorescein, which is commonly used as a photobleaching standard (Figure 1.5 c). Even so, silica encapsulation reduces TRITC's photobleaching kinetics by approximately an order of magnitude[19].

Finally, a direct brightness comparison between individual TRITC molecules, optimized C dots encapsulating TRITC and water-soluble quantum dots (CdSe/ZnS) of similar emission wavelength (577nm) was performed via FCS. Within the errors of the measurements, the particle sizes of the C dots and quantum dots were identical (14-15nm hydrodynamic radius) and measurements were performed on samples of identical optical density. The per-particle brightness values of both C dots and QDs were found to be one to two orders of magnitude greater than free TRITC, while the QDs were only a factor of 2-3 brighter than the C dots (Figure 1.5 d). These results showed for the first time that organic dye-based probes could be fine-tuned to reach brightness levels similar to quantum dots of the same size in aqueous solution. Subsequent work has shown that the factor of ~30 times increase in brightness of the C dots over free TRITC in water is a result of the product of a per-dye enhancement (see below) and the number of dye molecules in each particle, implying that the brightness levels may be further increased through optimization of the particle chemistry and architecture[19].

Quantum dot fluorescence is known to occur primarily by single exciton transitions, while the multiple dye molecules within each C dot absorb and emit

independently. This circumvents the issue of stochastic blinking suffered by quantum dots[8] and individual dye molecules under continuous illumination, by providing multiple independent emitters within a single probe. Furthermore, the silica environment not only enhances the fluorescence yield, but also ensures separation between neighboring dye molecules, suppressing energy transfer and quenching. Finally, the silica nanoparticle architecture creates probes that are easier to handle and purify than single dye molecules as well as exposing the silica surface for conjugation via various organosilicates, facilitating multifunctional probes.

### *1.2.2 Tuning Particle Color*

To explore the generality of the enhancements of silica encapsulation, we have investigated the behavior of multiple dyes from several dye families throughout the visible spectrum[10,20] as shown in Figure 1.6 a. As an example, Figure 1.6 b shows the results of incorporation of 7-nitrobenz-2-oxa-1,3-diazole (NBD) in core-shell silica nanoparticles of similar formulation to those shown above for TRITC[21]. Unlike TRITC, NBD is not optimized for use in aqueous environments, and is known to exhibit low quantum yields (~0.01) in aqueous solution[2]. For samples of equal optical density (photoabsorption), incorporating NBD in core-shell particles results in significantly increased fluorescence yield relative to un-conjugated NBD in water as shown in Figure 1.6. It is worth stressing the importance of such emission enhancement for encapsulated dyes as a general concept. Few dyes are optimized for fluorescence in aqueous solution, and those that are tend to be extremely expensive, if at all commercially available. The majority of dyes perform best outside of the aqueous milieu, limiting their applications in biologically relevant fields. Encapsulation of non-optimized organic fluorophores in core-shell silica nanoparticles

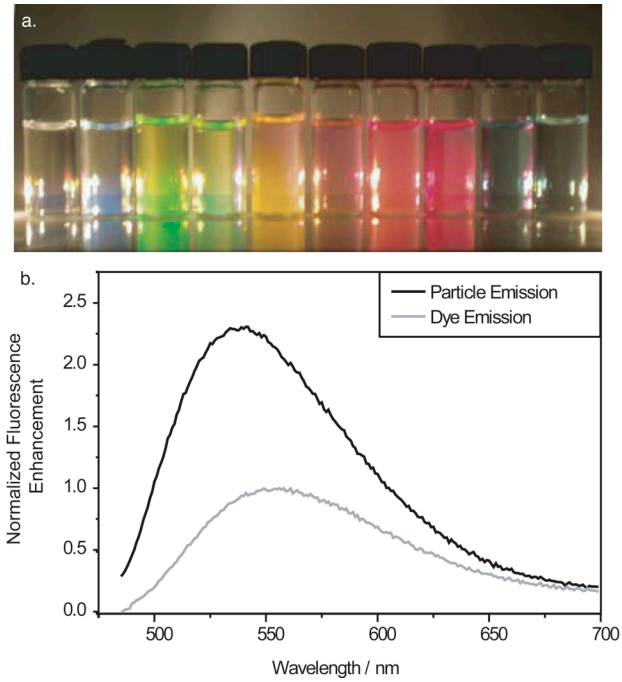


Figure 1.6 (a) The core-shell fluorescent silica nanoparticle architecture may be expanded to incorporate a wide range of dye colors by using different dye species in the core including (left to right): AlexaFluor 350, N(7-dimethyl-amino-4-methylcoumarin-3-yl), AlexaFluor 488, fluorescein isothiocyanate, tetramethylrhodamine isothiocyanate, AlexaFluor 555, AlexaFluor 568, Texas Red, AlexaFluor 680 and AlexaFluor 750. (b) Absorption-normalized emission spectra of 7-nitrobenz-2-oxa-1,3-diazole (NBD) free dye (grey) and NBD-based core-shell silica nanoparticles (black), showing greater than twofold enhancement in photoemission for equal peak photoabsorption. Reproduced (in part) with permission from *Nano Lett.* 2005, *5*, 113-117. Copyright 2005 American Chemical Society.

may render their optical performance in aqueous solution more competitive to highly optimized dyes, opening an area of research that so far has mostly been neglected.

### *1.2.3 Tuning Particle Size*

The core-shell architecture can be generalized not only to other dyes and colors, but may also be expanded to cover the gamut of sizes accessible through the Stöber reaction. For applications ranging from biology to photonics, it is desirable to tailor particle size throughout the nanometer to micron scale to study, for example, molecular-scale phenomena in biology or to generate active building blocks for photonic structures. By simply controlling the concentrations of the various reactants in the synthesis, one can tailor the core and shell sizes from nanometers to microns in size as shown in Figure 1.7. These scanning electron micrographs depict core-shell TRITC-based fluorescent particles with (a) 50nm, (b) 150nm, (c) 250nm, (d) 500nm, and (e) 1.5μm diameters. In all cases, the images show the narrow particle size distributions expected from the Stöber synthesis in these size regimes[13,14,21].

### *1.2.4 Tuning Collective Behavior*

The core-shell architecture not only provides a means to engineer the photophysical properties of the encapsulated fluorophores at the single-particle level, but also creates a means to tailor the collective behavior of the particles. For example, in many applications such as thin films, active photonic crystal building-blocks and cellular labeling for confocal microscopy, it is desirable to have extremely dense lateral or three-dimensional packing of emitters to yield maximum brightness. Researchers have tried to create such dense labeling with dye molecules and quantum dots, but often find that these emitters suffer from energy transfer and quenching at high spatial density, counter-acting their high loading[4].

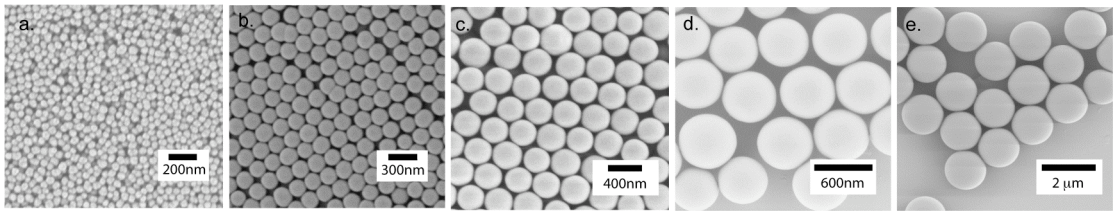


Figure 1.7 - Representative scanning electron micrographs of core-shell fluorescent silica nanoparticles of different diameters: (a) 50nm, (b) 150nm, (c) 250nm, (d) 500nm, (e) 1.5µm

In contrast, the core-shell architecture allows the fine-tuning of inter-particle interactions by tailoring the shell thickness. Shell thicknesses comparable to the Förster radius of energy transfer[3] preclude interactions between the particle cores and permit dense packing of emitters, creating maximal fluorescence. A simple case of high-density packing is shown in Figure 1.8 for particles arrayed on a surface. Each particle core is effectively separated from its neighbors by twice the pure silica shell thickness, creating high spatial emitter density without permitting energy transfer between neighboring fluorophores. As a first example of high emitter density architectures, ultra-bright colloidal particles with a raspberry architecture have been produced where the C-dots are deposited as a dense monolayer on ZnS core particles for potential application in active colloidal photonic crystals[21].

### *1.3 Ordered Mesoporous Fluorescent Silica Particles*

Silica offers a variety of appealing properties as a host material for nanoparticle probes. As a first example towards creating multifunctional particle architectures beyond fluorescence, ordered mesoporosity (2-50 nm) can be integrated through the use of amphiphilic structure-directing agents such as surfactants or block-copolymers. Most of these molecular sieve materials are classified in the M41S family, with the MCM-41 (hexagonal) and MCM-48 (cubic bicontinuous) classes being most common. The structure and pore size of these materials have been extensively studied since their discovery at Mobil in the early 1990s[22], and have attracted much attention for applications in sorption, separation and catalysis as well as within the biological community. MCM-41 (hexagonal) mesoporous materials have been extensively studied as vehicles for controlled therapeutic release[23], while the biological applications of MCM-48 (cubic bicontinuous) materials are just beginning to be realized[24]. Despite their lack of biodegradability, these silicate materials do offer

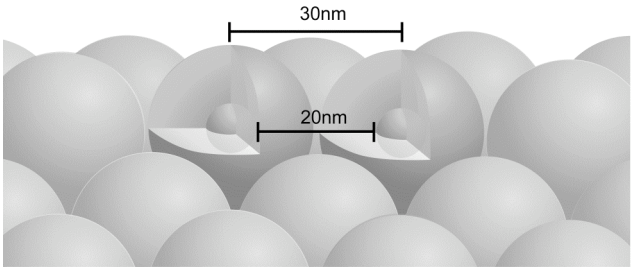


Figure 1.8 - A schematic illustration of close-packed C dot core-shell silica nanoparticles on a surface, showing the separation of the particle cores, permitting high spatial density of photoemitters without energy transfer between neighboring particles.

a variety of interesting attributes including easily tailored pore and particle sizes and facile surface functionalization. MCM-48 materials have even been shown to induce hydroxyapatite growth *in vitro*, making them a potentially viable scaffold for hard tissue (*e.g.*, bone) regeneration[23].

To explore the use of the MCM-48 materials structure (Figure 1.9 a) we synthesized fluorescent MCM-48 based silica particles by a modified version of the method of Schumacher *et al.*, using hexadecyltrimethylammonium bromide as the structure-directing agent and integrating covalently-bound TRITC as a fluorescent label[18,25]. The particles were grown to a final diameter of 400 nm (Figure 1.9 b). Transmission electron microscopy (Figure 1.9 c) and nitrogen adsorption-desorption measurements (BJH analysis, data not shown) revealed a pore size of 2.74 ± 0.11 nm, creating particles with large internal surface areas. In order to access all of the internal pores, the templating agent must, of course, be removed. The most complete method of surfactant removal is calcination. This resulted in material with extremely high surface area (BET analysis: 1300 $m^2$ / g), but led to sintering of the particles and destroyed the organic fluorophores. Alternatively, repeated washing steps were used to remove the templates. A lower internal surface area of the resulting particles (~100 $m^2$ / g) suggested incomplete template removal, but provided ample volume for initial drug release studies.

In order to assess the viability of the fluorescent MCM-48 particles as a system for cellular uptake and controlled release of, *e.g.*, a drug, we worked with camptothecin, a powerful chemotherapeutic agent, which suffers from low water solubility. The particles were compared with non-porous Stöber-type fluorescent silica particles of a similar size, as well as poly (lactic-co-glycolic acid) (PLGA) polymer-based particles loaded with 15% (w/w) camptothecin (Saltzman Group, Yale University). The mesoporous and non-porous particles were exposed to camptothecin

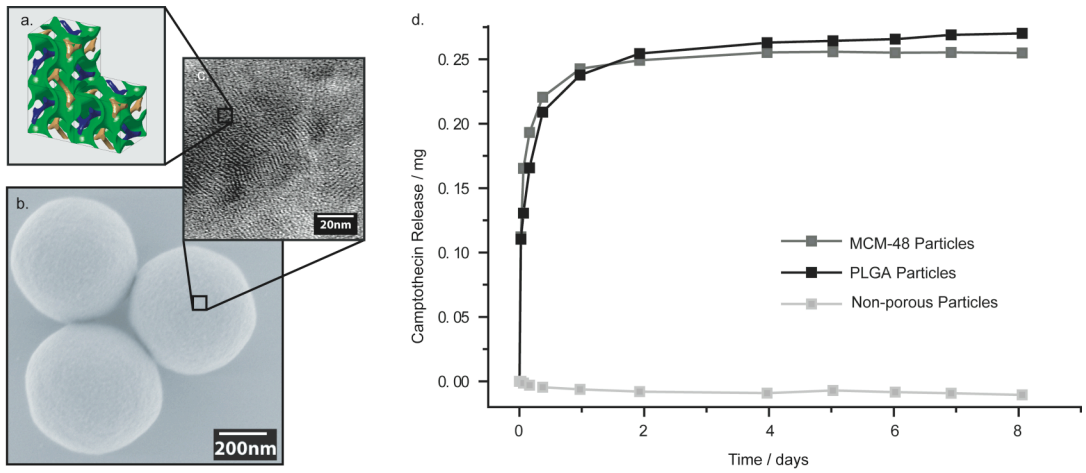


Figure 1.9 - (a) A structural representation of the MCM-48 cubic bicontinuous porous network; (b) a scanning electron micrograph of 400nm MCM-48 porous silica nanoparticles; and (c) a thin-section TEM image showing the mesoporous structure of the MCM-type particles. (d) A plot of the drug release characteristics of the MCM-48 nanoparticles (red), PLGA nanoparticles (black) and non-porous Stöber-type nanoparticles (blue) for the chemotherapeutic agent camptothecin.

solution in dimethyl sulfoxide (DMSO) and washed thoroughly in phosphate buffered saline solution (PBS) to remove any free camptothecin molecules. Following drug loading, the concentration of camptothecin was quantified in PBS by standardized absorption measurement so that similar drug concentrations could be assessed across different porous host materials. The drug release kinetics were then monitored by spectrophotometry, measuring the optical density of aliquots of the PBS solution at the absorption peak of camptothecin, following the removal of the particles by centrifugation. The data, as plotted in Figure 1.9 d, show that the silica- and PLGA-based particles exhibit nearly identical drug release behavior, while the non-porous silica particles do not exhibit any appreciable drug release activity. As well, the timescale of release for both the PLGA and MCM-48 are in the clinically relevant realm of hours to days, making them potential candidates for future drug release studies.

It is noteworthy that the PLGA and MCM-48 materials show nearly identical release kinetics, considering that the release mechanisms behind each are quite dissimilar. For PLGA, the entrapped drug molecules are released as the polymer matrix breaks down, while the MCM-48 materials remain intact throughout and slowly release their cargoes by diffusion out of the tortuous mesoporous network. This example underscores the versatility of silica as a materials platform for the development of highly functional probes and tools for the life sciences.

### *1.4 Colloidal Metal Nanoshells*

Thin metal shells can be grown on the surface of silica nanoparticles to create novel metal/dielectric architectures. Pioneering work in this field was performed by the Halas group, who described the synthesis of gold and silver nanoshells on silica nanoparticles in the 1990s and began to explore the photophysical properties of these

new architectures[26]. Colloidal metal shells exhibit plasmon resonances that are tunable over a wide range of frequencies by changing the ratio of core-to-shell thickness. These resonances yield particles that absorb light very strongly at different wavelengths throughout the visible and near-infrared spectrum (Figure 1.10).

In these previous works, the metal nanoshells were grown over pure silica nanoparticles bearing no active fluorescent species. It is well known however, that the emission properties of a fluorophore can be dramatically changed by electromagnetic interactions with electron-dense materials such as metals[27]. Further, these interactions can be controlled by altering the geometry of the metal/dielectric system and under favorable conditions can yield benefits such as increased photostability and longer fluorescence lifetimes, without any loss in detectable fluorescence[27]. It is thus interesting to develop C dot-type fluorescent core-shell silica nanoparticles encased in a metal shell, such that the dye-metal shell interactions can be explored though variations in the core-shell/metal-shell particle geometry. To this end, we synthesized C dots encapsulated in a gold shell, shown schematically in Figure 1.11 a[18].

These nanoparticles were prepared via a step-wise growth of a gold nanoshell around 50nm C-dot core-shell silica nanoparticles with TRITC-rich particle cores. The gold nanoshell was generated based on the synthetic protocols[26] of the Halas group, wherein nano-sized gold colloids (1.5-3nm) were attached to the silica particles through silica-bound amine groups. These gold seed particles serve as nucleation points for a homogenous gold shell growth over the particle surface by solution-phase reduction of $HAuCl_4$ by hydroxylamine hydrochloride. In order to produce particles with monodisperse shell thickness and to minimize secondary nucleation of unbound gold particles, the Halas protocols were modified to integrate purification by centrifugation and resuspension between each growth step. Results of this step-wise synthetic procedure are shown in Figure 1.11 b-e, where the C-dot seed is decorated

Figure 1.10 - Silica-cored gold nanoshell particles of various core-shell thicknesses demonstrating the variety of absorption wavelengths available through fine-tuning the particle geometry. Published with permission from: "Nanoshell-Enabled Photonics-Based Imaging and Therapy of Cancer," *Technology in Cancer Research and Treatment*, 3, 34, 2004, Adenine Press, http://www.tcrt.org/

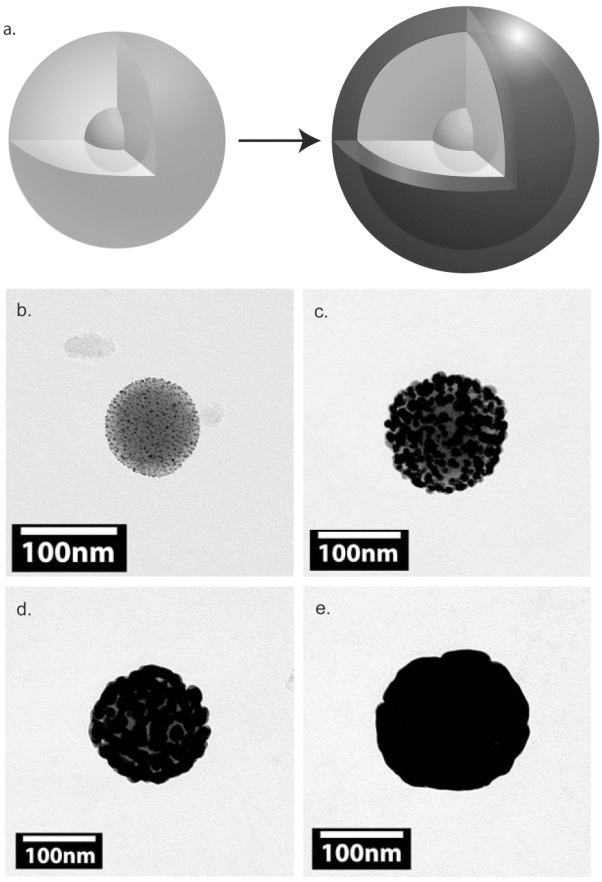


Figure 1.11 - (a) A schematic depiction of fluorescent core-shell silica nano-particles encapsulated in a gold nanoshell, and (b-e) representative transmission electron micrographs (TEM) of fluorescent core-shell-gold nanoshell particles grown by step-wise synthesis as described in the text.

with 1.5-3 nm gold colloids which grow into a complete metal shell over the course of the three growth steps. Future in-depth photophysical studies can now focus on elucidating the effects of the gold shells on the fluorescence properties of the encapsulated dyes as a function of silica and gold shell thicknesses and overall particle geometry.

In addition, with sufficient excitation power, the metal shell absorptions can be used to dramatically change the local temperature of the environment surrounding the gold nanoshell particles. The Halas and Price groups have recently used this technique to treat tumors within mice. Briefly, gold-coated silica nanoparticles tuned to absorb in the near infrared (820 nm) were injected into a subcutaneous tumor and were subsequently irradiated by a laser. The locations containing gold nanoshell particles increased in temperature by nearly 40ºC, effectively killing the tumor cells, while similarly irradiated areas without particles experienced a non-lethal increase of less than 10ºC (Figure 1.12a-c)[26,28].

### *1.5 Applications in Biology: The Field of Nanobiotechnology*

As demonstrated by this last example, an area of enormous scientific as well as technological promise is the application of nanomaterials in biotechnology and medicine. One of the most powerful paradigms of nanobiotechnology is the design of synthetic materials towards the molecular architecture of biomolecules for enhanced interactions and integration. Indeed, small size and high functionality of materials are keys to understanding the complex interactions in biology on the length scales of proteins, antibodies and organelles, from which future breakthroughs are expected. The combination of enhanced, tunable photophysical properties, variable core-shell architecture, and benign, biocompatible matrix chemistry (silica materials are inert and commonly used in a variety of food and cosmetic products) make silica nanoparticles

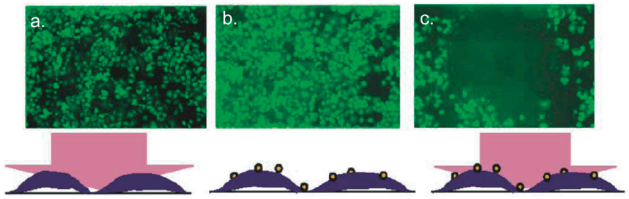


Figure 1.12 - Fluorescence microscopy imaging of human breast epithelial cells (a) irradiated by 820nm laser light, (b) exposed to gold nanoshell particles and (c) exposed to gold nanoshell particles and irradiated with 820nm light. The green fluorescence is calcein green which indicates cell viability. Photothermal exposure in (c) shows localized cell death in the irradiated spot. Published with permission from: "Nanoshell-Enabled Photonics-Based Imaging and Therapy of Cancer," *Technology in Cancer Research and Treatment*, 3, 39, 2004, Adenine Press, http://www.tcrt.org/

an ideal materials platform that can be tailored towards a wide array of applications in the life sciences.

In order to demonstrate the potential of any novel nanoparticle as a fluorescent probe, it is often instructive to use model biological systems. On the cellular level, Rat Basophilic Leukemia mast cells (RBL-2H3) are a robust and versatile cell line and are an excellent candidate for *in vitro* studies with nanomaterials[29]. Mast cells are a class of tissue cells, which are part of the first line of immunological defense in vertebrates. These cells are integral to the immune response to environmental stimuli such as allergens and bacteria, and are known to express cell-surface receptors for antibodies such as Immunoglobulin E (IgE). Upon IgE-binding and cross-linking, mast cells undergo a transformation from their resting state (Figure 1.13 a) to an activated state (Figure 1.13 b) with concomitant release of signaling molecules such as histamine, which mediate the allergic response throughout the body. The RBL-2H3 cells are a continuously-cultured cell line commonly used in studies of allergic response because they are easily sensitized towards various stimuli[29]. They will be employed as the biological model system in the remainder of this review.

### *1.5.1 Integrating Imaging with Targeting: C-Dot Antibody Conjugates*

One of the desirable features of a biological probe is that it can be targeted to a specific biological environment with minimal non-specific labeling. Surface functionalization of silica is well established and may be performed with an array of biologically active substances from small molecules to antibodies to create such probes. Indeed, various groups have demonstrated the use of antibodies, peptides and small molecules to mediate biological recognition[12]. An example of this concept for TRITC-based C dots was demonstrated through antibody-mediated labeling of cell surface receptors on RBL cells. Specifically, the work investigated the interaction

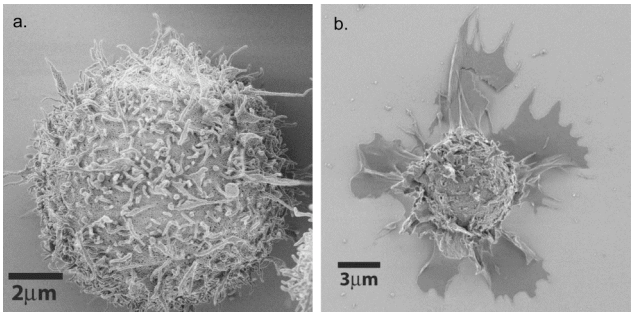


Figure 1.13 - Scanning electron micrographs of fixed Rat Basophilic Leukemia (RBL) mast cells in their (a) resting and (b) excited states.

between IgE antibodies and the FcεRI cell surface receptor. FcεRI is integral to the cell's response to foreign materials in the bloodstream and is known to form a strong, but reversible complex with IgE both *in vivo* and *in vitro*[30]. Upon exposure to an allergen, IgE antibodies specific to that allergen bind to and cross-link the FcεRI cell surface receptors. This initiates a signal cascade throughout the cell, ultimately leading to degranulation and release of histamine and heparin, the latter of which transduces further steps in the allergic response, which can eventually cause allergy symptoms throughout the body and thus a systematic response at the macroscopic length scale[29].

For these experiments, 30 nm diameter TRITC-based C dots were exposed to the IgE antibodies and allowed to bind via adsorption to the silica surface. These particle-antibody complexes were then incubated with RBL cells. It was found that they specifically attached to the cell surface via the IgE-FcεRI interaction schematically depicted in Figure 1.14 a. Representative results are shown as brightfield and confocal fluorescence images in Figure 1.14 b and c, demonstrating equatorial labeling of the cell membranes by the nanoparticle-antibody complexes. The images reveal even labeling levels across the whole cell membrane. As a control, cells were incubated with free IgE antibodies to quench the FcεRI receptors before incubation with the C dot-IgE complexes under the same conditions as above. These experiments revealed no appreciable cell surface binding after washing, as shown in the bright field and confocal fluorescence images in Figure 1.14 d and e[10]. The combination of specific targeting and the robust nature of these core-shell fluorescent silica nanoparticles creates an ideal tool for long-term studies such as determining the fate of antibodies or other proteins in a variety of biological systems.

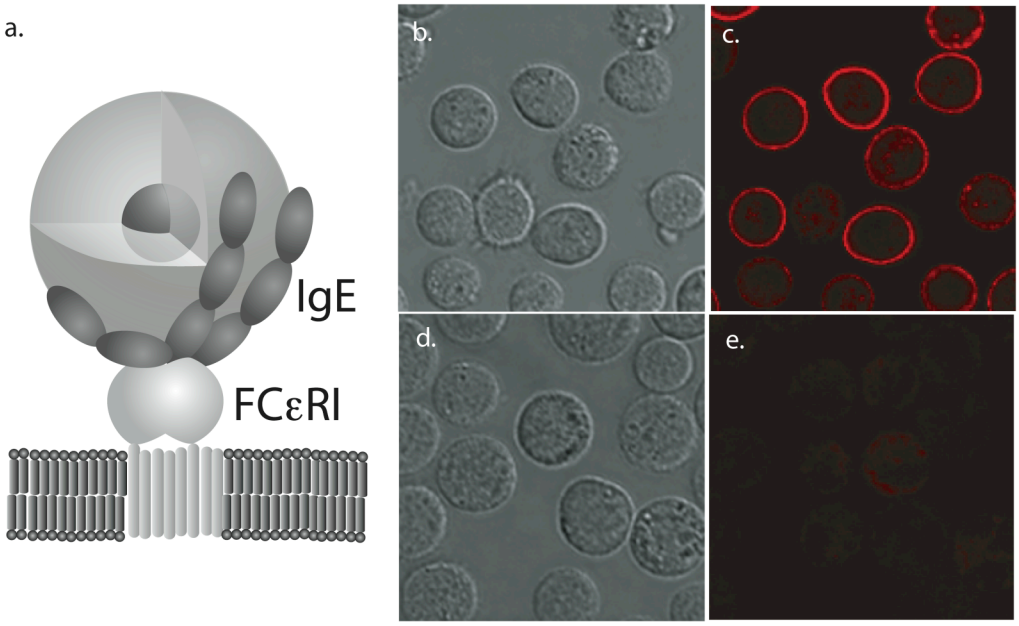


Figure 1.14 - A schematic illustration of a fluorescent core-shell silica nanoparticle non-covalently attached to an Immunoglobulin E (IgE) antibody specifically attached to the FceR1 cell surface receptor of an RBL cell, and (b) brightfield and (c) confocal fluorescence images of RBL cells with IgE mediated cell surface labeling. As a control (d) brightfield and (e) fluorescence images of RBL cells quenched with free IgE after exposure to C dot-antibody complexes showing minimal non-specific cell surface binding.

### *1.5.2 Integrating Imaging with Sensing: C Dot Sensors*

The final example of a highly functional core-shell architecture involves the development of C dot sensors for near-molecular scale chemical sensing, building on the bright and stable C dot platform to create environmentally-sensitive probes[31]. On the cellular and sub-cellular level, chemical gradients are crucial to the communication and function of living systems. The concentrations of ions such as $Na^+$, $Ca^{2+}$ and $H^+$ are very closely controlled in both space and time and changes in these concentrations can be indicative of such cellular activities as neural/muscular signaling, vesicle trafficking, or more broadly, overall cellular health. For example, within eukaryotic cells, materials (e.g. drugs, proteins) that are endocytosed by the cell are transported through a series of membrane-bound organelles known as endosomes, which transport their cargo throughout the cell. In many cases, materials that are taken up by the cell go through a series of membrane-bound vesicles with sequentially lower pH until reaching the lysosome where the foreign material is ultimately degraded in a low pH environment[32]. On a slightly larger scale, the rapid growth of tumor cells often outstrips the available blood supply, yielding an acidic and hypoxic environment within the growing tumor[33]. Thus, the ability to quantitatively image the concentrations of biologically active ions, such as $H^+$, are of major importance in understanding metabolic processes in both *in vitro* and *in vivo* experiments.

Ion concentrations such as pH are traditionally analyzed by macroscopic means, such as titration or probes such as litmus paper or electrochemical cells. These approaches lack the small size and spatial/temporal resolution to effectively probe ion concentrations within cells or tissues. Thus, a variety of approaches to nanoscale sensing have been developed which rely on analyte-specific effects on the wavelength, lifetime or quantum yield of fluorophore emission. The smallest assays are analyte-sensitive dyes, such as fluorescein (pH sensor) and Fluo-4 ($Ca^{+2}$ sensor)[2]. However,

the vast majority of these molecular sensors can only provide qualitative data, as the measured fluorescence intensity is dependent not only on the analyte concentration, but also on the concentration of the sensor[34]. Additionally, like all free dye molecules, they are limited in brightness and are prone to photobleaching, cellular toxicity and solvatochromic shifts[3].

To address these issues, several groups have begun developing particle-based hybrid systems incorporating a second dye species to create an internal standard, which allows the analyte concentration to be determined independent of the sensor concentration by analyzing the ratio between the two signals. This so-called ratiometric sensing enables quantitative chemical sensing down to the single nanoparticle level. Among the variations on this concept are polymer-based sensors, lipid vesicle-based sensors and silica-based sensors. Polymer-based sensors are currently the most common, including commercially-available dextran-based pH sensors[2] and the larger PEBBLE sensors developed by Kopelman and co-workers[35]. The PEBBLE sensors integrate sensor and reference dye molecules homogenously into a cross-linked polymer particle and although these particles integrate multiple dye molecules to increase individual probes' brightness, like all polymer-based probes, the dyes are given relatively little protection against quenching and leaching. Another approach, pursued by the Rosenzweig group, is the use of supported lipid bilayer vesicles as vehicles for the reference and sensor dyes. These microparticles provide a highly biocompatible alternative to polymers, though they lack the robustness and small size to effectively probe intracellular conditions[36]. To address some of these issues, the Kopelman group recently developed homogenously-dyed ratiometric nanoparticle sensors for dissolved oxygen based on sol-gel silica[37] which provides a more robust vehicle for the sensor dyes.

### *1.5.2.1 The Optimized Core-Shell Sensor Architecture*

The core-shell C dot architecture is ideally suited to the development of ratiometric fluorescent sensors on the nanoscale (Figure 1.15). By placing the internal reference dyes in the sequestered particle core environment, they are protected from external influences such as solvent and other large molecules, providing a stable reference signal. The sensor dyes can then be integrated covalently into the particle shell, protecting the reference dyes. Further, this arrangement affords the sensor dyes the benefits of attachment to the silica matrix, while exposing the sensors on the highest surface-area portion of the particle. This provides greater sensitivity and more uniform response than particles with sensor and reference dye molecules dispersed homogenously throughout the particle. As well, covalent attachment of both sensor and reference dyes minimizes dye leaching to create stable sensors with low background signal.

As proof-of-principle for this dual-emission core-shell sensor nanoparticle architecture, the Wiesner group developed a ratiometric pH sensor for quantitative *in vitro* chemical imaging and spectrofluorometric analysis[31]. Fluorescein isothiocyanate (FITC) was chosen as a pH sensor dye for its significant change in quantum yield upon protonation/deprotonation of the hydroxyl groups on the xanthene backbone of the dye. In the protonated, mono-anionic form, the dye exhibits a relatively low quantum yield of 36%, whereas upon deprotonation the quantum yield increases to 93% for the dianion form[2]. With a pKa of 6.4, this transition makes fluorescein an excellent sensor for pH in the biologically relevant range from pH 5-8.5. TRITC was chosen as the internal standard because its quantum yield is unaffected by pH changes in this realm. The TRITC-containing core particles were grown to 50 nm in size via a modified Stöber reaction, as shown in the scanning electron micrograph in Figure 1.16 a. FITC-based fluorescent silica precursors were synthesized and integrated into a 10

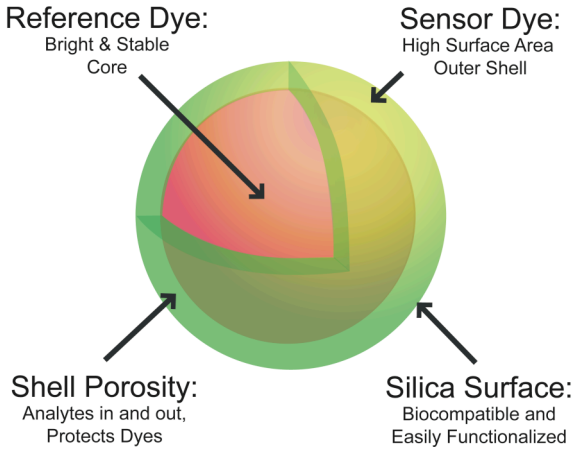


Figure 1.15 - A schematic illustration of the dual-emission core-shell nanoparticle sensor architecture highlighting several design advantages

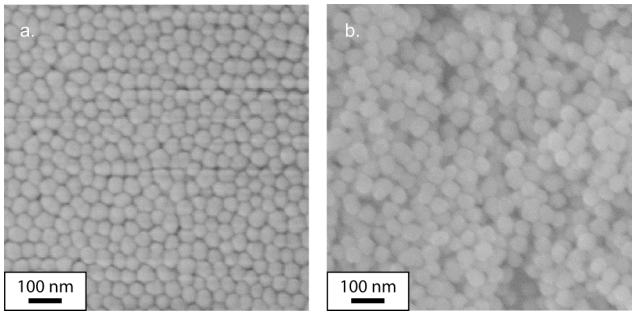


Figure 1.16 - Scanning electron microscopy images of (a) 50nm TRITC-based core particles and (b) 70nm dual-emission pH sensor nanoparticles incorporating fluorescein isothiocyanate as a sensor dye and TRITC as a reference dye. Reproduced with permission from *Small*, 2006, *2(1)*, 723-726, Copyright 2006, Wiley VCH

nm-thick shell layer around the TRITC cores to yield 70 nm core-shell sensor particles as shown in the SEM image in Figure 1.16 b. In both cases, monodisperse particles with smooth and uniform surfaces were produced. This particle size and architecture was chosen for ease of uptake into cells[38] as well as ease of handling during synthesis and characterization.

The pH-dependent spectra of the particles were analyzed by spectrofluorometry (Figure 1.17 a). The ratio between the peak emission intensities of the sensor and reference dyes were calculated for particles in a variety of pH calibrated phosphate buffer solutions (pH 5-8.5) and were plotted versus pH (Figure 1.17 b). The resulting calibration curve exhibits the typical behavior of a system in equilibrium between two states, in this case the mono- and di-anionic protonation states of fluorescein with a pKa at pH 6.4, which is in accordance with literature[2]. The particles were similarly analyzed on a confocal fluorescence microscope to develop a calibration curve for ratiometric imaging of pH.

#### *1.5.2.2 Intracellular Ratiometric pH Imaging*

An important goal of nanoparticle sensors is the ability to perform quantitative chemical measurements inside individual cells facilitating spatial and temporal mapping of metabolic parameters within the cell. To demonstrate the C dot sensor's capabilities, RBL mast cells were again chosen as a model system for their particle-uptake characteristics and several interesting pH-related biological questions that remain under investigation. Initial experiments were performed with single-emission TRITC core-shell particles of the same core-shell geometry as the sensors which showed that the RBL mast cells do not naturally uptake 70nm particles (Figure 1.18 a). Upon addition of phorbol (12,13) dibutyrate (PDB), however, the particles were rapidly endocytosed into various intracellular vesicles (Figure 1.18 b). PDB is a

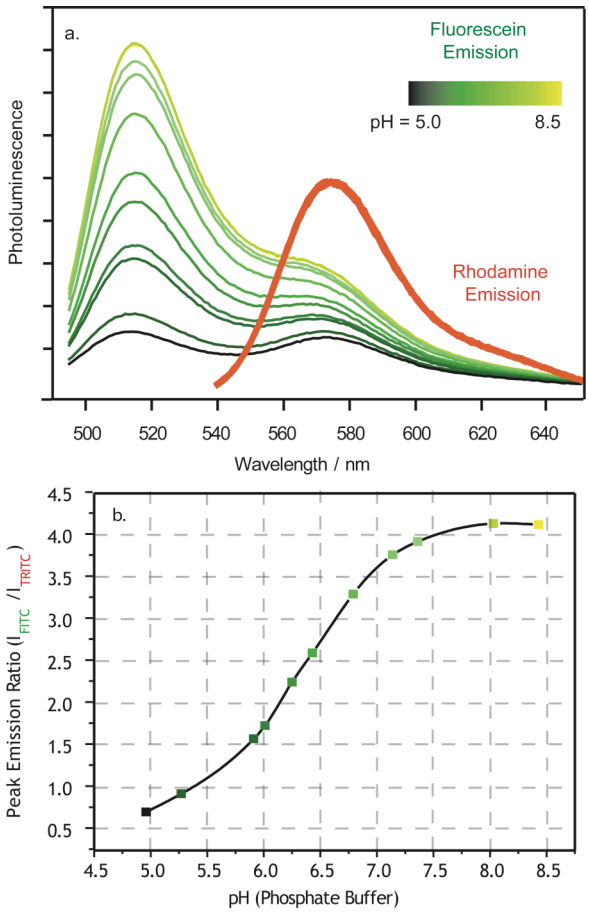


Figure 1.17 - (a) Spectrofluorometry data for 70nm dual-emission core-shell fluorescent silica nanoparticle pH sensors showing fluorescein (green) and TRITC (red) in phosphate pH calibration buffers from pH 5-8.5. (b) A ratiometric calibration curve based on the peak intensity ratio between fluorescein and TRITC across the pH range under investigation. Reproduced, in part, with permission from *Small*, 2006, *2(1)*, 723-726, Copyright 2006, Wiley VCH

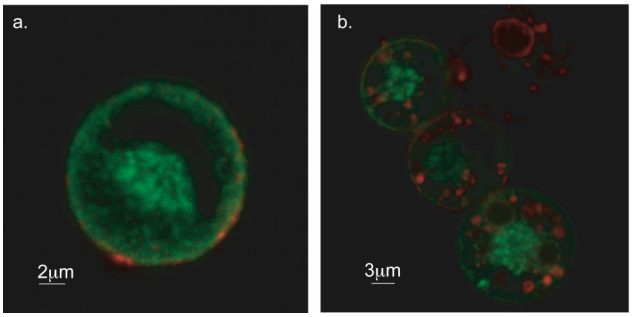


Figure 1.18 - (a) 70nm single-emission sensor particle analogs (red) incubated with RBL mast cells (green) and (b) 70nm single-emission sensor particle analogs (red) in intracellular vesicles following exposure to phorbol dibutryate. Reproduced with permission from *Small*, 2006, *2(1)*, 723-726, Copyright 2006, Wiley VCH

commonly used reagent in DNA transfection experiments and it is thought to stimulate macropinocytosis and concomitant uptake of membrane-associated and extracellular material[39].

The same uptake protocols were then followed for the dual-emission sensor particles that were readily endocytosed as well. Following uptake, the particles were trafficked into early endosomal compartments, which sort incoming material to various intracellular destinations. For the sensor nanoparticles, these early endosomes matured into late endosomes and eventually lysosomal compartments with much lower pH. This progression was imaged via confocal fluorescence microscopy as shown in Figure 1.19.

The reference and sensor channels were imaged using separate excitation to avoid spectral bleed-through as shown in Figure 1.19 a-b. The reference dye (TRITC) channel acts not only as an internal standard for pH measurements but also as an indication of particle location and local concentration allowing the particles to be tracked throughout the cell (Figure 1.19 a). The ratio between the sensor (Figure 1.19 b) and reference emission channels was calculated for each pixel and using the previously determined calibration curve, the corresponding pH values were represented in the false-spectrum image shown overlaid on a transmitted-light image of the cell in Figure 1.19 c. Various intracellular locations reveal pH values varying from ~pH 6.5 (early endosome) to late endosomal and lysosomal compartments with much lower pH values between 5-5.5. These results demonstrate the applicability of the concept of dual-emission core-shell silica sensor nanoparticles for investigating fundamental biology at the molecular level and open the door to further experiments building upon the specific targeting capabilities of these nanoparticles to investigate biological phenomena.

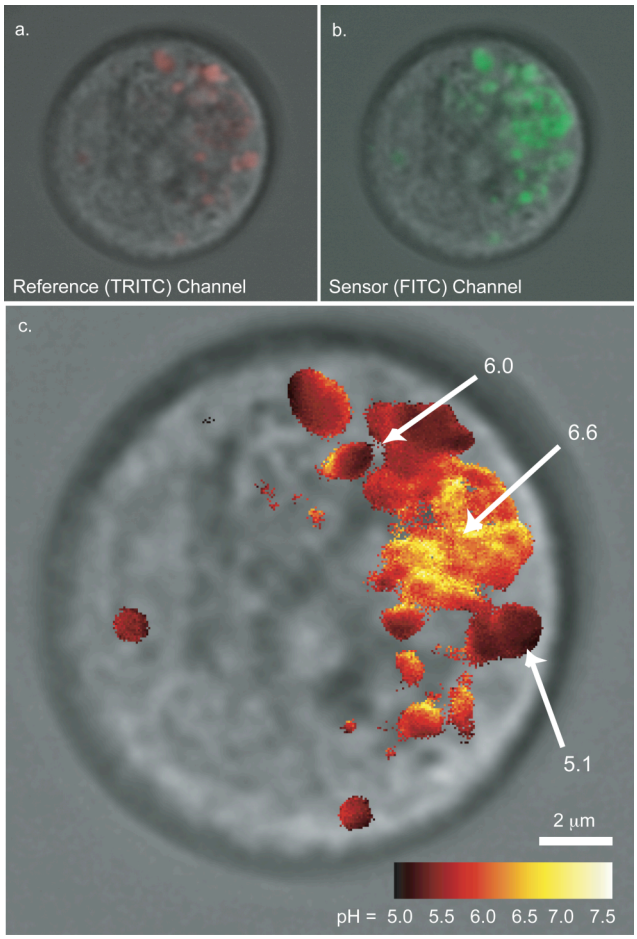


Figure 1.19 - Confocal fluorescence images of (a) red reference dye (TRITC) emission, (b) green sensor dye (fluorescein) emission as well as (c) quantitative ratiometric confocal imaging of pH within an RBL mast cell, all overlaid on brightfield cell images. Reproduced, in part, with permission from *Small*, 2006, *2(1)*, 723-726, Copyright 2006, Wiley VCH

This sensor architecture may be of particular importance in complex biological environments where many species can potentially interfere with sensing. Since many fluorophores with sensing capabilities are available, this approach may be generalized towards multiple analytes, including metal ions, oxygen, or redox status indicators. Cocktails of such particles may further allow high content imaging for high throughput drug screening whereby metabolic parameters of cells are monitored with high temporal and spatial resolution down to the molecular level.

### *1.6 Conclusions: Highly Integrated Particles - Towards "Lab on a Particle" Architectures and Single Particle Laboratories*

Throughout this review, a variety of functionalities have been introduced that demonstrate the versatility of silica as a host material for fluorescent dyes for many applications, specifically in the fields of nanobiotechnology and the life sciences. The power of silica as a host material is twofold. First, encapsulation of organic dyes in a silica matrix can enhance their stability and performance (*e.g.* brightness). Second, the ability to synthesize particles with core-shell architectures allows multiple functions to be brought together in a single vehicle, separated in different shells, for example, to minimize interference towards creating highly functional particles.

The first of these two points reveals an interesting aspect of nanotechnology, *i.e.* the ability to improve an existing technology through the application of small-scale structures and materials. As discussed in the first section of this review, organic dye molecules have been investigated for decades. Highly optimized, water-soluble organic dyes have been developed and are now commercially available for prices per weight much higher than that of gold. Enhancing the performance of dyes through encapsulation in water soluble core-shell silica nanoparticles may significantly reduce

costs and at the same time catapult performance characteristics of relatively inexpensive dyes to competitive levels.

The fluorescent core-shell silica nanoparticle design concepts exemplified by the sensors introduced in the last section hint at the possibilities available to researchers in the future. By combining such functionalities as antibody-mediated targeting, mesoporosity and chemical sensing already demonstrated individually, a "single-particle laboratory" or "lab on a particle" can be envisioned that would, for example, (a) seek out a specific cellular location, (b) deliver a payload of therapeutics and (c) subsequently monitor the cell's response. These particles would provide high-content feedback on the activity of the therapeutic agent, rather than simply monitoring whether or not the cells survived treatment, as is commonly the case today.

Many other such combinations can be envisioned, with more functionalities such as enzymatic catalysis or magnetism, that can be easily integrated. With the development of these and other functionalities, one can envision a "toolbox" of capabilities, which can be assembled in different shells to create probes tailored to explore specific biological questions at near-molecular scale. The versatility of silica as a host material and the modularity of the core-shell architecture thus provide a wide and open space for innovative research towards creating highly-integrated and highly-functional nanomaterials for nanobiotechnology and beyond.

### *1.7 Acknowledgements*

This review is based on several years of research on fluorescent silica nanomaterials performed at Cornell University. We would like to thank the following collaborators for their contributions to the research: Tara Zedayko, Daniel Bonner, Katherine Chin and Erik Herz for particle synthesis; Daniel Larson and Watt Webb for photophysical characterization; Mamta Srivastava, Prabuddha Sengupta and Barbara

Baird for cellular application of the particles; Mark Saltzman for drug release studies; and Carol Bayles and Malcolm Thomas for their oversight on confocal fluorescence and scanning electron microscopy, respectively. Funding for this research included grants from the Cornell Center for Materials Research (CCMR – NSF MRSEC DMR 0520404), the National Science Foundation (NSF – NSF grants: NIRT 0404195, DBI-0080792), Phillip Morris USA and the Cornell Nanobiotechnology Center (NBTC – STC Agreement No. ECS-9876771). Finally, we would like to thank Gil Toombes for rendering the MCM-48 structures shown in this review as well as Erik Herz for fruitful discussions and careful reading of the manuscript.

REFERENCES


[1] F. Wang, W. Tan, Y. Zhang, X. Fan, M. Wang, *Nanotechnology*, 2006, *17*, R1-R13 (and references therein).

[2] R. P. Haugland, *The Handbook – A Guide to Fluorescent Probes and Labeling Technologies*, Molecular Probes, Eugene, OR, 10th edn., 2005

[3] J. R. Lakowicz, *Principles of Fluorescence Spectroscopy*, Kluwer Academic, New York, 2nd edn., 1999.

[4] T. Maka, S. G. Romanov, M. Muller, R. Zentel, C. S. Torres, *Phys. Stat. Sol.* 1999, 215, 307-312.

[5] R. Tsien, *Ann. Rev. Biochem.*, 1998, *67*, 509-544.

[6] I. Medintz, H. Uyeda, E. Goldman, H. Mattoussi, *Nat. Mater.*, 2005, 4, 435-446.

[7] A.M. Derfus, W. C. W. Chan, and S. N. Bhatia, *Nano Lett.*, 2004, 4, 11-18.

[8] J. Yao, D. Larson, H. Vishwasrao, W. Zipfel, W. Webb, *P. Nat. Acad. Sci. USA*, 2005, 102, 14284-14289.

[9] T. Pellegrino, S. Kudera, T. Liedl, A. Javier, L. Manna, W. Parak, *Small*, 2005, 1, 48-63.

[10] H. Ow, D. Larson, M. Srivastava, B. Baird, W. Webb, U. Wiesner, *Nano Lett.*, 2005, *5*, 113-117.

[11] F. J. Arriagada, K. Osseo-Asare, *J. Colloid Interf. Sci.*, 1995, 170, 8-17.

[12] L. Wang, K. Wang, S. Santra, X. Zhao, L. Hilliard, J. Smith, Y. Wu, W. Tan, *Anal. Chem.*, 2006, 646-654.

[13] W. Stöber, A. Fink, E. Bohn, *J. Colloid Interf. Sci.*, 1968, 26, 62-69.

[14] G. H. Bogush, M. A. Tracy, C. F. Zukoski, *J. Non-Cryst. Solids*, 1988, 104, 95-106.

[15] A. van Blaaderen, A. Vrij, *J. Colloid Interf. Sci.*, 1993, 156, 1-18.

[16] S. Hess, S. Huang, A. Heikal, W. W. Webb, *Biochemistry*, 2002, 41, 697-705.

[17] W. Zipfel, R. Williams, W. W. Webb, *Nat. Biotech.*, 2003, 21, 1369-1377.

[18] H. Ow, Ph.D. Thesis, Cornell University, 2005.

[19] D. Larson, H. Ow, H. Vishwasrao, A. Heikal, U. Wiesner, W. Webb, *Chem. Mater.* 2008, *8(20)*, 2677-2684

[20] E. Herz, D. Bonner, U. Wiesner, in preparation

[21] E. Herz, A. Burns, S. Lee, P. Sengupta, D. Bonner, H. Ow, C. Liddell, B. Baird, U. Wiesner, *Proc. of SPIE*, 2006, 6096, 609605.

[22] C. T. Kresge, M. E. Leonowicz, W. J. Roth, J. C. Vartuli, J. S. Beck, *Nature,* 1991, *359*, 710-712.

[23] M. Vallet-Regi, L. Ruiz-Gonzalez, I. Izquierdo-Barba, J. Gonzalez-Calbet, *J. Mater. Chem.*, 2006, 16, 26-31.

[24] Y-S. Lin, C-P. Tsai, H-Y. Huang, C-T. Kuo, Y. Hung, D-M. Huang, Y-C. Chen, C-Y. Mou, *Chem. Mater.*, 2005, 17, 4570-4573.

[25] K. Schumacher, P. Ravikovitch, A. Du Chesne, A. Neimark, K. Unger, *Langmuir*, 2000, *16*, 4648–4654.

[26] C. Loo, A. Lin, L. Hirsch, M-H. Lee, J. Barton, N. Halas, J. West, R. Drezek, *Technol. Cancer Res. T.*, 2004, 3, 33-40. and references therein.

[27] J. Enderlein, *Appl. Phys. Lett.*, 2002, 80, 315–317.

[28] J. Hirsch, R. Stafford, J. Bankson, S. Sershen, B. Riviera, R. Price, J. Hazle, N. Halas, J. West, *Proc. Nat. Acad. Sci. USA,* 2003, 100, 13549-13554.

[29] D. Holowka, B. Baird, *Annu. Rev. Biophys. Biomol. Struct.*, 1996, 25, 79-112.

[30] P. Schwille, U. Haupts, S. Maiti, W. W. Webb, *Biophys. J.*, 1999, 77, 2251-2265.

[31] A. Burns, P. Sengupta, T. Zedayko, B. Baird, U. Wiesner. *Small*, 2006, 2, 723-726.

[32] H. Lodish, A. Berk, S. Zipursky, P. Matsudaira, D. Baltimore, J. Darnell, *Molecular Cell Biology*, W.H. Freeman, New York, 4th edn., 1999.

[33] P. Carmeliet, R. Jain, *Nature*, 2000, 407, 249-257.

[34] Z. Gryczynski, I. Gryczynski, J. R. Lakowicz, *Method. Enzymol.* 2003, 360, 44-75.

[35] S. M. Buck, Y.-E. L. Koo, E. Park, H. Xu, M. A. Philbert, M. A. Brasuel, R. Kopelman, *Curr. Opin. Chem. Biol*. 2004, 8, 540-546.

[36] A. Ma, Z. Rosenzweig, *Anal. Bioanal. Chem*., 2005, 382, 28-36

[37] H. Xu, J. W. Aylott, R. Kopelman, T. J. Miller, M. A. Philbert, *Anal. Chem*. 2001, 73, 4124-4133.

[38] W. Zauner, N. Farrow, A. Haines, *J. Control. Release*, 2001, 71, 39-51.

[39] C. Ra, K. Furuichi, J. Riviera, J. Mullins, C. Isersky, K. White, *Eur. J. Immunol*., 1989, 19, 1771-1777.

# CHAPTER 2

# CORE-SHELL FLUORESCENT SILICA NANOPARTICLES FOR CHEMICAL SENSING: TOWARDS SINGLE PARTICLE LABORATORIES*


## *2.0 Abstract*

In this chapter, a fluorescent chemical sensor platform is introduced based upon a core-shell architecture of sol-gel silica nanoparticles. Through covalent attachment of organic reference dyes within the particle core and sensor dyes incorporated in the outer shell, optimal sensor architectures can be realized. This design protects the internal dyes from perturbations to create a stable reference signal against which the sensor dyes may be compared. The sensor dyes' location in the surface shell offers maximal exposure to analytes in the environment, while the silica matrix acts as a filter to prevent interactions with large, interfering molecules that could perturb the measurements. As well, the silica provides a robust, biocompatible and stabilizing scaffold for the sensor. As a proof of principle, ratiometric pH sensors were developed and tested in vitro to measure pH following uptake into Rat Basophilic Leukemia cells. The concepts and synthetic control demonstrated here pave the way towards the development of highly functional particle architectures with catalytic or synthetic abilities in addition to sensors located in concentric shells to create single particle laboratories with myriad potential applications.



* Originally Published as: Andrew Burns, Prabuddha Sengupta, Tara Zedayko, Barbara Baird, Ulrich Wiesner. "Core-Shell Fluorescent Silica Nanoparticles for Chemical Sensing: Towards Single Particle Laboratories," *Small*, **2006**, *2(6)*, 723-726, Reprinted with permission of Wiley VCH

### *2.1 Introduction*

Photoluminescence has been shown to be an excellent tool to investigate biology down to the molecular scale, due to its high signal-to-noise ratio, excellent spatial resolution and ease of implementation[1]. The interactions and conditions in this realm of enzymes, antibodies and nucleotides are integral to the higher order function seen throughout nature. A variety of probes have been developed in recent decades to explore these environments, from organic and metallorganic dye molecules to semiconductor nanoparticles[2], fluorescent proteins[3], and hybrid systems[4]. There is great interest among biologists to explore the chemical microenvironments found on the cellular and molecular scales to determine quantitative chemical concentrations both *in vivo* and *in vitro*[5]. For example, the rapid growth of cancer cells in tumors outstrips the available blood supply, leading to hypoxic and acidic conditions within the tumor, the detection of which could provide a route to early cancer screening[6]. Focusing deeper to individual cells, the local concentrations of ions such as $Na^{+}$, $Ca^{+2}$, $H^{+}$ and others are indicative of signal transduction[7] as well as general cellular health.

Traditionally, environmental factors such as pH have been analyzed by titration or probes such as litmus paper or electrochemical cells. These approaches fail at small length scales and in complex environments such as those found in living cells and tissues. Thus, a variety of approaches to sensing have been developed which rely on analyte-specific effects on the wavelength[8], lifetime[9] or quantum yield[10], of fluorophore emission. The smallest such assays are environmentally-sensitive fluorophores, such as fluorescein (pH sensor) and Fluo-4 ($Ca^{+2}$ assay)[11]. Unfortunately, most of these molecular sensors are effective only as qualitative sensors, as their measured fluorescence intensity is dependent upon sensor concentration as well as analyte concentration[12]. Additionally, like all free dye molecules, they are limited in brightness and are prone to photobleaching, non-specific quenching, solvatochromic

effects and cellular toxicity[1]. Particle-based hybrid systems incorporating an internal standard allow researchers to deconvolve global sensor concentration from local analyte concentration, enabling quantitative chemical sensing down to the single nanoparticle level.

Among the variations on this concept are polymer-based sensors, lipid vesicle-based sensors and silica-based sensors. Polymer-based sensors are currently the most common, including commercially available dextran-based pH sensors[11] and the larger PEBBLE sensors developed by Kopelman and co-workers[13]. These sensors integrate sensor and reference dye molecules into a polymer matrix to create a biocompatible particle. Though these particles can integrate multiple dye molecules to increase individual probes' brightness, the polymer network affords the dyes relatively little protection against quenching or leaching, and in some cases may decrease the quantum yield of the dye molecules. Another approach, pursued by the Rosenzweig group, is the use of supported lipid bilayer vesicles as vehicles for the reference and sensor dyes. These microparticles provide a highly biocompatible alternative to polymers, though they lack the robustness and small size to effectively probe intracellular conditions[14,15]. To address these issues, the Kopelman group developed ratiometric nanoparticle sensors for dissolved oxygen based on sol-gel silica[16] which provides a robust vehicle for the sensor dyes as well as a biocompatible and easily functionalized outer surface.

The Wiesner group recently developed a class of monodisperse fluorescent core/shell silica nanoparticles with a host of beneficial properties and very small dimensions[4]. Briefly, these particles integrate covalently-bound dyes[17] in a sol-gel-derived silica matrix. The particles are assembled in a core/shell architecture via a modified Stöber synthesis[18] with the dye molecules sequestered within the particle core, which is enclosed in a layer of pure silica. This architecture leads to a variety of

enhanced properties, including reduced photobleaching, minimized solvatochromic shift and increased fluorescent efficiency relative to free dye in aqueous solution[4]. Further, this design allows co-localization of multiple fluorophores within a single particle. This not only significantly increases per-particle brightness, but also facilitates long-term single particle tracking because the encapsulated dye molecules are decoupled from each other[19] and thus are not prone to the intermittent "blinking" under continuous excitation suffered by single emitter systems such as GFP[20] or quantum dots[21]. Finally, the silica shell lends itself to biological applications, as silica is highly biocompatible[22] and easily functionaled for biological targeting via proteins, antibodies or cell-penetrating peptides[23].

Building upon the benefits of our core/shell nanoparticle design concept, here we report a class of quantitative chemical sensors based on the co-localization of sensor and reference dye molecules concentrically within a single particle (Figure 2.1a). By coating a reference dye-rich core in a thin layer of sensor dye-rich silica, a sensor with optimal geometry may be realized which sequesters the reference while providing the greatest possible surface area for sensor interactions. In addition, the shell's silica matrix acts as a filter, allowing analyte molecules to diffuse to and from the sensor dyes, while protecting the dyes from interactions with larger molecules such as proteins or organic quenchers that could interfere with the measurements.

### *2.2 Results & Discussion*

As a proof of concept, we developed a silica-based pH sensor based on the pH-dependent change in quantum efficiency exhibited by fluorescein with tetramethylrhodamine as an internal standard. Fluorescein exists in several protonation states with changing pH. Of particular importance for this work is the equilibrium between the monoanionic and dianionic forms (pKa = 6.4). The

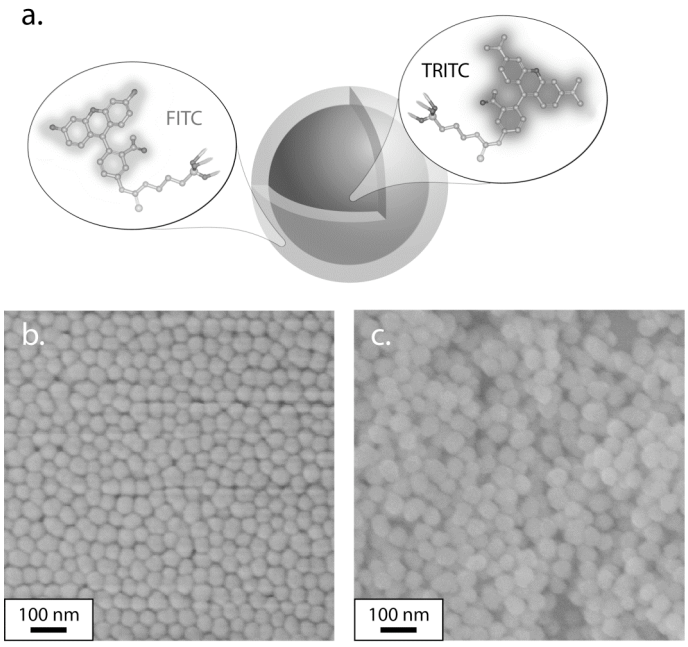


Figure 2.1 - A schematic diagram (a) showing the core/shell architecture of these sensor nanoparticles highlighting the reference dye sequestered in the core coated by a sensor-dye rich shell. SEM images of (b) 50 nm core and (c) 70nm core/shell particles.

monoanion has a low quantum yield of $\phi = 0.37$, while the dianion has a quantum yield of $\phi = 0.93$[11].

These particles were synthesized via a modified Stöber synthesis[18] incorporating reference and sensor dyes covalently bound to the matrix in the core-shell architecture depicted in Figure 2.1a. The reference dye, tetramethyrhodamine isothiocyanate (TRITC, Molecular Probes, Eugene, OR) was conjugated to the silica precursor 3-aminopropyltriethoxysilane (APTS, Gelest, Morrisville, PA) in an anhydrous nitrogen environment[17]. This conjugate was then hydrolyzed and condensed in basic ethanolic solution with a pure silica precursor, tetraethoxysilane (TEOS, Sigma-Aldrich, St. Louis, MO) catalyzed by concentrated aqueous ammonia (Sigma-Aldrich). The reagent concentrations were estimated from the empirical formula of Bogush *et al*[24]. Following the synthesis of these core particles, the sensor dye, fluorescein, in the form of fluorescein isothiocyanate (FITC, Sigma-Aldrich), was conjugated with APTS under similar conditions. The sensor dye precursor was then hydrolyzed with further TEOS to form the sensor layer. Following synthesis, the particles were centrifuged and resuspended repeatedly in ethanol and finally deionized water, in which they remain stable against flocculation, leaching and degradation for months at a time.

The particles were characterized via Scanning Electron Microscopy (LEO 1550 FE-SEM) and Dynamic Light Scattering (Horiba LB-550), which showed monodispersed 50nm dye-rich core particles (Figure 2.1b), encapsulated in a 10nm sensor dye-rich layer to create 70nm core-shell sensor particles (Figure 2.1c). The particles were then characterized via spectrofluorometry (PTI Quantamaster) to calibrate the ratiometric pH response in sodium phosphate buffer solutions with pH values between pH 5.0 and 8.5 as depicted in Figure 2.2[25]. The resulting calibration curve (Figure 2.2b) exhibits the typical behavior of a system in equilibrium between

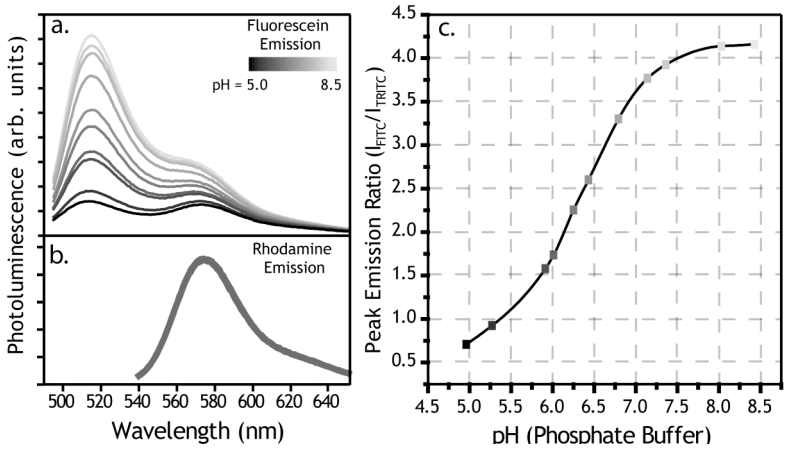


Figure 2.2 - pH sensor calibration via spectrofluorometry. (a) Fluorescein (sensor) emission spectra collected for solutions of known pH from 5.0 to 8.5 (b) Tetramethylrhodamine (reference) emission spectra for solutions of known pH from 5.0-8.5 (c) Ratiometric calibration curve showing peak sensor emission intensity (525 nm) divided by peak reference emission intensity (575 nm) versus pH.

two states, in this case the mono- and di-anion states of fluorescein and shows an effective pKa at pH 6.4 which corroborates well with the literature value[11]. For intracellular application, the particles were similarly calibrated on a confocal laser-scanning fluorescence microscope (Leica TCX SP2). We confirmed that there was no bleed-through between channels by the excitation wavelengths and emission filter set used[26].

To demonstrate the intracellular sensing capabilities of these particles, we chose to implement them in Rat Basophilic Leukemia Mast Cells[27,28] (RBL-2H3) to investigate the pH of various intracellular compartments. Physical analogues of the sensor particles (TRITC in 70nm silica) bound to the cell surface after incubation, but they were not internalized by the cells as observed with cells counter-labeled with Alexa488-Cholera toxin B (Figure 2.3a). Phorbol (12,13) dibutyrate, a compound known to increase endocytotic activity[29,30], was added during the incubation and was found to successfully stimulate particle uptake (Figure 2.3b). These uptake protocols were then applied to the sensor particles to mediate their endocytosis. Following uptake, the particles were monitored by confocal microscopy and found to reside in various intracellular compartments with pH values ranging from 5.1 to 6.6 as shown, for example, in Figure 2.4. The sensor and reference channels showed no bleed-through and were corrected for a small amount of cell autofluorescence. The pixel ratios (green/red) in these equatorial images were analyzed via MATLAB 6.12 (The MathWorks, Natick, MA) and superimposed in Adobe Photoshop 7.0 (Adobe Systems, San Jose, CA) to yield the images shown in Figure 2.4. The reference dye channel (TRITC – Figure 2.4a) acts not only as an internal standard for pH measurements but also as an indicator of particle location and concentration throughout the cell. Pixel-wise ratios between sensor (FITC – Figure 2.4b) and reference intensities were taken for all points of the cell with detectable reference

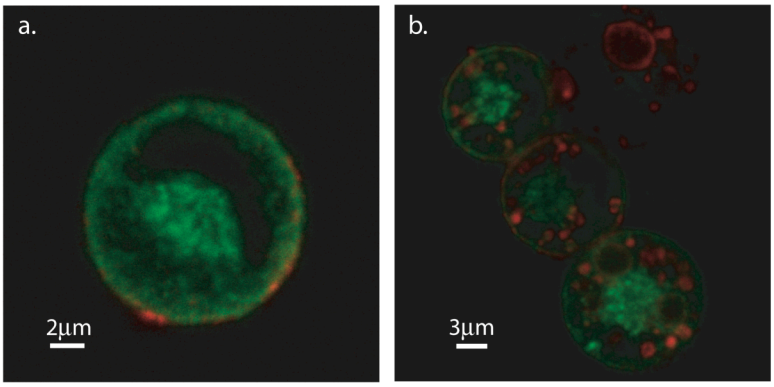


Figure 2.3 - Confocal fluorescence microscopy images of 70nm TRITC silica particles (red) and AlexaFluor 488-Cholera toxin B (green) in RBL Mast Cells. (a) 70nm fluorescent silica nanoparticles do not experience spontaneous uptake after incubation with cells at 37ºC for 1 hr, while (b) the same particles are endocytosed as a result of simultaneous incubation of cells with particles with phorbol (12,13) dibutyrate.

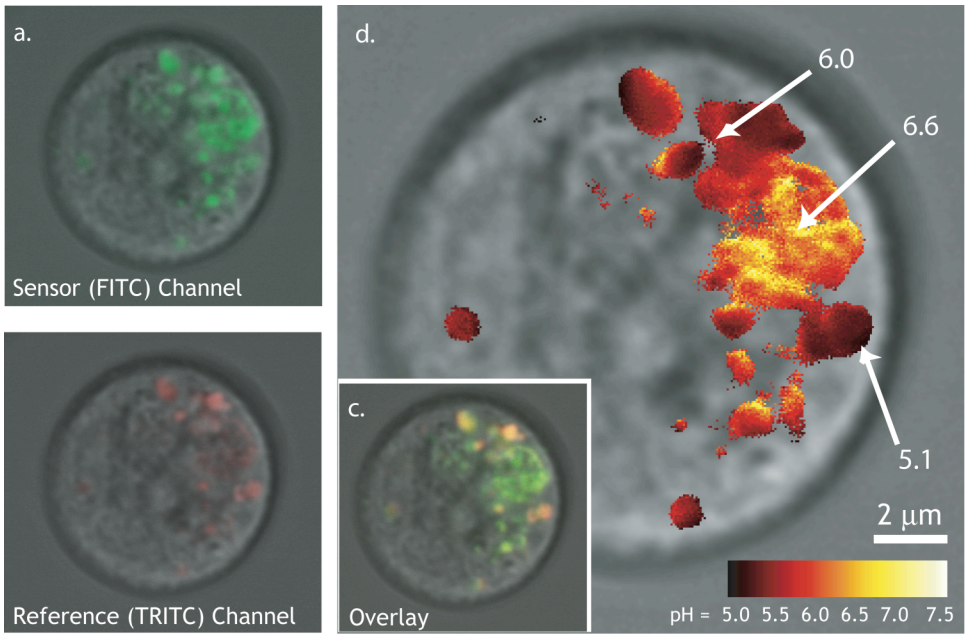


Figure 2.4 - Confocal fluorescence microscopy images (overlaid on brightfield) of pH sensors in RBL Mast Cells showing (a) reference dye channel, (b) sensor dye channel (c) overlaid images and (d) false-color ratiometric imaging of pH in various intracellular compartments.

fluorescence and the pH was thus imaged throughout the confocal image plane as shown in Figure 2.4d. Various intracellular locations are found to have pH values varying from ~pH 6.5 (early endosome) to late endosomal and lysosomal compartments with much lower pH values between 5.0-5.5. These initial experiments show the potential for core-shell silica sensor nanoparticles in investigations of fundamental biology and a variety of other fields.

### *2.3 Conclusions & Outlook*

This is the first demonstration of a silica-based core-shell fluorescent pH sensor comprising a shell of covalently-bound sensor dye molecules surrounding a core of sequestered, covalently-bound reference dye molecules. This architecture maximizes surface area for analyte exposure while effectively sequestering the reference dyes to permit quantitative ratiometric analysis of pH *in vitro*. This concentric core-shell architecture may be expanded to integrate new functionalities such as chemically reactive centers, catalytic sites[31] and/or surfactant-templated mesoporosity[32] to create highly sensitive particles capable of in situ chemical transformations and detection of analytes, thus leading to "single particle laboratories." It is expected that such optimized single nanoparticle sensor architectures will provide a unique platform to monitor metabolic status within cells both in vitro and in vivo with potential applications in fundamental biology, biomedicine and high-throughput pharmaceutical screening.

REFERENCES


[1] J. R. Lakowicz, *Principles of Fluorescence Spectroscopy 2nd Ed*., Kluwer Academic, New York, **1999**

[2] I. L. Medintz, H. T. Uyeda, E. R. Goldman, H. Matoussi, *Nat. Mater*. **2005**, *4*, 435-436

[3] 0. Shimomura, *FEBS Lett*. **1979**, *104*, 220-222

[4] H. Ow, D. R. Larson, M. Srivastava, B. A. Baird, W. Webb, U. Wiesner, *Nano Lett.* **2005**, *5*,113-117

[5] H. Ro, J. H. Carson, *J. Biol. Chem*. **2004**, *279*, 37115-37123

[6] P. Carmeliet, R. K. Jain, *Nature*, **2000**, *407*, 249-257

[7] R. Tsien, *Am. J. Physiol*. **1992**, *263*, C723-C728

[8] Z. Murtaza, Q. Chang, G. Rao, H. Lin, J. R. Lakowicz, *Anal. Biochem*. **1997**, *247*, 216-222

[9] H. Lin, H. Szmacinski, J.R. Lakowicz, *Anal. Biochem*. **1999**, *269*, 162-167

[10] C. C. Woodroofe, S. J. Lippard, *J. Am. Chem. Soc*. **2003**, *125*, 11458-11459

[11] R. P. Haugland, *The Handbook – A Guide to Fluorescent Probes and Labeling Technologies, Tenth Edition*, Molecular Probes, Eugene, OR, **2005**

[12] Z. Gryczynski, I. Gryczynski, J. R. Lakowicz, *Method. Enzymol*. **2003**, *360*, 44

[13] S. M. Buck, Y.-E. L. Koo, E. Park, H. Xu, M. A. Philbert, M. A. Brasuel, R. Kopelman, *Curr. Opin. Chem. Biol.* **2004**, *8*, 540-546

[14] T. Nguyen, Z. Rosenzweig, *Anal. Bioanal. Chem.,* **2002**, *374*, 69-74

[15] A. Ma, Z. Rosenzweig, *Anal. Bioanal. Chem*., **2005**, *382*, 28-36

[16] H. Xu, J. W. Aylott, R. Kopelman, T. J. Miller, M. A. Philbert, *Anal. Chem*. **2001**, *73*, 4124-4133

[17] A. van Blaaderen, A. Vrij, *J. Colloid Interf. Sci.* **1993**, *156*, 1-18

[18] W. Stöber, A. Fink, E. Bohn, *J. Colloid Interf. Sci.* **1968**, *26*, 62-

[19] D. R. Larson. *Optical Approaches to the Study of Nanoparticles and Biology: Quantum Dots, Silica Dots and Retroviruses,* **2004**, Cornell University, Ithaca, NY

[20] R. M. Dickson, A. B. Cubitt, R. Y. Tsien, W. E. Moerner, *Nature*, **1997**, *388*, 355-358

[21] R. G. Neuhauser, K. T. Shimizu, W. K. Woo, S. A. Empedocles, M. G. Bawendi, *Phys. Rev. Lett.* **2000**, *85*, 3301-3304

[22] J. Choi, A. Burns, R. Williams, Z. Zhou, A. Flesken-Nikitin, W. Zipfel, U. Wiesner, W. Zipfel, A. Nikitin, *J. Biomed. Optics*, 2007, 12(6), 064007 (1-13)

[23] A. Webster, S. J. Compton, J. W. Aylott, *Analyst*, 2005, *130*, 163-170

[24] G. H. Bogush, M. A. Tracy, C. F. Zukoski, *J. Non-Cryst. Solids*. 1988, *104*, 95-106

[25] See Appendix A Section A.1

[26] See Appendix A Section A.2

[27] L. Pierini, D. A. Holowka, B. Baird. *J. Cell Biol*. 1996, ***134*,** 1427–1439

[28] See Appendix A Section A.3

[29] C. Ra, K. Furuichi, J. Riviera, J. Mullins, C. Isersky, K. White, *Eur. J. Immunol*. **1989**, *19*, 1771-1777

[30] A. Alcover, B. Alarcon, *Crit. Rev. Immunol*. **2000**, *20*, 325-346

[31] D. R. Rolison, *Science*. **2003**, *299*, 1698-1701

[32] K. Suzuki, K. Ikari, H. Imai, *J. Am. Chem. Soc*. **2003**, *126*, 462-463

# CHAPTER 3

# REVERSE MICROEMULSION ROUTES TO CORE-SHELL FLUORESCENT SILICA NANOPARTICLES FOR pH AND CALCIUM SENSING[*]

## *3.0 Abstract*

This chapter presents an alternative method for the synthesis of core-shell silica-based sensor particles for pH and $Ca^{2+}$ using a seeded reverse microemulsion method. We demonstrate successful incorporation of dextran-bound fluorescein and Calcium Green™ sensor dyes into a coronal silica shell surrounding a reference-dye rich core as an alternative to covalent attachment of the sensor dye to the silica matrix. The effects of various synthetic parameters on particle size and dye incorporation are investigated. The reverse microemulsion synthetic protocol is generalizable towards the development of multiple ratiometric sensor particles with sensitivity to different analytes.

[*] Prepared for Submission as: Andrew Burns, Yoong Kim, Ulrich Wiesner. "Reverse Microemulsion Routes to Core-Shell Fluorescent Silica Nanoparticles for pH and Calcium Sensing"

### *3.1 Introduction*

In biology, the desire to study biomolecules such as proteins, enzymes and nucleic acids on the molecular level and to probe the chemical microenvironments within cells and tissues has fueled the development of novel imaging tools[1,2] and techniques[3-5] that provide high signal-to-noise ratios and fine spatial resolution as well as facile implementation. One of the most useful approaches for investigating the cellular and subcellular milieux is fluorescence, which is known for its versatility, sensitivity and high spatial resolution[3,6]. The advent of bright and stable fluorescent nanomaterials such as quantum dots[7] and hybrid fluorescent nanoparticles[8,9] has the potential to reshape the use of fluorescence in biology. In particular, hybrid particles based on polymeric or inorganic matrices allow for the incorporation of multiple, independent emitters, permitting, *e.g.*, the development of quantitative chemical sensors[10,11]. The ability to determine local chemical concentration data in addition to the spatial and temporal information available from single-emission probes may be of great benefit in fields from fundamental biology and drug development to diagnostic and clinical applications.

A host of probes exist today for labeling and staining biomolecules, including organic and metallorganic dyes[12], fluorescent proteins[13], quantum dots[7] and hybrid organic/inorganic particles[8,14-16]. For biological applications, fluorescent probes must not only exhibit bright and stable emission, but also must minimize the perturbation to the biological system under investigation. Each class of fluorescent probes approaches these challenges differently and has their own specific advantages and disadvantages as reviewed elsewhere[17].

Many environmental factors can change the peak wavelength, lifetime and efficiency of a dye, including solvent polarity, pH, oxygen and ion concentrations[18].

While many dyes have been designed to be relatively immune to these influences, there are a number of sensor dyes which are susceptible to specific environmental cues[6]. The most commonly used sensor dyes exhibit a change in quantum yield upon interaction with an analyte and are used as intensity-based probes. Unfortunately, the measured intensity of these fluorophores is dependent on the sensor dye concentration as well as the analyte concentration; thus, in situations where the dye concentration is unknown locally (*e.g.* intracellular imaging), they can function only qualitatively. In order to generate quantitative concentration data, the sensor dye concentration must be determined, which can be easily accomplished by co-localization of the sensor dye with an environmentally insensitive reference emitter to create a so-called ratiometric sensor[19].

One of the more common methods of preparing ratiometric sensors involves the use of hybrid particle systems incorporating multiple organic or organometallic dyes in a polymeric or inorganic matrix. By co-localizing the sensor and reference dyes, these architectures allow quantitative measurements to be performed down to the single-nanoparticle level. Kopelman and co-workers have developed a variety of sensors based on the PEBBLE concept (Probes Encapsulated By Biologically Localized Embedding) that integrate sensor and reference dye molecules homogenously throughout a polymeric or inorganic particle[20,21]. Although incorporating multiple dye molecules can increase the brightness of individual probes, a polymer network provides minimal protection against quenching and bleaching of the dye molecules, which may complicate their use in long-term sensing.

The Wiesner group has developed a class of core-shell fluorescent silica nanoparticles, with narrow size distributions, known as C dots, with hydrodynamic radii from several nanometers to microns, enhanced photostability, and per-particle brightness levels approaching those of quantum dots of similar hydrodynamic size and

wavelength[2, 8, 15, 22]. Based on a modified Stöber silica synthesis, these core-shell particles incorporate multiple organic fluorophores into an amorphous silica core through the covalent coupling of organosilicate precursors to reactive dye molecules[8,23,24]. To this core, additional pure silica is added to form a protective silica shell. The silica shell imparts biocompatibility and enables surface functionalization with a variety of biomolecules such as proteins, antibodies and peptides for biological targeting independent of emission wavelength[2, 8, 14].

Building on the bright and stable C dot architecture, the Wiesner group has developed a class of quantitative chemical sensors known as C dot sensors, which incorporate sensor and reference dye molecules concentrically within separate layers of a single silica particle (Figure 3.1 a). This concept was initially demonstrated for the quantitative imaging of pH within cells[10]. The reference dye molecules were sequestered within the particle core, while the sensor dyes were covalently integrated into the outer shell of the particle exposing them to analytes in solution. The silica matrix comprising the shell serves as a filter, allowing diffusion of analyte species to and from the sensor dye molecules, while preventing unwanted interactions with proteins or large quenchers that could interfere with fluorescence measurements. One limitation of the Stöber-based synthesis is the limited commercial availability of sensor dyes with conjugation chemistries for integration into the silica matrix. This study describes the development of a seeded reverse microemulsion route to ratiometric pH and $Ca^{+2}$ sensor particles incorporating dextran-bound sensor dyes[12, 25] in the surface shell of the particle. Dextran is a hydrophilic polysaccharide which exhibits good water solubility and low toxicity, while being biologically inert to cleavage by most cellular esterase enzymes due to the uncommon poly-(α-D-1,6-glucose) linkage. Fluorescent dextran conjugates are commercially available and provide an appealing alternative to covalent-conjugation as a method for incorporating

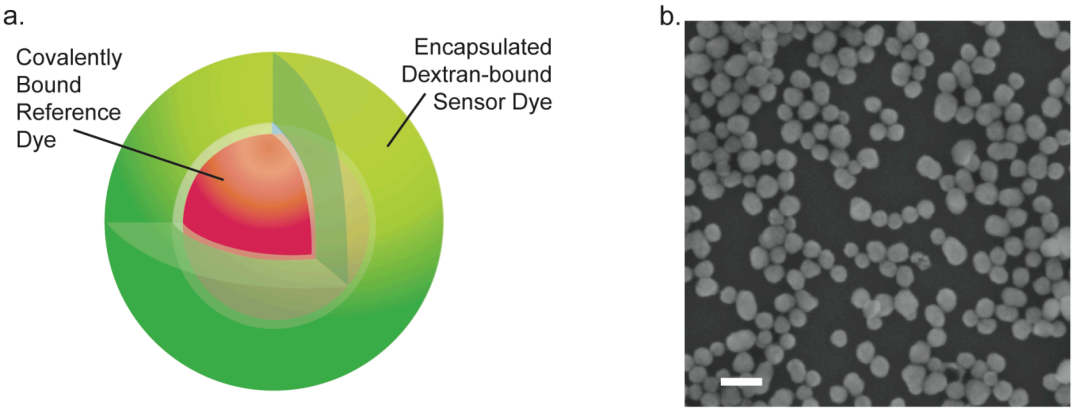


Figure 3.1 (a) A schematic description of the core-shell silica ratiometric sensor nanoparticle design incorporating a protected reference dye in the particle core with sensor dyes in the high-surface area outer shell. (b) Representative SEM image of ~45 nm diameter core-shell silica nanoparticle seeds containing TRITC as a reference dye prior to sensor dye functionalization (scale bar 100 nm).

dyes into a hybrid particle. They have previously been used to nucleate single-emission particles using reverse microemulsions, but their use in ratiometric chemical sensor particles has yet to be investigated[26].

Reverse microemulsions are thermodynamically stable, isotropic dispersions of a hydrophilic (aqueous) phase in a continuous hydrophobic (organic) phase stabilized by an interfacial film of amphiphilic surfactant molecules. These aqueous droplets can serve as reactors concentrating hydrophilic reagents. Reverse microemulsion syntheses of silica nanoparticles have been demonstrated by various groups over the past two decades[26-28] and generally, these syntheses yield highly monodisperse, spherical particles. Following the formation of the emulsion, the three main steps in particle growth are the association of a silica precursor molecule with a reverse microemulsion droplet, interfacial hydrolysis, and base-catalyzed silica condensation within the droplet leading to particle growth[27]. There are several critical parameters which determine the equilibrium size of the reverse microemulsion-derived particles, including the water-to-surfactant molar ratio ($R$) and the cosurfactant-to-surfactant molar ratio ($p$)[29]. In contrast to previous work, we chose to use Stöber-derived seeds for the growth of a functional sensing shell, as opposed to nucleating new particles within the micelles. This allows us to combine the high yield and control of the Stöber synthesis with ability to control the contents of the subsequent shells.

Building on the extensive work of the Tan group and others[26, 29-31], we chose to begin with the Triton X-100/n-hexanol/cyclohexane:aqueous system. In our case, the basic aqueous phase is comprised of the dextran-bound sensor dye, 45 nm diameter Stöber-derived core-shell particles (Figure 3.1 b) and aqueous ammonium hydroxide as a catalyst. Tetraethoxysilane (TEOS) was chosen as the pure silica precursor for these particles and was added to the system following emulsion formation.

### *3.2 Experimental*

Polyethylene glycol *p*-(1,1,3,3-tetramethylbutyl)-phenyl ether (Triton X-100), n-hexanol, cyclohexane, tetraethoxysilane (TEOS), aqueous hydrochloric acid (5.0 N) and ammonium hydroxide (29%) were purchased from Sigma-Aldrich and used as received. 3-aminopropyltriethoxysilane (APTS) was purchased from Gelest, Inc. and used as received. Tetramethylrhodamine isothiocyanate (TRITC), Dextran-bound Calcium Green (10K MW) and Dextran-bound Fluorescein Isothiocyanate were purchased from Molecular Probes (Eugene, OR). 18.2 MΩ Deionized water was obtained from a Millipore Synthesis Purification system.

The reference dye, TRITC (5mg/ml in anhydrous ethanol), was conjugated at a molar ratio of 1:50 to APTS to form a fluorescent silicate precursor molecule under nitrogen atmosphere. This solution was then diluted in ethanol, and aqueous ammonium hydroxide and TEOS were added to yield a final stoichiometry of 15 μM TRITC: 15M ethanol: 300mM $NH_4OH$: 200mM TEOS. The particles were then transferred to aqueous solution by repeated dialysis to deionized water, followed by filtration (0.2μm PTFE) and concentration to 35 mg/ml by rotary evaporation.

The optimized particle synthesis was performed as follows: The emulsion was formed by addition of the particles (63 μl), dextran-bound dye (3 μl at 2.0 mM in $H_2O$), water, acid or salt (17 μl of 0.06M aqueous acid or salt) and ammonia as catalyst (15 μl 28% aqueous solution) to a pre-mixed solution of cyclohexane (1.92 ml), n-hexane (600 μl) and Triton X-100 (0.60 g). This mixture was allowed to equilibrate for 2 hours, after which TEOS (60 μl, depending on *c*) was added to initiate shell growth. The particles were allowed to react under vigorous stirring for 6 hours, at which point the emulsion was broken by addition of ethanol. The precipitate was collected by centrifugation and resuspended by ultrasonication. This washing was

performed thrice, alternating between resuspension in deioinized water and absolute ethanol. The cleaned particles were then analyzed as discussed below.

SEM samples were prepared by dilution of particles in ethanol (5:1000) followed by deposition on cleaned silicon wafer pieces, which were imaged on a LEO 1550 FE-SEM. Particle sizes were calculated based on image analysis of 25 nanoparticles in a representative SEM image. Fluorescence analysis was performed on a PTI fluorometer with all slit widths set to 2 nm. Data analysis was completed with Microsoft Excel 2003 and GraphPad Prism 4.0c.

### *3.3 Results and Discussion*

Among the architectures explored in the literature to date, a number of groups have pursued silica shell growth from heterogeneous nuclei such as quantum dots, metallic or magnetic nanoparticles[32-34], though none were tailored to grow dye-rich, functional shells onto these seeds. We chose to combine the size control and high yield of the Stöber synthesis[8, 23] with the efficient incorporation of microemulsion synthesis to create a core-shell sensor particle. For the seed particles, both homogeneously-dyed and dye-rich core / silica shell C dot particles were investigated, with similar results. To maximize dye density, and simplify the synthetic scheme, the homogeneously-dyed seed particles were chosen for the remainder of the experiments.

Initial syntheses using dextran-bound fluorescein (pH sensor) revealed that the dextran molecules were loosely bound to the seed particles, and were quickly leached upon exposure to water.

To address this, we began by increasing the ratio of silica precursor to seed particles (mol TEOS/mol particles, hereafter known as *c*). The goal was to coat the particles with enough silica to fully entrap the dextran molecules. The dye incorporation was measured by comparing the ratio of fluorescein fluorescence to

rhodamine reference intensity ($F_{max}$) at pH 9.0 (fluorescein pH saturation regime). Understandably, the mean particle diameter increased with $c$, generating particles from 85nm diameter to nearly 150nm diameter from 45 nm diameter cores. Although dye retention increased proportionally with increasing shell thickness (Figure 3.2 a) the issue of dye loss remained. At 150nm diameter ($c$ = 1200), reasonable $F_{max}$ values were achieved, but the particle size is too large for many applications.

The fast dye loss hinted at surface adsorption of some of the dextran molecules rather than the desired physical entrapment within the silica matrix. A closer examination of the interaction between the seed particles and the dextran molecules reveals that both exhibit negative surface charges. The silica particle surface is comprised of siloxane bonds, which exist in equilibrium between protonated and deprotonated silanol groups (Si-OH/Si-$O^-$) while the fluorescein dyes bound to the dextran molecules exist in mono- and di-anion states depending on pH. All told, these negative charges exert a mutual Coulombic repulsion between the two species, which may be responsible for the low incorporation rate. In aqueous solutions, the electrostatic interaction can be controlled by changing the ionic strength of the solution where increased ionic strength acts to "screen" the charges and lower the net repulsion[35].

Towards that end, we chose to increase the ionic strength of the aqueous phase through the addition of salts to the reaction medium. We employed both acid-addition (HCl) and salt-addition (NaCl) to test this hypothesis. An acid-mediated method was previously proposed[31] for the growth of particles nucleated on dextran molecules, though the explanation provided did not address the changes in ionic strength, instead proposing that the acid would protonate the negatively-charged dye moieties. In the ammonium hydroxide-rich reaction solution, the amounts of acid added do not sufficiently change the pH to drop below the dye's pKa and protonate it appreciably.

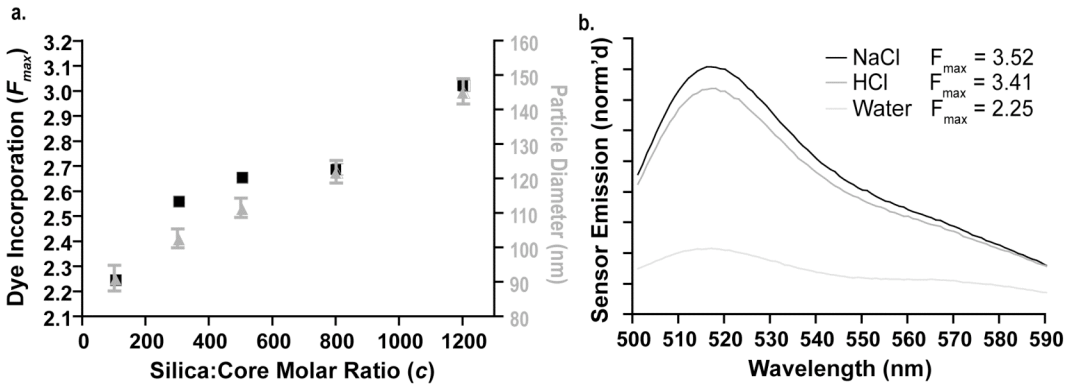


Figure 3.2 (a) A two-axis plot of the effects of increased silica precursor concentration (*c*) on sensor dye incorporation (left axis, black) and particle diameter (right axis, grey) showing the dye loss occurring during the sensor synthesis. (b) A plot of normalized FITC intensity (TRITC dye spectra in Supp. Info.) showing the effects of electrostatic screening on sensor dye incorporation for the addition of 0.06M HCl (dark grey), 0.06M NaCl (black) and water as a control (light grey). Addition of NaCl resulted in the highest encapsulation efficiency and was thus chosen for the remaining syntheses.

The addition of a strong acid such as HCl to the reaction solution would instead likely yield ammonium chloride salts, which could act to screen the particle-dye repulsion.

The addition of both acid (HCl) and salt (NaCl), at 0.06M (with respect to the aqueous phase) yielded an increase in dye incorporation as determined by spectrofluorometry (Figure 3.2b) which compares water-based (light grey), HCl-added (dark grey) and NaCl-added (black) syntheses. Each spectrum is normalized to the emission of the reference dye (TRITCThe increase in fluorescence at 520 nm (FITC) demonstrates the increased incorporation efficiency of the electrostatically-screened syntheses. The NaCl-based syntheses yielded overall slightly higher encapsulation ($F_{max} \sim 3.5$) and were chosen for all further reactions.

The fully optimized synthesis yielded relatively small (83+/-7 nm diameter) dual-emission pH sensitive particles as shown by the representative SEM image in Figure 3.3 a with high dye retention ($F_{max} = 3.5$). The particles were calibrated by spectrofluorometry to determine their pH response in the range from pH 5 to 9 as shown in Figure 3.3 b-d. With increasing pH, the sensor dye intensity (Figure 3.3b) increased six-fold, while the reference intensity (Figure 3.3c) remained constant. The pH response of the sensor particles can be calculated based on a modified Henderson-Hasselbalch equation which relates the individual intensity ratios ($I_{FITC}/I_{TRITC} = F_i$) to the concentration of mono- and di-anionic fluorescein species through the extrema values ($F_{max}$ and $F_{min}$) as shown in Equations 3.1-3.2.

$$\mathrm{pH} = -\log a_{H^+} = pK_a + \log\left(\frac{[Base]}{[Acid]}\right) \qquad \text{Eq. 3.1}$$

$$pH = pK_a + \log\left(\frac{F_i - F_{\min}}{F_{\max} - F_i}\right) \qquad \text{Eq. 3.2}$$

This analysis was applied to the data in Figure 3.3b-c as shown in Figure 3.3d, which reveals the $pK_a$ of the sensor to be approximately 6.3, which agrees well with

literature values for fluorescein (6.3-6.4)[12], showing that the incorporation into the silica matrix has negligible effects on FITC's utility in ratiometric pH sensing.
To demonstrate the versatility of this synthetic method for other sensor dyes which are unavailable with covalent conjugation chemistries, we developed a ratiometric $Ca^{+2}$ ion sensor by incorporating Calcium Green (Molecular Probes, Eugene, OR). Calcium Green (CG) is based on a dichlorofluorescein fluorophore conjugated to a BAPTA chelator (1,2-*bis*(*o*-aminophenoxy) ethane-N,N,N',N'-tetraacetic acid) which exhibits excellent specificity for $Ca^{+2}$, with a binding constant of approximately 0.2-0.4 μM depending on its surroundings[36, 37]. In the unbound state, the chelator can donate an electron into the ground state of the dichlorofluorescein, effectively quenching fluoresecence, while the $Ca^{+2}$-bound molecule cannot, thereby reversibly increasing fluorescence with increasing calcium concentration. Currently, this dye is not commercially available with a silica-compatible conjugation chemistry, but it is available as a dextran-conjugate from Invitrogen.

We applied the same synthetic conditions developed for 10K MW dextran-fluorescein to grow core-shell silica nanoparticles incorporating Calcium Green into the external shell of a TRITC-core based nanoparticle. The results of this synthesis are shown by a representative SEM image in Figure 3.4 a, where 103+/-8 nm core-shell particles were formed. The $Ca^{+2}$-dependent fluorescent response of the particles was determined using a commercially-available calibration buffer kit (Molecular Probes C-3008). The sensor and reference dyes were analyzed separately by spectrofluorometry (Figure 3.4 b-c) showing the stable reference fluorescence of the core- dye TRITC along with the dynamic range of the CG dye in response to changing [$Ca^{+2}$]. The ratio of peak CG fluorescence to peak TRITC fluorescence ($F_i$) at each concentration was determined over a range from 0 to 39μM $Ca^{+2}$. These values were

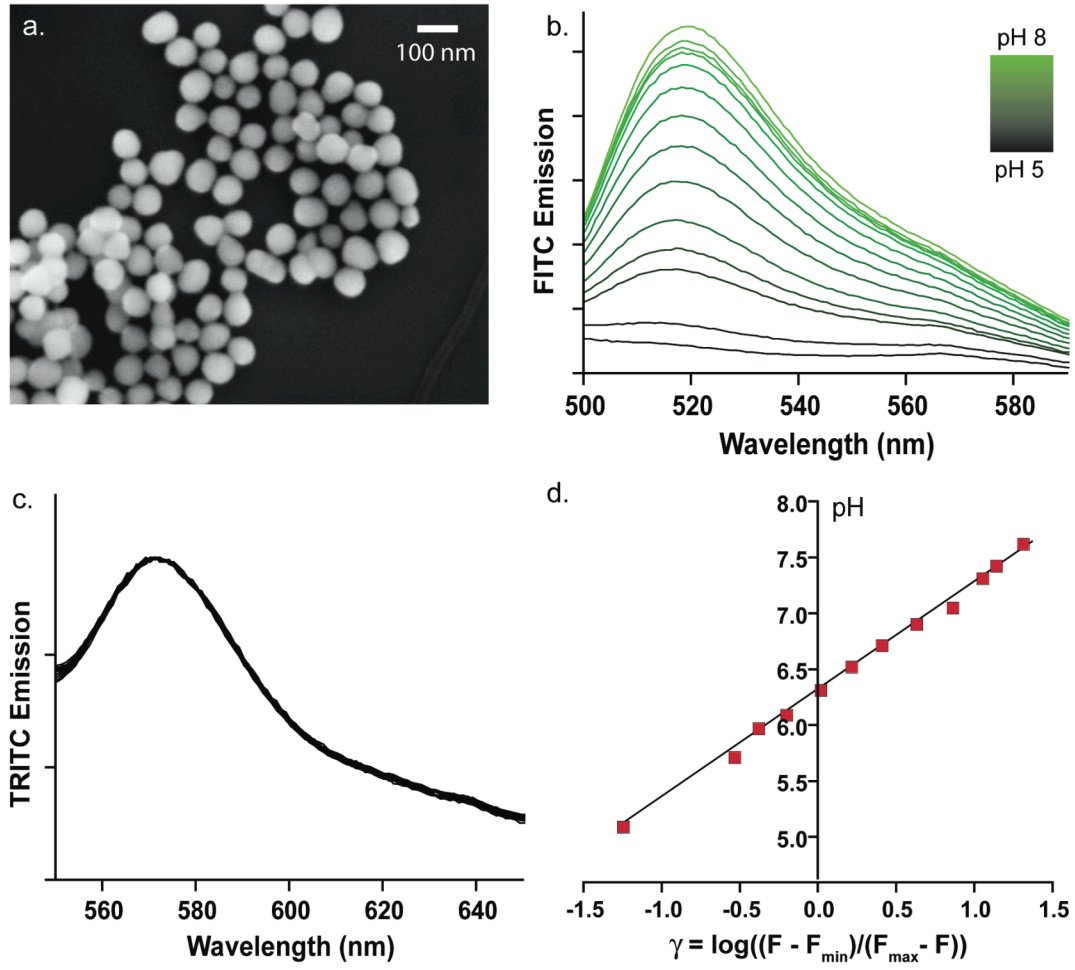


Figure 3.3 (a) Representative SEM image of core-shell silica nanoparticle pH sensors with diameters of 83 +/- 7 nm. (b) Emission spectra of fluorescein sensor dye ($\lambda_{ex}$ = 488 nm) for pH values from 5.0 (black) to 8.0 (light green), normalized to the peak emission of (c) tetramethylrhodamine reference spectra. (d) A Hendersen-Hasselbalch plot of $\gamma$ versus pH used to determine a calibration curve for the sensors as well as the pKa of the sensor.

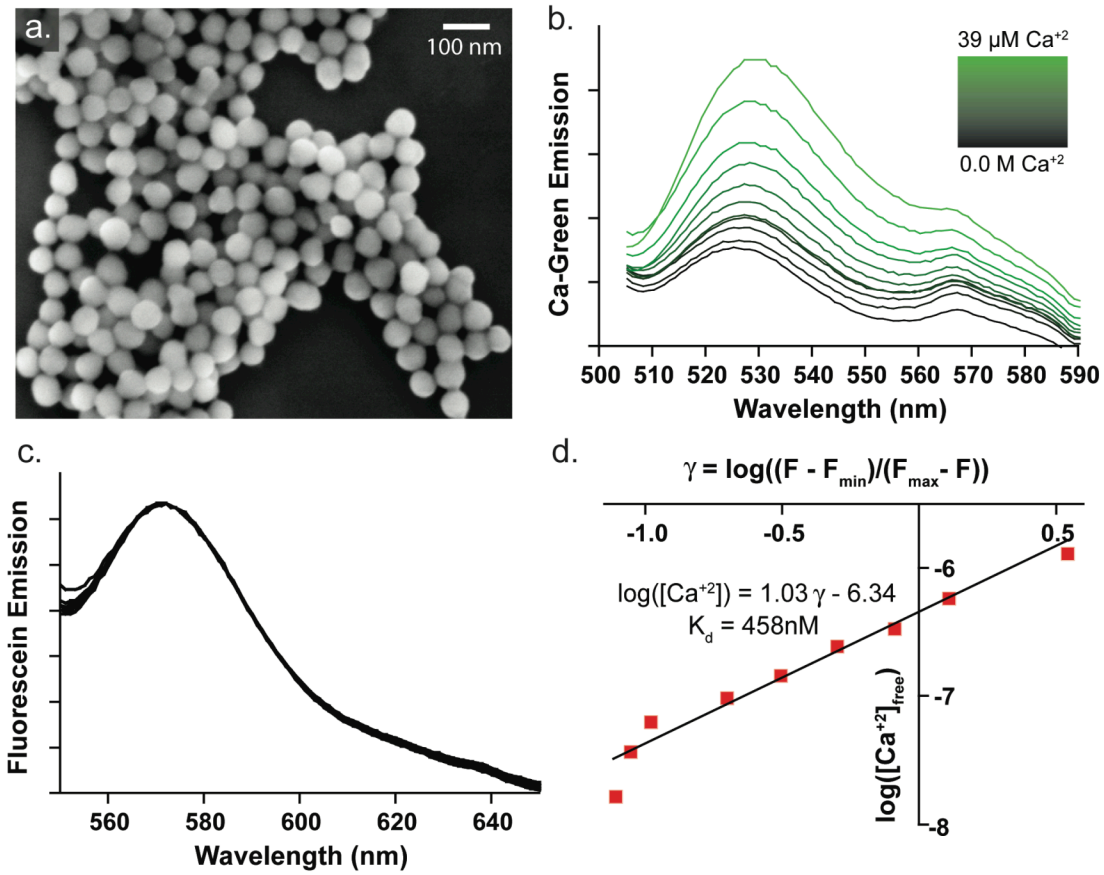


Figure 3.4 (a) Representative SEM image of core-shell silica nanoparticle pH sensors with diameters of 103 +/- 8 nm. (b) Emission spectra of Calcium Green sensor dye ($\lambda_{ex}$ = 488 nm) for [$Ca^{+2}$] values from 0.0M (black) to 39.0μM (light green), normalized to the peak of tetramethylrhodamine reference emission spectra shown in (c). (d) A plot of γ versus log([$Ca^{+2}$]) used to determine a calibration curve for the sensors as well as the $K_d$ of the sensor.

analyzed using Equation 3.3, where $F_{max}$ and $F_{min}$ are the saturation and zero $Ca^{+2}$ values of $F_i$, respectively. This analysis (Figure 3.4 c) showed the effective binding constant of this sensor to be 302 nM $Ca^{+2}$. While this $K_d$ is below the literature value for free Calcium Green ($K_d \sim 500$ nM)[12], it remains within the physiologically relevant regime for many $Ca^{+2}$-related phenomena and is consistent with $K_d$ values for sterically constrained $Ca^{+2}$ sensors[37].

$$\log\left(\left[Ca^{+2}\right]_{free}\right) = \log\left(K_d\right) + \log\left(\frac{[bound]}{[unbound]}\right) = \log\left(K_d\right) + \log\left(\frac{F_i - F_{\min}}{F_{\max} - F_i}\right) \qquad \text{Eq. 3.3}$$

### *3.4 Conclusions*

An alternative method for the development of ratiometric sensor nanoparticles is presented to address the incorporation of dye molecules which otherwise cannot be covalently incorporated into the silica network. A seeded reverse microemulsion was used to enhance the incorporation of dextran-conjugated sensor dye molecules into the shell of a core-shell silica nanoparticle sensor. Sensor dye incorporation was quantified via spectrofluorometry and found to be dramatically enhanced by decreasing the electrostatic repulsion between the negatively-charged dextran-dye conjugates and the silica nanoparticle seeds. Increasing the ionic strength of the aqueous phase during synthesis by salt addition screened the electrostatic repulsion and enhanced the physical entrapment of the dye in the silica shells. Ultimately, 80-100nm diameter particles were synthesized with biologically-relevant sensitivities for both pH and free $Ca^{+2}$ based on 10K MW dextran conjugates of fluorescein and Calcium Green.

REFERENCES


[1] F. Wang, W. B. Tan, Y. Zhang, X. Fan, and M. Wang, *Nanotechnology*, 2006, **17**, R1.

[2] A. Burns, H. Ow, and U. Wiesner, *Chemical Society Reviews*, 2006, **35**, 1028.

[3] J. B. Pawley, '*Handbook of biological confocal microscopy*', Plenum Press, 1995.

[4] E. Betzig, G. H. Patterson, R. Sougrat, O. W. Lindwasser, S. Olenych, J. S. Bonifacino, M. W. Davidson, J. Lippincott-Schwartz, and H. F. Hess, *Science*, 2006, **313**, 1642.

[5] M. J. Rust, M. Bates, and X. Zhuang, *Nat Meth*, 2006, **3**, 793.

[6] B. Valeur, 'Molecular Fluorescence: Principles and Applications', Wiley-VCH, 2002.

[7] X. Michalet, F. F. Pinaud, L. A. Bentolila, J. M. Tsay, S. Doose, J. J. Li, G. Sundaresan, A. M. Wu, S. S. Gambhir, and S. Weiss, *Science*, 2005, **307**, 538.

[8] H. Ow, D. R. Larson, M. Srivastava, B. A. Baird, W. Webb, and U. Wiesner, *Nano Letters*, 2005, **5**, 113.

[9] M. Qhobosheane, S. Santra, P. Zhang, and W. Tan, *The Analyst*, 2001, **126**, 1274.

[10] A. Burns, P. Sengupta, T. Zedayko, B. Baird, and U. Wiesner, *Small*, 2006, **2**, 723.

[11] H. A. Clark, M. Hoyer, M. A. Philbert, and R. Kopelman, *Anal. Chem.*, 1999, **71**, 4831.

[12] R. P. Haugland, 'The Handbook - A guide to Fluorescent Probes and Labeling Technologies', Invitrogen, Inc, 2005.

[13] R. Tsien, *Ann. Rev. Biochem*, 1998, **67**, 509.

[14] J. Choi, A. Burns, R. Williams, Z. Zhou, A. Flesken-Nikitin, W. Zipfel, U. Wiesner, and A. Nikitin, *Journal of Biomedical Optics*, 2007, **12**, 064007 (1.

[15] D. Larson, H. Ow, H. Vishwasrao, A. Heikal, U. Wiesner, and W. Webb, *Chemistry of Materials*, 2008, **20**, 2677.

[16] B. L. F. C. J. P. B. C. Sanchez, *Advanced Materials*, 2003, **15**, 1969.

[17] F. Wang, W. Tan, Y. Zhang, X. Fan, and M. Wang, *Nanotechnology*, 2006, **17**, R1.

[18] J. R. Lakowicz, 'Principles of Fluorescence Spectroscopy', Springer-Verlag, 2006.

[19] Z. Gryczynski, I. Gryczynski, and J. R. Kalowicz, *Methods in Enzymology*, 2003, **360**, 44.

[20] J. W. Aylott, *The Analyst*, 2003, **128**, 309.

[21] H. Xu, J. W. Aylott, R. Kopelman, T. J. Miller, and M. A. Philbert, *Anal. Chem.*, 2001, **73**, 4124.

[22] E. Herz, H. Ow, D. Bonner, A. Burns, and U. Wiesner, *J. Am. Chem. Soc.*, 2008, **submitted**.

[23] W. Stober, A. Fink, and E. Bohn, *Journal of Colloid and Interface Science*, 1968, **26**, 62.

[24] C. J. Brinker and G. W. Scherer, 'Sol-Gel Science: The Physics and Chemistry of Sol-Gel Processing', Harcourt Brace Jovanovich, 1990.

[25] J. Iain, *The Histochemical Journal*, 1998, **30**, 123.

[26] X. Zhao, R. Bagwe, and W. Tan, *Advanced Materials*, 2004, **16**, 173.

[27] F. J. Arriagada and K. Osseo-Asare, *Journal of Colloid and Interface Science*, 1999, **211**, 210.

[28] C. L. Chang and H. S. Fogler, *Langmuir*, 1997, **13**, 3295.

[29] R. P. Bagwe, C. Yang, L. R. Hilliard, and W. Tan, *Langmuir*, 2004, **20**, 8336.

[30] R. P. Bagwe, L. R. Hilliard, and W. Tan, *Langmuir*, 2006, **22**, 4357.

[31] X. He, K. Wang, W. Tan, J. Chen, J. Duan, Y. Yuan, and X. Lin, *Chinese Science Bulletin*, 2005, **50**, 2821.

[32] J. Kim, J. E. Lee, J. Lee, J. H. Yu, B. C. Kim, K. An, Y. Hwang, C. H. Shin, J. G. Park, J. Kim, and T. Hyeon, *J. Am. Chem. Soc.*, 2006, **128**, 688.

[33] L. J. C. M. R. P. C. Y. C. K.-J. Lin, *Advanced Materials*, 2004, **16**, 1845.

[34] W. Zhao, J. Gu, L. Zhang, H. Chen, and J. Shi, *J. Am. Chem. Soc.*, 2005, **127**, 8916.

[35] G. Parfitt, 'Dispersion of Powders in Liquids', Applied Science, 1981.

[36] R. Pethig, M. Kuhn, R. Payne, E. Adler, T. Chen, and L. Jaffe, *Cell Calcium*, 1989, **10**, 491.

[37] C. M. Loughrey, K. E. MacEachern, J. Cooper, and G. L. Smith, *Cell Calcium*, 2003, **34**, 1.

# CHAPTER 4

# FUNCTIONAL TOMOGRAPHIC FLUORESCENCE IMAGING OF pH MICROENVIRONMENTS IN MICROBIAL BIOFILMS WITH SILICA NANOPARTICLE SENSORS[*]


## *4.0 Abstract*

Attached bacterial communities often generate three-dimensional (3D) physicochemical gradients that create microenvironments where local conditions differ substantially from the surrounding solution. Given the ubiquity of biofilms in nature, and their impacts on issues ranging from water quality to human health, better tools for understanding of these microenvironments are needed. In this study, we employ fluorescent core-shell silica nanoparticle sensors (C dot sensors) to non-disruptively measure local pH within *Escherichia coli* PHL628 and mixed-culture biofilms. Testing 70, 30 and 10 nm diameter sensor particles revealed a critical size for homogeneous biofilm staining with only the 10 nm diameter particles capable of successful quantitative functional imaging. Tomographic fluorescence imaging via confocal microscopy generated high-resolution maps of biofilm pH ranging from pH 5 to above 7, and distinct local heterogeneities. Time-resolved measurements of the effects of glucose addition on local pH of both suspended and attached cultures showed a general acidification of the environments, likely due to the release of TCA-cycle-acids and $CO_2$ by glycolysis. These studies demonstrate that the combination of 3D functional fluorescence imaging with well-designed nanoparticle sensors provides a powerful tool for *in situ* characterization of chemical microenvironments in complex biofilms.


[*] Prepared for submission as: Gabriela Hidalgo[†], Andrew Burns[†], Anthony Hay, Paul L. Houston, Ulrich Wiesner, Leonard W. Lion. "Functional Tomographic Fluorescence Imaging of pH Microenvironments in Microbial Biofilms with Silica Nanoparticle Sensors." ([†]equal co-authorship)

### *4.1 Introduction*

Biofilms are collections of surface-attached microbes entrapped in a self-produced matrix of extracellular polymeric substances anchored to a surface[1]. Their growth is characterized by complex three-dimensional structures including channels, voids, towers and mushroom-like protrusions[2]. They are common both in biological systems as well as in near-surface fluid rock systems and may represent a significant portion of the surface area exposed to fluids in many natural environments[3]. The ubiquity of biofilms has a variety of important implications for modern society. Industrially, biofilms are used in a wide array of engineered systems including treatment of wastewater and hazardous waste and remediation of contaminated soil and oil spills[4], but they can also contaminate water distribution systems, foul the hulls of ships and promote corrosion. Medically, biofilms have been implicated infections in lungs and chronic wounds, as well as dental caries and periodontal diseases.

One characteristic feature of biofilms is the development of three-dimensional chemical gradients, from the diffusion of nutrients, metabolic products, and signaling compounds throughout the film. These gradients create microenvironments in which the local physicochemical properties may differ substantially from those in the surrounding solution[5]. This gradation of conditions allows, for example, anaerobic bacteria to flourish within biofilms that are growing in an otherwise aerobic environment[6]. An example of the steep gradients that can develop within a biofilm are caries caused by dental plaque. Following sugar consumption, the pH within the plaque biofilm drops dramatically (<5.5) while the pH of the overlying saliva remains near neutral. This acidification leads to demineralization of the tooth enamel and ultimately caries[6-8].

The spatial variation of pH within microbial biofilms is an exciting area of research that may elucidate a variety of topics. From a clinical standpoint, pH

heterogeneities are of relevance as a gauge of biofilm development in wound management. The degree of physiological heterogeneity, marked by the establishment of nutrient, dissolved gas and pH gradients, increases with time and is positively correlated with the development of drug resistance. Furthermore, it has been well established that the susceptibilities of bacterial cells towards antibiotics and biocides are profoundly affected by their pH[9]. The recent emergence of antibiotic-resistant pathogenic bacteria makes this a topic of great interest[1, 10-12].

One of the common techniques for interrogating the local chemistry of biofilms, is microelectrochemistry, but microelectrode measurements lack spatial resolution[13] and the ability to generate three-dimensional images to visualize heterogeneities. An alternative, minimally invasive method is based on fluorescence microscopy of ratiometric sensor dyes such as seminapthorhodafluor (SNARF). In this case, the spatial resolution is limited only by that of the microscope in use and multi-dimensional imaging is possible, but sensor dyes have been demonstrated to interact with biofilm components, altering their sensitivities and perturbing the resulting images[14]. Further, dye penetration into the biofilm can also be limited by restricted diffusion into microcolonies[6]. Finally, like all free dye molecules, the dyes used for biofilm analysis are limited in brightness, prone to photobleaching over long or repeated exposures and may cause cellular toxicity[15].

We used a combination of functional three-dimensional (tomographic) fluorescence imaging with ratiometric silica nanoparticle sensors to study the morphology and temporal evolution of pH microenvironments in pure *Escherichia coli* (*E. coli* PHL628) and mixed-culture wastewater biofilms. Because of the diversity of structure, tomographic imaging is of particular interest to investigate biofilms in their native state. Optical coherence tomography[16], soft X-ray microscopy[17] and confocal fluorescence microscopy[16, 18] in particular enable high-

resolution structural reconstructions with minimal perturbation to the biofilm. In order to overcome the limitations of free ratiometric sensor dyes, we employed ratiometric core-shell silica nanoparticle sensors, referred to as C Dot sensors[19]. Placing a pH sensitive dye in a thin silica shell surrounding a reference dye-rich core[19] as shown schematically in Figure 4.1a permits intensity-based quantification of the local pH by comparison of sensor and reference dye emission intensities (Figure 4.1b), effectively separating sensor concentration fluctuations from analyte effects[20-22]. The covalent incorporation of dyes into a core-shell silica matrix significantly enhances both dye brightness and photostability through changes in the radiative and non-radiative fluorescence rates[23]. Finally, silica is a highly biocompatible and easily functionalized material for diverse biological applications[15, 24].

To assess the possibility of time-resolved pH imaging, aliquots of glucose were added to biofilm samples to promote acid production by glycolysis. To the best of our knowledge, this is the first time that ratiometric nanoparticle sensors have been used for functional volumetric imaging of analytes in prokaryotic systems.

## *4.2 Results*

### *4.2.1 C dot sensor distribution and toxicity*

We assayed biofilms with C dot sensors of varying diameters: 70, 30 and 10 nm (Figure 4.1c-e, respectively) and both positively charged (aminated) and negatively charged (bare silica) surfaces. The amination process screened the local pH effects on the particle making quantitation difficult and thus was not pursued further. For 70 and 30 nm diameter bare silica sensors, the particles were found to distribute sparsely and heterogeneously in the biofilms. Only when using the smallest, 10 nm diameter bare C dots sensors were we able to reproducibly achieve high and homogeneous biofilm

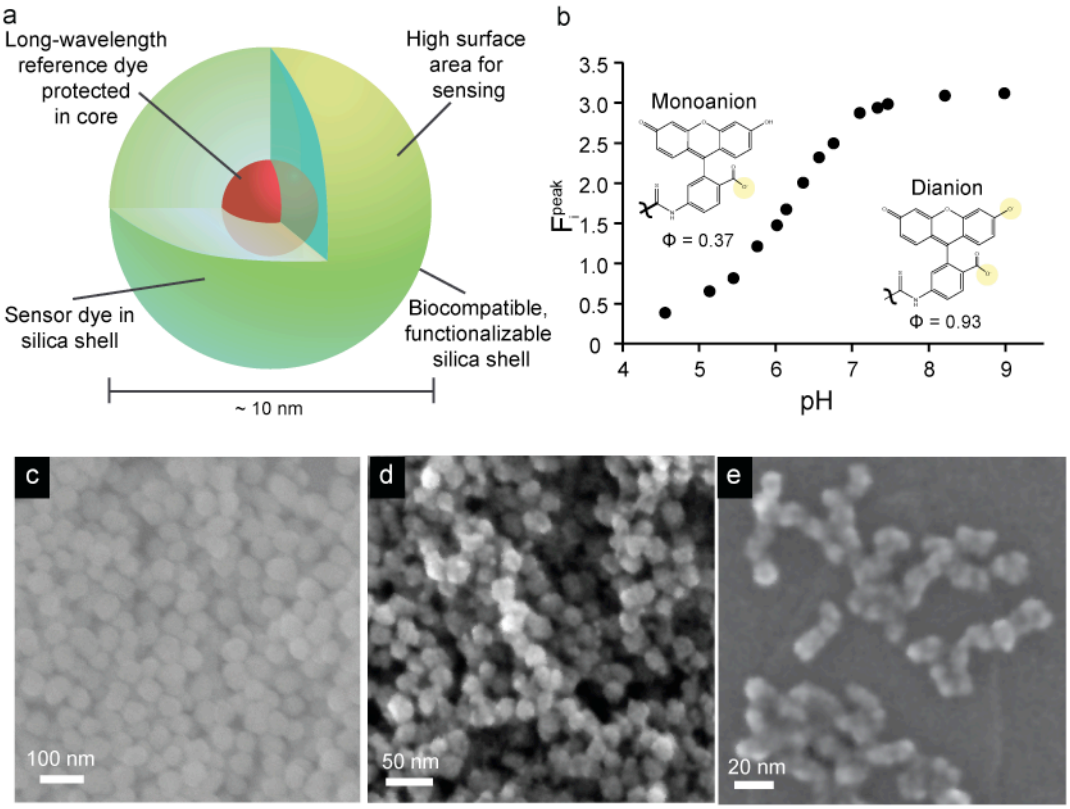


Figure 4.1 a, Schematic diagram showing the core/shell architecture of the C dot sensors that highlights the reference dye (Cy5) sequestered in the core and coated by a sensor dye shell (fluorescein). b, Peak fluorescein emission collected for solutions of known pH value from 4.5 to 9.0. The figure also shows the molecular structure of the dye in its di-anionic charge state where it exhibits a quantum yield of ~93% and in its monoanionic state where its quantum yield is of ~37%. c-e, SEM images of 70, 30 and 10 nm diameter sensor particles

incorporation. All experiments described in the following were performed with the bare 10 nm particles.

The growth curves presented in Figure 4.2a reveal that the bacterial growth is not affected by the introduction of 10 nm C dot sensor particles or dye-free silica nanoparticles of similar size. The OD reached after 18 hours of growth was, on average, 0.33 for *E. coli* and 0.46 for wastewater samples, with minimal effect of particle type (Figure 4.2a) or concentration (Appendix B, Figure B.1). The OD of sterile controls remained constant at approximately 0.0 OD.

### 4.2.2 pH measurement in suspended cultures

The pH profiles after glucose addition to *E. coli* PHL628 cultures and to mixed community wastewater cultures are shown in Figure 4.2b-c and 4.2d-e, respectively. The pH was tracked both with C dots (Figure 4.2b, d) and with a pH meter (Figure 4.2c, e). For these samples, the trends in pH as measured over time using C dot sensors and a pH meter were similar. The differences in values may be caused by the nature of the measurement being performed: if the C dot sensors are adsorbed to cells in suspension, the pH of the area immediately surrounding that cell is being measured; while the pH meter records the pH of the bulk solution. These results validate our claim that C dots may be used for real time tracking of pH in bacterial environments.

Figures 4.2b and c show that the pH of a suspended *E. coli* PHL628 culture after glucose addition dropped from 7.0 to near 5.5, over ~400 minutes post-addition. Over the course of the experiment, the pH did not return to neutral values. This decrease in pH can be explained by the release of $CO_2$ and degradation products such as citric and succinic acid from the catabolism of glucose through the citric acid cycle in the bacteria. We do not believe this acidification to be the result of fermentation,

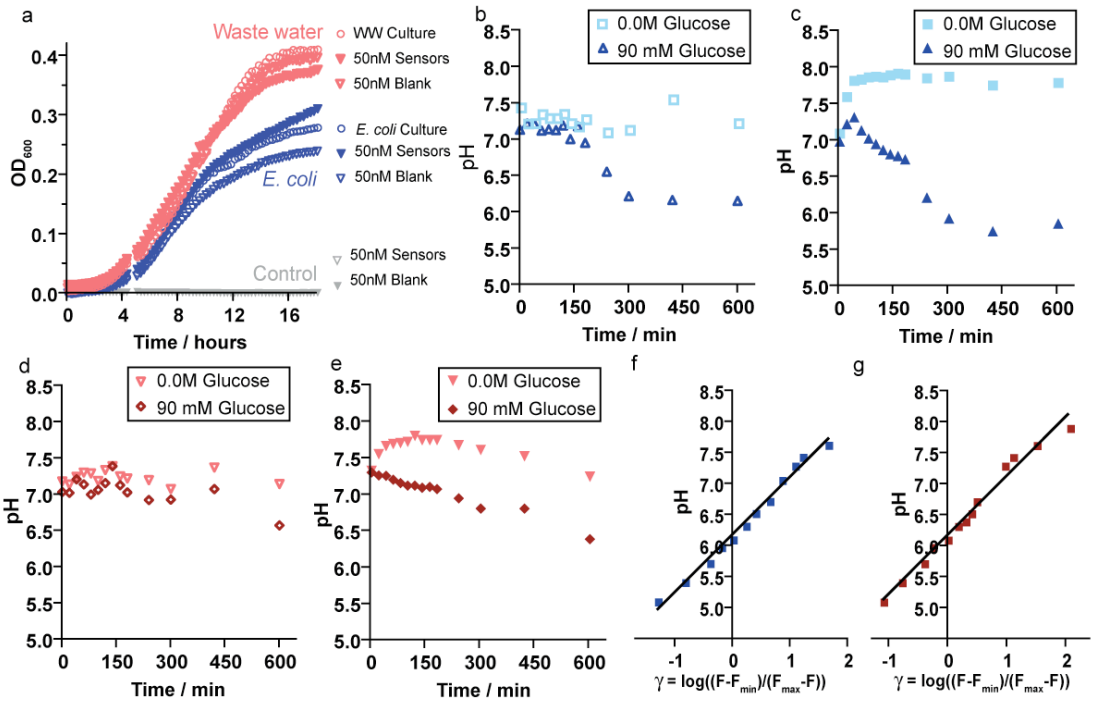


Figure 4.2 - a, OD at 600 nm for *E. coli* PHL628 (top curves, shown in red), mixed wastewater culture (middle curves, shown in blue) and sterile controls (along x-axis, black) versus time, under normal growth conditions (○), and in the presence of 50 nM C dot sensors (▼) or 50 nM pure silica nanoparticles of the same size (▽). b-e, pH versus time after glucose introduction as measured by silica nanoparticle sensors (b,c) and pH meter (d,e) in planktonic *E. coli* (b,d) and wastewater culture (c,e) suspensions. Triangle and square symbols indicate glucose additions of 90 or 0 mM respectively. f-g) pH calibration graphs for *E. coli* biofilm imaging f, ($R^2 = 0.99$) and wastewater mixed-culture biofilm imaging g, ($R^2 = 0.99$) based on pixel-wise image analysis of calibration confocal microscopy images.

because the cultures were stirred continuously, to maintain aerobic conditions. The drop in pH begins approximately 40 minutes after glucose addition, prior to which, the pH increased to nearly 7.3. The glucose-free sample displayed a similar increase in pH from neutral to about 7.7 during the first 60 minutes followed by a plateau.

As shown in Figures 4.2d and e, the pH in the 90 mM glucose-exposed mixed-culture dropped by only ~0.8 pH units over the course of the experiment. This difference relative to the behavior of *E. coli* is reasonable given that glucose is the primary energy source for enteric *E. coli,* which constitutively expresses the necessary enzymes for glucose metabolism. Therefore in *E. coli*, catabolism can begin immediately upon glucose exposure leading to a pH drop as metabolites accumulate in solution. The mixed wastewater culture, however, includes a large variety of microorganisms that may not be adapted to glucose consumption or that must go through an induction process to metabolize glucose, resulting in a lag in the pH drop.

Both the mixed-culture and *E. coli* control samples exhibited an initial increase in pH. It has been shown that alkalinization follows amino acid catabolism as a result of the excretion of excess ammonium[25], therefore, we believe that the increase in pH observed in the cultures to which no glucose was added is likely the result of the consumption of the abundant oligopeptides that are present in LB broth and are the principal source of carbon in this growth medium.

### *4.2.3 Functional Three-dimensional Tomographic Imaging*

In Figure 4.2f and g we show the image-based pH calibration graphs for the (f) *E. coli* biofilm ($R^2 = 0.99$) and (g) wastewater biofilm ($R^2 = 0.99$) image settings as calculated by a modified Henderson-Hasselbalch equation (Eq. 4.1) where $F_i = I_{FITC} / I_{Cy5}$, and $F_{min}$ and $F_{max}$ are the extreme values of $F_i$ at low and high pH, respectively. All *F*-values were calculated by pixel-wise analysis of confocal microscopy images of

C dot sensors suspended in calibration buffers of varying pH as described in the methods section. Based on these calibration curves, we were able to accurately determine pH from 5.0 to 8.0, which includes the physiological range of this system.

$$pH = pK_a + \log\left(\frac{F_i - F_{\min}}{F_{\max} - F_i}\right) \qquad \text{Eq. 4.1}$$

Figures 4.3a and b show, respectively, the green (sensor dye) channel and the red (reference dye) channel confocal images of a typical live, hydrated *E. coli* PHL628 biofilm at a focal plane approximately 90 μm from the attachment substrate. Figure 4.3c depicts the sensor and reference images merged with a brightfield image of the biofilm, demonstrating the incorporation of the particles within the film. The greater depth of field of the brightfield image shows the structure of the film above and below the confocal image plane, which accounts for the apparent mismatch of the fluorescence and brightfield images. Vertical scanning of the sample results in registry of particle fluorescence with the brightfield images of the biofilm over the z-range of imaging (top view, Figure 4.3 e).

The pH was analyzed ratiometrically based on the sensor and reference images and is expressed as a false spectrum (red-yellow) in Figure 4.3d overlaid on the brightfield image. The pH scale is shown on the right of the image. Specifically, the pH within the core of the biofilm is low (red) and increases (orange/yellow) towards the periphery of the film, potentially due to low diffusion rates of acidic metabolites back into solution. This region of the biofilm was imaged from the attachment substrate up to 160 μm in 1 μm steps, and volumetrically reconstructed to show the biofilm morphology as well as the pH gradients and microenvironments in the x,y and z directions. Top- and side- views are presented in Figures 4.3e and f, respectively. The vertical gradient from low pH deep in the film to more neutral pH at the upper

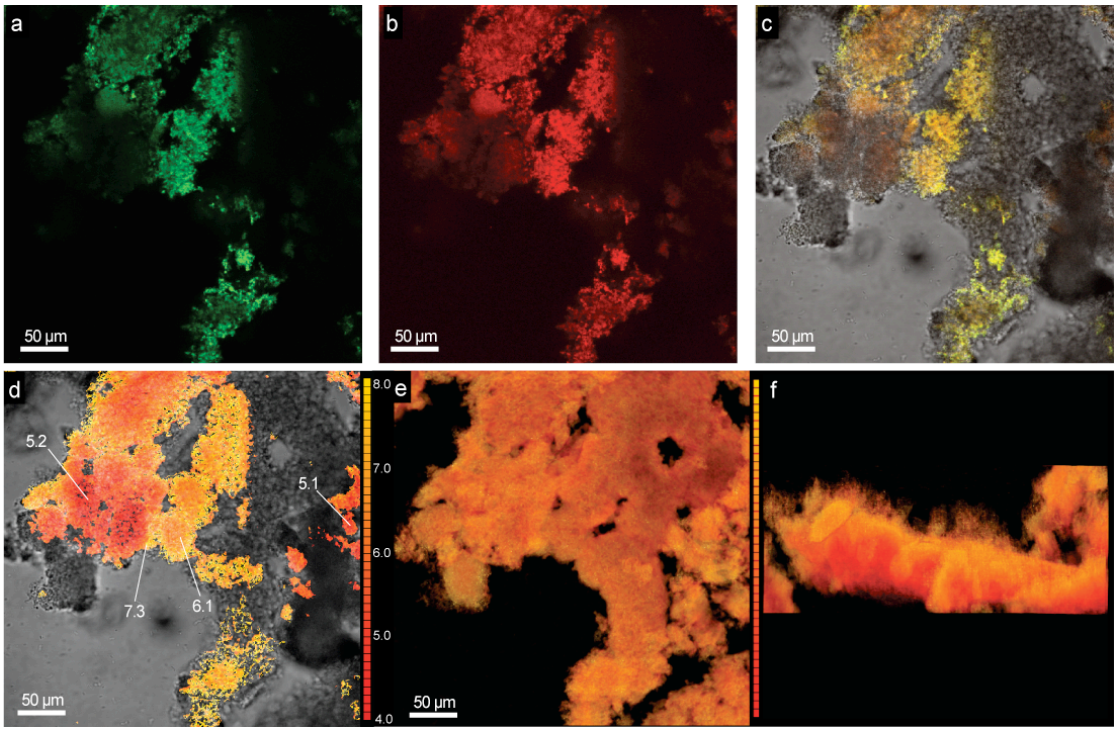


Figure 4.3 - a, Green and b, red channel confocal images of a typical live, hydrated *E. coli* PHL628 biofilm at a focal plane approximately 90 µm from the substratum. c, shows the sensor and reference images superimposed on a brightfield image of the biofilm, showing the co-localization of the particles in the film. The pH was analyzed ratiometrically based on the sensor and reference images and is expressed as a false spectrum (red-yellow) in d, overlaid on the brightfield image, with the pH scale shown at the right in the image. e, Top-down and f, side-view of the reconstructed biofilm pH map show the local variation of pH from the neutral outside surface of the film to the acidic core.

surface observed in the side-view (Figure 4.3f) correlates well with the in-plane gradients seen in Figure 4.3d. A 'fly-through' movie of the full tomographic reconstruction can be found in the Supplemental Information (Video 1).

Similarly, Figures 4.4a-d depict the sensor, reference, overlay and ratiometric pH images of a mixed-culture biofilm imaged approximately 77 μm from the attachment substrate. The pH is more dramatically heterogeneous throughout this mixed-culture than in the axenic one, both horizontally as well as vertically as revealed by a comparison of top- and side-views in Figures 4.3e and f with 4.4e and f. Figures 4.4g-i show the distinct pH microenvironments in the three-dimensional pH image of the mixed culture film by presenting three projections of the full tomographic reconstruction (500x500x160μm). For the corresponding fly-through video (Video 2) please see the Supplementary Information. Based on the morphological and chemical differences between these microenvironments, it is likely that bacteria from different phyla are coexisting and generating different metabolic by-products.

Investigating specific regions of interest by zooming into the full tomographic reconstructions and providing various views of the *E. coli* and mixed-culture biofilms (Figure 4.5) demonstrates the power of nanoparticle sensor-enabled 3D functional imaging. Figures 4.5 a-d show in detail the low-to-neutral pH gradient formed from the core of the biofilm to the periphery, as well as the fine structure with channels and voids of the *E. coli* film. Figures 4.5 e-h show the voids formed by the interpenetration of the low pH film components and the fibrous neutral regions as well as the different growth habits of the two including a mushroom-like protrusion.

Figure 4.6a depicts the average pH versus time following a glucose injection (90mM) for *E. coli* PHL628 (red) and wastewater mixed culture (blue) biofilms. Figures 4.6b and 4.6c show the corresponding confocal ratiometric pH images at t = 0

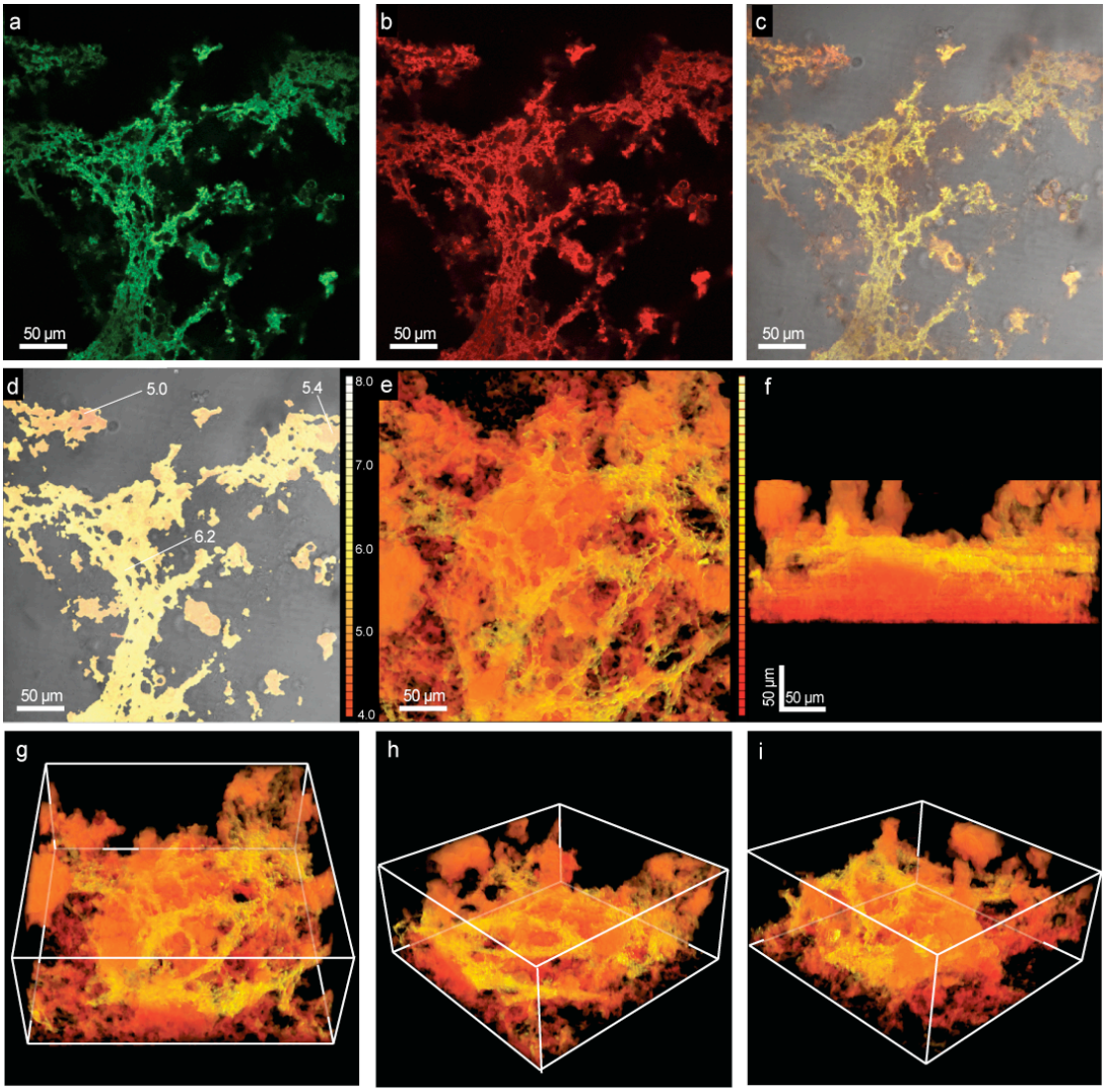


Figure 4.4 - a, Green and b, red channel confocal images of a typical live, hydrated wastewater mixed-culture biofilm at a focal plane approximately 77 µm from the substratum. The sensor and reference images are superimposed on a brightfield image of the biofilm c, showing the co-localization of the particles in the film. The pH was analyzed ratiometrically based on the sensor and reference images and is expressed as a false spectrum (red-yellow) in d, and overlaid on the brightfield image, with the pH scale shown at the right in the image. Top-down e, side-view f, (and appropriate pH scale bar from pH 4 to 8) and off-axis g-i, views of the fully reconstructed biofilm pH map (500x500x160µm) showing the considerable heterogeneity that exists within the mixed-culture film, where a web-like neutral environment exists with acidic film with tower structures surrounding and penetrating it.

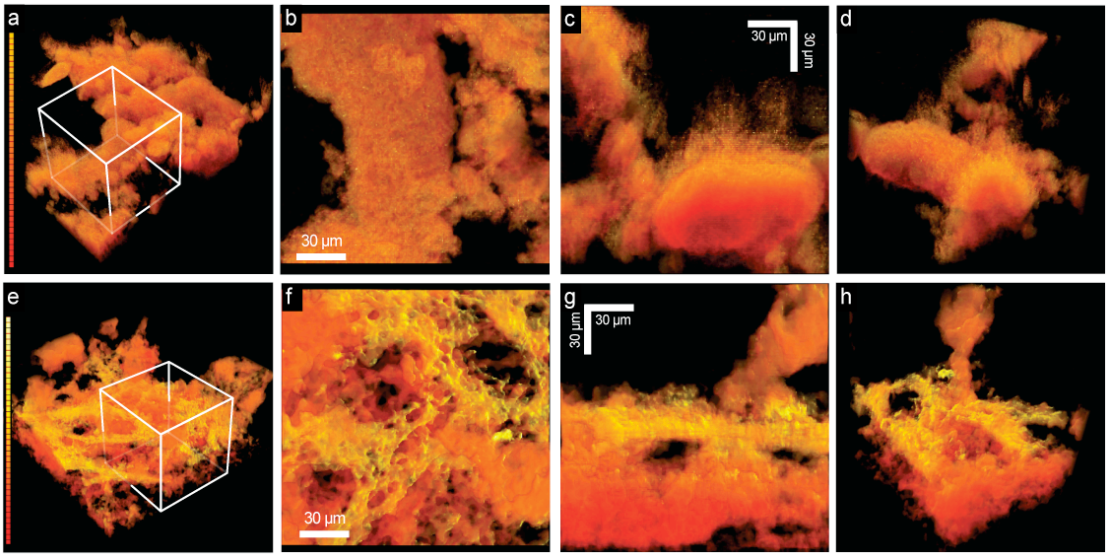


Figure 4.5 - a, an off-axis view of the reconstructed *E. coli* PHL628 biofilm with a region of interest defined by the white cube (160 x 160 x 160 µm) and pH map scale at left (pH 4.0-8.0, red-yellow). b-d, top-, side- and off-axis views of the region of interest showing the pH heterogeneities, as well as the local structure of the biofilm. e, An off-axis view of the reconstructed wastewater mixed-culture biofilm with a region of interest defined by the white cube (160 x 160 x 160 µm) and pH map scale at left (pH 4.0-8.0, red-yellow). f-h, top-, side- and off-axis views of the region of interest showing the pH heterogeneities, as well as the local structure of the biofilm including voids, channels and a tower.

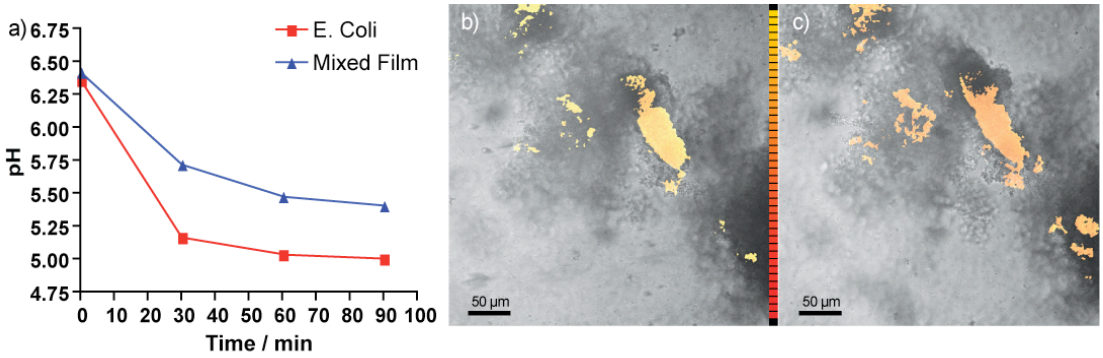


Figure 4.6 - a, average pH versus time post injection of 90 mM glucose to biofilms to *E. coli* PHL628 (in red) and mixed wastewater culture (in blue). b, Imaging of C dots within an *E. coli* PHL628 biofilm corresponding to the initial b, and final c, times of a, (Color scale corresponds to pH values from 4 to 8)

and 90 minutes, respectively, after the glucose addition to the *E. coli* PHL628 biofilm at a focal plane approximately 60 μm from the attachment substrate (further images available in Appendix B). The *E. coli* biofilm pH drops sharply from 6.3 to 5.2 in the first 30 minutes and then remains constant for the remainder of the experiment. The wastewater biofilm follows a similar trend, though the magnitude of the pH change is lower (plateau value at 5.6 at 30 minutes). This result is similar to the behavior observed in the suspended cultures, though the kinetics are much faster in the biofilm. The increased rate of pH change in the biofilm is most likely due to the fact that diffusion is hindered in the biofilm as compared to the stirred suspensions, allowing acidic metabolites to accumulate in the biofilm and change the local pH much more quickly.

The biofilm imaging experiments were performed without shaking or perfusion in order to maintain a stable field of view over the course of the experiment. Therefore, the rate of oxygen diffusion was probably low and anoxic zones may have developed within the biofilms. So, in contrast to the planktonic cultures, it is possible that the drop in pH observed in the biofilms is the combined result of different metabolic processes, *i.e.* aerobic and anaerobic respiration and fermentation. In the absence of oxygen *E. coli*, for instance, is capable of fermenting glucose as well as respiring nitrate. In the case of the wastewater culture biofilm, the presence of microorganisms capable of fermenting glucose (such as other species of enteric bacteria, *Clostridium*, *Lactobacillus* and even yeasts) might explain the presence of the low pH microenvironments.

### *4.3 Discussion*

In nanobiotechnology, tools of nanotechnology are used to study biology and in particular to further the goals of biotechnology. Over the past two decades, fueled

by the discovery of fluorescent semiconductor nanocrystals, an explosion has taken place in the development of fluorescent nanoparticles and nanoparticle sytems for imaging, sensing and diagnostic purposes[26,27]. Concurrently, microscale heterogeneities in biofilms, in particular sucrose-induced pH gradients in dental caries have been the subject of much research[6, 7, 14, 28-37]. Despite recent advances, however, present understanding of the complex processes in biofilms is incomplete[38]. The presence of biofilms at the solid-water interface in virtually all systems allows them to impact the quality of water in the environment, regulate the behavior of pollutatnts, enhance the resistance of infections to treatment and, in short, have effects on all ecosystems and the organisms that inhabit them. Concomitant with increasing recognition of the importance of biofilms is the need for better investigational tools. Development and execution of *in situ* monitoring and characterization of biofilms is expected to be particularly powerful to address present and future needs. Towards this end, the research presented here demonstrates, for the first time, the use of ratiometric fluorescent silica nanoparticle sensors as tools for high-resolution three-dimensional and time-domain functional fluorescence imaging of pH gradients in microbial biofilms. These nanoparticle sensors provide a minimally-invasive route to quantitative chemical imaging with resolution limited only by the microscopy system in use.

In order for nanoparticle sensor-based functional imaging of biofilms to work, the nanoparticle probes must intimately mix with, and stay in the extracellular matrix of the biofilm. Interestingly, through performing experiments with 70, 30 and 10 nm diameter silica particles, we found only the smallest bare C dot sensors provided the desired effective and homogeneous staining. There are several effects, which, by themselves or in combination could explain these observations. Gels of polysaccharides and fibrous proteins fill the intercellular spaces of biofilms. First,

fluid gaps between these elements of the extracellular matrix could simply be too small for the bigger particles to penetrate. Second, it is expected that mixing between nanoparticles and polymer matrices is size dependent for entropic reasons. In fact, such entropic size dependencies have been theoretically predicted and experimentally observed[39-41]. For mixing to occur, polymer chains must wrap around the nanoparticles, a process which becomes more entropically unfavorable as the particle size increases relative to the polymer size. Because polymer dimensions scale with only the square root of the number (N) of monomer units constituting them (ideal case[42]) particle size quickly outgrows chain size. Plugging in relevant numbers for extracellular matrix polymer sizes suggests that it is not unreasonable to expect the critical particle size for demixing to be between 10 and 30 nm. Third, the electrostatic repulsion between the negatively charged particle surfaces (the isoelectric point of silica is between pH 2-3) and biofilm extracellular matrix could cause a similar size-dependent effect. The electrostatic repulsion energy for particles of uniform surface charge scales approximately with the surface area of the particles[43], such that 70 nm diameter particles would experience a ~50-fold stronger repulsion than 10 nm diameter particles, making their inclusion into the biofilm much less favorable. While repulsive electrostatic effects will be partially screened by the ions in solution (*e.g.* 0.05M NaCl in LB) they may still affect the behavior at small length scales. Irrespective of which of these effects dominates the behavior, in all cases particle size becomes a critical design criterion for nanoparticle probes for biofilm interrogation.

The dyes in the C dot sensors are shielded by the silica matrix from interactions with extracellular matrix components that can bias the results, which simultaneously renders the particles biocompatible for use in both prokaryotic and higher biological systems with minimal toxicity. The enhanced photostability of the silica-encapsulated dye molecules also facilitates high-resolution measurements in xyz

and xy-time spaces without compromising sensitivity. Although the long wavelength photons used in multiphoton imaging give greater penetration depth than single photon imaging, for this work a dual-excitation, single-photon system was chosen to provide a large spectral separation between sensor and reference emissions. Several recent reviews further elaborate on the relative merits of single and multiphoton imaging techniques[44, 45].

The sensor/reference dye combination chosen for this work is well suited to the pH values in living biofilms, but other combinations can be synthesized to study environments with more extreme pH gradients such as microbial mats[46], insect midguts[47, 48] and river or lake sediments exposed to acid mine drainage[49], and the sediments of lakes impacted by acid rain. Substituting a fluorophore with a more acidic or basic $pK_a$ such as Oregon Green 514 or carboxynaphthofluorescein (4.8 and 7.6 respectively[50]) for fluorescein allows the linear range of the particles to be tailored. Moreover, by changing to other dyes, it is possible to quantitatively measure other variables of interest such as redox potential, oxygen status or concentration of ions such as $Ca^{+2}$ and $Mg^{+2}$ without significantly altering the particle architecture. Such nanoparticle probes, if designed appropriately, should provide powerful tools for future *in situ* monitoring and characterization of complex biofilms.

### *4.4 Methods*

#### *4.4.1 C Dot Sensors*

C dot sensors with 70, 30 and 10 nm diameters were grown via modified Stöber silica nanoparticle syntheses[23, 51]. Amination was performed using 3-aminopropyltriethoxysilane (APTS) as a surface-silanizing agent. The 10 nm diameter bare silica particles, which were ultimately used for all of the functional three-

dimensional reconstructions shown here, consist of a particle core covalently incorporating Cy5 as an environmentally insensitive reference dye via coupling to a reactive silane, surrounded by a shell covalently incorporating fluorescein dye (FITC) through coupling to a reactive silane. FITC was chosen for its $pK_a$ of 6.4, which is within the range of interest for this biological system. At high pH (9 and above), fluorescein exists in the di-anionic charge state and exhibits a quantum yield of approximately 93%, while at low pH (4.5 and below) the dye is protonated to the monoanion state with a quantum yield of approximately 37% (Figure 4.1 b)[50]. Cy5 has a quantum yield that is constant within this pH range making it an ideal internal standard. Additional information on the synthesis and characteristics of these particles may be found elsewhere[15, 19, 23].

### *4.4.2 Culture and Media*

*E. coli* PHL628, an adherent K-12 MG1655 derivative was used as the test bacterium for the pure-culture experiments. This strain has a single point mutation at position 43 in the regulatory OmpR protein that is responsible for the sessile phenotype. This mutation results in an overproduction of curli, which are optimally expressed at temperatures below 30ºC, at low nutrient concentrations and at low medium osmolarity; hence, growth of the culture as a collection of free-swimming organisms or as an attached community can be controlled by changing growth conditions[52].

The cultures were grown in a solution of one part Luria-Bertani (LB) medium (which contained, per liter, 10 g NaCl, 10 g tryptone and 5 g yeast extract) and two parts water and which was sterilized by autoclaving at 121ºC before use. All experiments performed with *E. coli* PHL628 were supplemented with kanamycin (50 mg/L). Suspended cultures were grown at 37ºC with rotary shaking at 150 rpm.

Attached cultures were grown in 35 mm Petri dishes with an untreated 14 mm Microwell No. 1.5 coverglass at the bottom surface (MatTek, Ashland, MA). After inoculation, the cells were kept at 30ºC with rotary shaking at 30 rpm. Every 48 hours the spent media was discarded and fresh media was added. Biofilms were grown for a period of 7 to 8 days. Approximately 9 hours prior to imaging, C dot sensors of different sizes and surface chemistries were added (to a concentration of 50 nM, in the case of the 10 nm C dot sensors) and the cultures were continuously stirred for 4 hours. A final media change was performed 5 hours prior to imaging to remove unbound dots.

The mixed-culture seed (potentially containing archaea and eukaryotic microorganisms *e.g.* fungi and protozoans in addition to bacteria)[53] came from a municipal wastewater treatment facility in Ithaca, NY. Biofilms and suspended cultures of the mixed cultures were grown following the same protocols described above.

### *4.4.3 Growth Curves*

To demonstrate the biocompatibility and low toxicity of the core-shell silica nanoparticles, 10 nm diameter sensor particles and dye-free nanoparticles of the same size were added to diluted LB medium at varying concentrations representative of biofilm growth conditions (18-50 nM). The solutions were then inoculated at 1% volume with either *E. coli* PHL628 cultures or mixed wastewater cultures. 200 µL aliquots of the cultures were placed in sterile, clear 96-well plates and optical density (OD) at 600 nm was recorded until stationary phase was reached. OD was measured using a Biotek multi-detection microplate reader equipped with Synergy HT and KC4 software. The microplate reader maintained the cultures at 37ºC with shaking prior to each measurement, which were performed at 20 minute intervals. Each condition was

analyzed in triplicate in addition to sterile controls both with and without particles. Reported ODs correspond to the absorbance measured from the bottom of each well (10.67 mm deep and 6.35 mm in diameter) in the plate; therefore, OD numbers are not comparable to standard OD measurements with 1 cm path-length cuvettes.

### *4.4.4 pH analysis in suspended cultures*

A calibration curve for C dot sensors was generated by mixing the dots with a series of pH-adjusted phosphate buffered saline solutions (pH 4.5 to pH 8.0) and measuring sensor (green) and reference (red) emission spectra upon excitation at 488 and 638 nm, respectively, on a PTI spectrofluorometer (Fig S1a). For each measurement, the peak intensity ratio ($F_i = I_{FITC} / I_{Cy5}$) was plotted versus pH and analyzed by a modified Henderson-Hasselbalch equation (Eq. 1) where $F_{min}$ and $F_{max}$ are the extreme values of $F_i$ at low and high pH, respectively, to determine the $pK_a$ and generate a calibration curve (Appendix B, Figure B.1d).

100 mL of overnight cultures of *E. coli* PHL628 grown in 1/3 LB were spiked with a concentrated glucose solution to achieve final concentrations of 90 mM glucose or an equal volume of distilled water (control). For the following 12 hours, 700 µL aliquots were retrieved from the spiked flask as well as the 0 mM glucose control and placed in cuvettes where the suspensions were mixed with C dots at 180 nM. Fluorescence in the green and red channel was recorded at the excitation and emission wavelengths described above. pH was simultaneously recorded with a UP-10 Denver Instrument pH meter. The experiment was simultaneously run with the mixed wastewater culture. Next, the relationship obtained from the calibration curve ($r^2$= 0.99) was used to calculate the pH of the cell suspensions.

### *4.4.5 Confocal Fluorescence Imaging*

All biofilm images were collected using a Leica TCX-SP2 Confocal Laser Scanning Microscope (CLSM) equipped with Argon ion and HeNe lasers. A 40x 0.8 NA water immersion objective was used for all imaging. 512 x 512 pixel TIF images were collected at 12-bit color depth in xy mode. Image stacks were generated by sequential imaging in 1μm steps through the biofilm.

To determine the spatial distribution of pH microenvironments within the biofilms, both pure culture *E. coli* PHL628 and mixed-culture films were grown and mixed with the sensors as described above. The samples were maintained at room temperature under constant shaking until imaging. The biofilms were concurrently imaged using transmitted light and fluorescence with excitation at 488 and 638 nm and appropriate emission filter settings. Particle-free biofilms were similarly imaged to control for background fluorescence. In order to record pH variations in biofilms following a glucose spike, an initial series of images was taken as a baseline, followed by a glucose addition that resulted in a final concentration equal to that used for the suspended cultures (90 mM). The same field was imaged every 30 minutes for the next 1.5 hours. For calibration purposes aliquots of phosphate-buffered saline solutions were mixed with particles to a final concentration of 15 μM and imaged in 96-well plates.

### *4.4.6 Image Analysis*

Example analysis files are included in the supplemental information as MATLAB m-files. Briefly, all image files were loaded into MATLAB 7.4.0 using the *imread* command and background-corrected based on average background images taken at each image setting. For the calibrations, replicates in each channel, at each pH, were median filtered (to remove noise) and averaged prior to pixel-wise division

of the green (sensor channel) by the red (reference) channel to determine $F_i$ ($I_{FITC}/I_{Cy5}$). The mean and standard deviation of this ratio were calculated across each image and used as the $F_i$ values in the modified Henderson-Hasselbalch equation shown above (Eq. 4.1).

For the biofilm images, each sensor and reference channel image was pixel-wise divided to generate $F_i$ values throughout the imaging field and the pH was calculated at each point which contained sufficient reference intensity to be considered above background. The 512x512 arrays of pH values were scaled for output as 8-bit grayscale TIFs from MATLAB in the order that they were read-in and appended with a pH scale bar. The images were then imported into Osirix DICOM image processing software[54]. Originally designed for MRI, CT and PET image analysis, the software creates three-dimensional tomographs from two-dimensional image stacks in a variety of false-spectrum colors and allows for easy manipulation of the data and export to still images (Figures 4.3-5) as well as video (Supplementary Information).

### *4.5 Acknowledgments*

We appreciate the assistance of Carol Bayles and the Microscopy and Imaging Facility of the Cornell Biotechnology Research Center. Gabriela Hidalgo was funded through a CONACYT graduate fellowship. This work was supported, in part, by NSF grant EAR-0311767. Andrew Burns was supported by the Cornell Nanobiotechnology Center (NBTC), an STC center of the NSF under agreement No. ECS-9876771.

# REFERENCES


[1] L. Stoodley, J. Costerton, and P. Stoodley, *Nature Rev. Microbiol.* , 2004, **2**, 95.

[2] C. K. Hope and M. Wilson, *J Microbiol Methods*, 2003, **54**, 403.

[3] C. J. Daughney, J. B. Fein, and N. Yee, *Chemical Geology*, 1998, **144**, 161.

[4] M. Shannon, P. Bohn, M. Elimelech, J. Georgiadis, B. Marinas, and A. Mayes, *Nature*, 2008, **452**, 301.

[5] P. S. Stewart and M. J. Franklin, *Nat Rev Microbiol*, 2008, **6**, 199.

[6] J. M. Vroom, K. J. De Graw, H. C. Gerritsen, D. J. Bradshaw, P. D. Marsh, K. G. Watson, J. J. Birmingham, and C. Allison, *Applied and Environmental Microbiology*, 1999, **65**, 3502.

[7] P. D. Marsh and D. J. Bradshaw, *J Ind Microbiol*, 1995, **15**, 169.

[8] R. E. Marquis, *J Ind Microbiol*, 1995, **15**, 198.

[9] H. L. Ehrlich, 'Geomicrobiology', CRC Press, 2002.

[10] P. Gilbert, T. Maira-Litran, A. J. McBain, A. H. Rickard, and F. W. Whyte, *Adv Microb Physiol*, 2002, **46**, 202.

[11] R. T. Cirz, J. K. Chin, D. R. Andes, V. de Crecy-Lagard, W. A. Craig, and F. E. Romesberg, *PLoS Biol*, 2005, **3**, e176.

[12] L. Dethlefsen, M. McFall-Ngai, and D. Relman, *Nature*, 2007, **449**, 811.

[13] A. Gieseke, S. Tarre, M. Green, and D. de Beer, *Appl Environ Microbiol*, 2006, **72**, 4283.

[14] R. C. Hunter and T. J. Beveridge, *Appl Environ Microbiol*, 2005, **71**, 2501.

[15] A. Burns, H. Ow, and U. Wiesner, *Chemical Society Reviews*, 2006, **35**, 1028.

[16] C. Xi, D. Marks, S. Schlachter, W. Luo, and S. Boppart, *Journal of Biomedical Optics*, 2006, **11**, 034001.

[17] K. Kemner, S. Kelly, B. Lai, J. Maser, B. S. Eaglesham, E. O'Loughlin, D. Sholto-Douglas, Z. Cai, M. Schneegurt, C. Kulpa, and K. Nealson, *Science*, 2004, **306**, 686.

[18] K. Ohki, S. Chung, Y. Ch'ng, P. Kara, and R. Reid, *Nature*, 2005, **433**, 597.

[19] A. Burns, P. Sengupta, T. Zedayko, B. Baird, and U. Wiesner, *Small*, 2006, **2**, 723.

[20] Y. E. L. Koo, Y. Cao, R. Kopelman, S. M. Koo, M. Brasuel, and M. A. Philbert, *Anal. Chem.*, 2004, **76**, 2498.

[21] Z. Gryczynski, I. Gryczynski, and J. R. Kalowicz, *Methods in Enzymology*, 2003, **360**, 44.

[22] H. A. Clark, M. Hoyer, M. A. Philbert, and R. Kopelman, *Anal. Chem.*, 1999, **71**, 4831.

[23] D. Larson, H. Ow, H. Vishwasrao, A. Heikal, U. Wiesner, and W. Webb, *Chemistry of Materials*, 2008, **20**, 2677.

[24] J. Choi, A. Burns, R. Williams, Z. Zhou, A. Flesken-Nikitin, W. Zipfel, U. Wiesner, and A. Nikitin, *Journal of Biomedical Optics*, 2007, **12**, 064007 (1.

[25] O. Vidal, R. Longin, C. Prigent-Combaret, C. Dorel, M. Hooreman, and P. Lejeune, *J Bacteriol*, 1998, **180**, 2442.

[26] X. Michalet, F. Pinaud, L. Bentolila, J. Tsay, S. Doose, J. Li, G. Sundaresan, A. Wu, S. Gambhir, and S. Weiss, *Science*, 2005, **307**, 538.

[27] Y. Piao, A. Burns, J. Kim, U. Wiesner, and T. Hyeon, *Advanced Functional Materials* 2008, **accepted**.

[28] G. Sezonov, D. Joseleau-Petit, and R. D'Ari, *J. Bacteriol.*, 2007, **189**, 8746.

[29] N. B. Ramsing, M. Kuhl, and B. B. Jorgensen, *Appl Environ Microbiol*, 1993, **59**, 3840.

[30] M. Kuhl and T. Fenchel, *Microb Ecol*, 2000, **40**, 94.

[31] M. Kuhl, *Methods Enzymol*, 2005, **397**, 166.

[32] M. J. Ferris, T. S. Magnuson, J. A. Fagg, R. Thar, M. Kuhl, K. B. Sheehan, and J. M. Henson, *Environ Microbiol*, 2003, **5**, 954.

[33] D. de Beer, P. Stoodley, F. Roe, and Z. Lewandowski, *Biotechnology and Bioengineering*, 1994, **43**, 1131–1138.

[34] C. H. Sissons, L. Wong, E. M. Hancock, and T. W. Cutress, *Arch Oral Biol*, 1994, **39**, 507.

[35] C. H. Sissons, T. W. Cutress, G. Faulds, and L. Wong, *Arch Oral Biol*, 1992, **37**, 913.

[36] C. Sissons, *N Z Dent J*, 1998, **94**, 56.

[37] S. Okabe, H. Satoh, and Y. Watanabe, *Appl Environ Microbiol*, 1999, **65**, 3182.

[38] T. Bartrand, M. Weir, and C. Haas, *NSF Environmental Engineering Science*, 2007, **24**, 863.

[39] R. Thompson, V. Ginzburg, M. Matsen, and A. Balazs, *Science*, 2001, **292**, 2469.

[40] M. Mackay, A. Tuteja, P. Duxbury, C. Hawker, B. V. Horn, Z. Guan, G. Chen, and R. Krishnan, *Science*, 2006, **311**, 1740.

[41] S. Warren, F. DiSalvo, and U. Wiesner, *Nature Materials*, 2007, **6**, 156.

[42] P. DeGennes, 'Scaling Concepts in Polymer Physics', Cornell University Press, 1979.

[43] M. Hermansson, *Colloids and Surfaces B*, 1999, **14**, 105.

[44] L. M. Macpherson and C. Dawes, *J Dent Res*, 1991, **70**, 1230.

[45] F. Helmchen and W. Denk, *Nature Methods*, 2005, **2**, 932.

[46] E. L. Botvinick and J. V. Shah, *Methods Cell Biol*, 2007, **82**, 81.

[47] C. Vasconcelos, R. Warthmann, J. A. McKenzie, P. T. Visscher, A. G. Bittermann, and Y. van Lith, *Sedimentary Geology*, 2006, **185**, 175.

[48] J. A. Dow, *J Exp Biol*, 1992, **172**, 355.

[49] A. Brune, D. Emerson, and J. A. Breznak, *Appl Environ Microbiol*, 1995, **61**, 2681.

[50] R. P. Haugland, 'The Handbook - A guide to Fluorescent Probes and Labeling Technologies', Invitrogen, Inc, 2007.

[51] W. Stober, A. Fink, and E. Bohn, *Journal of Colloid and Interface Science*, 1968, **26**, 62.

[52] B. Xing, J. Rao, and R. Liu, *Mini Rev Med Chem*, 2008, **8**, 455.

[53] M. T. Madigan, J. M. Martinko, and J. Parker, '*Brock Biology of Microorganisms*', Prentice Hall, 2003.

[54] A. Roset, L. Spadola, and O. Ratib, *J. Digital Imaging*, 2004, **17**, 205.

# CHAPTER 5

# FLUORESCENT SILICA NANOPARTICLES AS *IN VIVO* IMAGING AGENTS FOR NANOMEDICINE*


## *5.0 Abstract*

The development of high-contrast, highly-specific, molecularly-targeted nanoparticle probes exhibiting high biostability, minimal toxicity and fast clearance profiles is expected to improve *in vivo* detection, characterization and treatment of human disease. Fluorescence imaging has proven invaluable to researchers in biology and biomedicine and is poised to become an effective tool for clinical applications. We describe a combination of thorough photophysical brightness and photobleaching characterization with the development of more quantitative protocols for fluorescence-based evaluation of biodistribution and clearance of hybrid core-shell silica nanoparticles in mice. When coated with ethylene glycol chains, fluorescent particles of ~3 and 6 nm diameter, containing near-infrared Cy5 dyes, exhibited effective renal clearance on timescales of several hours. *In vivo* whole body fluorescence imaging and post-mortem tissue and fluid analysis was corroborated by positron emission tomography results. Because of the versatility in silica chemistry and structure, these results suggest that fluorescent core-shell silica nanoparticles may develop into a powerful materials platform for the exciting field of nanomedicine.



* Prepared for Submission as: Andrew A. Burns, Jelena Vider, Hooisweng Ow, Erik Herz, Oula Penate-Medina, Martin Baumgart, Steven M. Larson, Ulrich B. Wiesner, Michelle Bradbury. "Fluorescent Silica Nanoparticles as *in Vivo* Imaging Agents for Nanomedicine"

### *5.1 Introduction*

Advances in the fundamental science and engineering underlying medical practice are poised to change the patient experience towards more personalized, predictive and preventive medicine in the coming decade. Explosive growth in the fields of molecular biology, genomics, proteomics, and informatics in parallel with advances in nanotechnology and imaging is transforming our understanding of disease at the molecular level[1-3] and beginning to create novel solutions to diagnostic and therapeutic challenges. In particular, nanotechnology platforms have enabled advances in molecular diagnostics and proteomic technologies, as well as increasing our understanding of the molecular mechanisms of diseases such as cancer. Employing highly-specific, molecularly-targeted probes exhibiting high biostability, minimal toxicity, and fast clearance profiles in conjunction with high-resolution imaging strategies will be mandatory for improving *in vivo* detection sensitivity, characterization, and treatment monitoring of tumors. Currently, morphologic features of lesions identified on anatomic imaging often preclude distinction of benign from malignant lesions, as well as limit response assessments. Although functional imaging methods are steadily being incorporated into patient scanning protocols for deriving information related to tumor metabolism and physiology, these methods remain limited in their sensitivity and specificity given the probes currently available.

Optical fluorescence imaging is comprised of a suite of technologies that are being applied to a rapidly growing array of *in vivo* biological and medical applications, and offer clear potential for translation to the clinic [1-4], particularly for endoscopic and open-surgical procedures. The combination of high sensitivity and imaging speed, advantageous for high-throughput screening studies, along with relatively low complexity and cost, makes *in vivo* fluorescence imaging very appealing for surface-based diagnostic detection, drug discovery, molecular pathway

analysis, as well as intraoperative mapping of tumor margins and nodal spread of disease. Limitations of commonly used planar fluorescence reflectance imaging methods include limited depth resolution (< 1 cm) due to intrinsic tissue signal attenuation, as well as autofluorescence arising from tissue organic components and absorbed dietary constituents, which reduce signal-to-noise ratios. Moreover, only relative, rather than absolute, quantification of imaging data sets can be achieved, given the dependence of the measured signal on depth and sample composition, but the data can be validated by implementation of rigorous experimental procedures.

Current state-of-the-art fluorescence imaging probes, in use as biological contrast agents, can be broadly classified as single conventional fluorophores (organic dyes[2], fluorescent proteins[5]), quantum dots (QDs), and hybrid architectures incorporating one or more of these emitters in an inert matrix[6-10]. To realize the broad potential of optical reflectance imaging, while addressing the above limitations, a new generation of luminescent nanoparticle probes, which emit photons in the near-infrared region (NIR, 650-900 nm), have been developed. Compared to current visible emitters, NIR-emitting probes exhibit decreased tissue attenuation and autofluorescence from non-target tissue, thereby maximizing brightness and contrast per dose. Moreover, these probes can be designed to enhance clearance, minimize toxicity, and eliminate the possibility of probe interference with other imaging or therapeutic techniques. Probes must be made from inert and biocompatible materials and designed to efficiently exit the body, either by biodegradation or intact excretion after serving their purpose. These criteria have been addressed individually by various approaches, but none to date have simultaneously achieved them in a single probe.

Research on probes for optical and other imaging modalities has shown renal clearance to be the most effective route of excretion, as opposed to liver sequestration, subsequent reticuloendothelial macrophage uptake, and eventual hepatobiliary

excretion into the intestinal tract[11]. Further, this body of work has defined many of the key criteria for renal clearance of a contrast agent. By regulating the fluid and chemical homeostatic balance in blood, the kidneys serve as an ideal conduit for the filtration of contrast agents from the bloodstream. Research has shown that the glomerular filtration rate of a particular material is predominantly determined by its size and surface charge.

Combining the dendrimer-based work of Kobayashi and Brechbiel[12] with the recently presented quantum dot work of the Bawendi and Frangioni groups[13], the consensus is that the optimal size balance to ensure both reasonable circulation lifetimes and efficient clearance is between 3-7 nm in hydrodynamic diameter. Probes well below this size (including molecular dyes) are prone to extravasation and non-specific dispersal throughout tissue[12, 14], which increases background fluorescence and potentially leads to prolonged retention. Larger probes (such as most quantum dots and hybrid architectures to date) tend to accumulate in the liver, where they are often taken up by macrophages in the reticuloendothelial system, which, in turn, eventually mediate their removal[7, 12, 13]. While ultimately effective, this mode of clearance prolongs exposure to the contrast agent beyond the relevant time frame for imaging, increasing the potential for toxicity and interference with other imaging or therapeutic modalities.

A probe's surface chemistry is a key determinant of its fate *in vivo*. Materials with a net surface charge (either positive or negative) tend to become opsonized[11] by serum proteins, effectively increasing probe size and preventing renal excretion. Both neutral and zwitterionic materials have been shown to clear effectively via the kidneys[12, 13], although chemically neutral surfaces such as poly- or oligo-ethylene glycol chains are generally more bio-inert than zwitterionic surfaces containing reactive amine and/or carboxylate groups[15].

Recent work has demonstrated quantum dots with sufficiently small hydrodynamic size to achieve renal filtration[13]. However, despite their excellent brightness and photostability for *in vivo* imaging applications, the risk of systemic toxicity remains high, given their incorporation of heavy metals (*e.g.* Pb, Cd), precluding their widespread use and ultimate clinical translation. Further, because of their size-dependent emission wavelengths, development of quantum dots of suitable stabilized size in the desirable far-red/near-infrared spectral region has thus far proven difficult.

The well-known limitations of quantum dots in their present form have accelerated the development of alternative particle platforms that are non-toxic, efficiently excreted, exhibit high per-probe brightness levels and, most importantly, are poised for clinical translation. We have sought to simultaneously achieve all of these criteria in a single particle platform by synthesizing fluorescent core-shell silica nanoparticles, referred to as C dots. The hydrodynamic radius of this probe is tunable down to the sub-4 nm range, a size previously thought to be unattainable. These nanoparticles covalently incorporate organic dyes into an amorphous silica matrix to prevent dye leaching (schematically depicted in Figure 5.1a)[6, 9, 16]. Larger C dots (15 - 40 nm diameter) have been shown to exhibit significantly enhanced dye quantum yields due to increases in radiative and decreases in non-radiative decay rates by the silica matrix, as well as enhanced photostability compared to the parent fluorophore[8, 9]. Prior work has demonstrated ~30 nm diameter particles with pure silica surfaces as imaging agents for *in vitro* (*e.g.* antibody-mediated labeling)[9] and *in vivo* (*e.g.* sentinel lymph node mapping)[7] applications. One of the particular advantages of this architecture is the ability to control particle size independently of the emission wavelength, which led us to develop long-wavelength probes tuned for renal clearance to address the challenges of *in vivo* imaging.

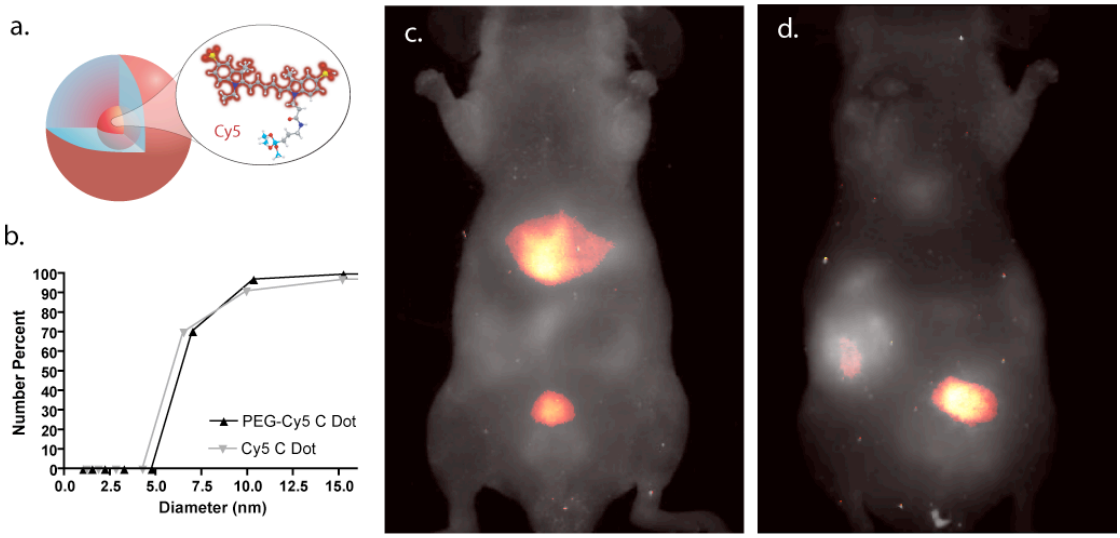


Figure 5.1a. A schematic representation of Cy5 reactive dye incorporated into the core of an amorphous silica nanoparticle. b. DLS (number average) plot of particle size for bare silica (grey) and PEG-coated (black) Cy5-containing silica nanoparticles (C dots). c, *In vivo* imaging of spectrally-demixed Cy5 particle fluorescence (false-spectrum) overlaid on visible light imaging of nude mice 30 minutes post-injection with bare silica C dots, showing particle accumulation in the liver and bladder. d. *In vivo* imaging of spectrally-demixed Cy5 particle fluorescence (false spectrum) overlaid on visible light imaging of nude mice 30 minutes post-injection with PEG-ylated Cy5 C dots showing particle accumulation in kidney and bladder.

### *5.2 Results & Discussion*

Initial syntheses derived from methods published elsewhere[8, 17, 18], using reactive derivatives of the organic dye Cy5 (GE Healthcare) which exhibits an emission maximum above 650 nm (Figure 5.2b) yielded nanoparticles in the 6-10 nm diameter range, as shown by Dynamic Light Scattering (DLS) results in Figure 5.1b. Athymic nude (nu/nu) mice were placed on a special corn and wheat-based diet for 5 days prior to performing *in vivo* imaging studies to significantly reduce and/or eliminate tissue autofluorescence. Standard high protein diets containing alfalfa and soy have been shown to contribute to autofluorescence from the gastrointestinal tract and skin of the animal at 674 nm, which has been linked to the products of chlorophyll metabolism[19].

*In vivo* whole-body near-infrared fluorescence (NIRF) imaging of bare silica nanoparticles in nude mice showed considerable renal clearance 30 minutes post-injection, but with a significant accumulation remaining in the liver (Figure 5.1c), with eventual biliary excretion into the intestine over the ensuing 24 hours (data not shown). Based on these promising results, the particles were covalently coated with methoxy-terminated polyethylene glycol chains (PEG, ~0.5 kD) to prevent opsonization and further enhance particle clearance while maintaining small hydrodynamic size. This treatment noticeably decreased liver retention and resulted in increased renal filtration into the bladder at 30 minutes post-injection, as shown by *in vivo* fluorescence imaging (Figure 5.1d). These probes were well tolerated, with no adverse effects or animal deaths observed over the course of the study.

On the basis of these initial *in vivo* data, a more detailed biodistribution and clearance study of coated core-shell silica nanoparticles was undertaken on two sets of PEG-ylated Cy5-containing core-shell silica particles to assess the effects of probe

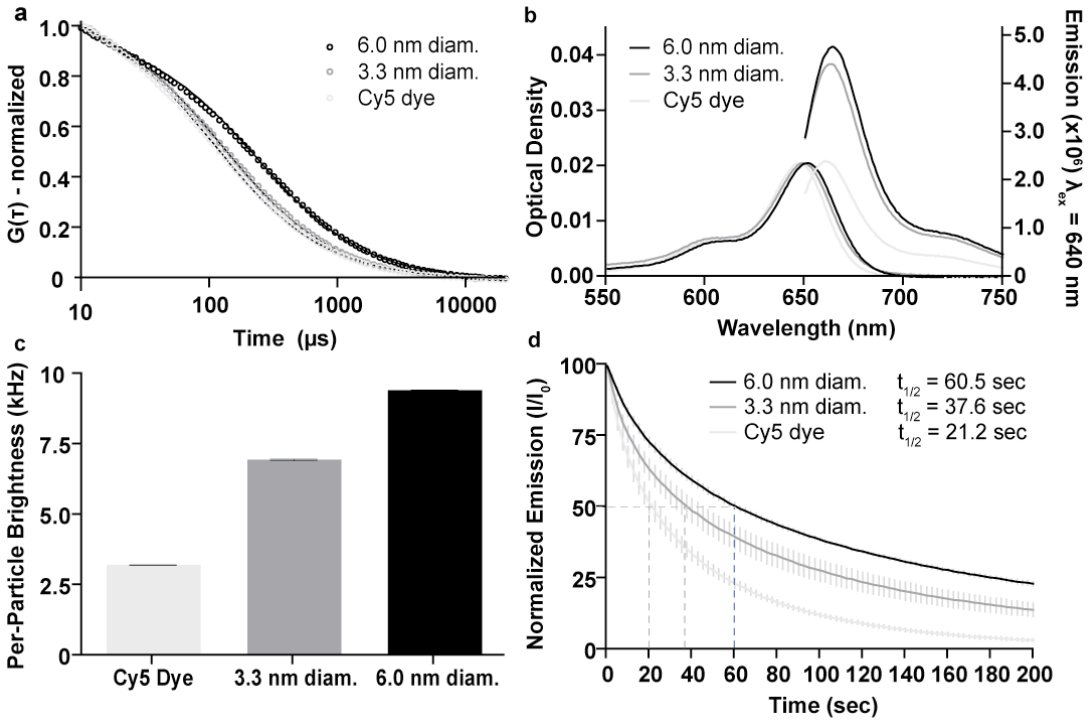


Figure 5.2a. FCS data and fits for of Cy5 dye (light grey), 3.3 nm diameter (dark grey) and 6.0 nm diameter (black) Cy5-containing PEG-coated C dots showing the differences in diffusion time resulting from the different hydrodynamic sizes of the different species. b. Absorption and emission spectra of Cy5 dye (light grey), 3.3 nm diameter (dark grey) and 6.0 nm diameter (black) PEG-coated C dots, comparing the peak photoemission of the three species at equal peak absorption optical density to demonstrate the enhanced performance of the dye following the encapsulation reaction. c, Relative brightness comparison of free dye (light grey) with 3.3 nm (dark grey) and 6.0 nm diameter (black) C dots, measured as count rate per molecule/particle as determined from the FCS curves, demonstrating the enhancement effects over free dye that increase with particle size. d, Photobleaching data for Cy5 dye (light grey), 3.3 nm diameter (dark grey) and 6.0 nm diameter (black) PEG-coated C dots under ~3.5mW laser excitation, demonstrating the enhanced photostability of the dye following silica encapsulation. The time at which 50% of the photoemission is reduced ($t_{1/2}$) is indicated for each of the different species.

size on biodistribution. In collaboration with Hybrid Silica Technologies (HST, Ithaca, NY), the particle synthesis was further optimized and particles with hydrodynamic diameters of 3.3+/-0.1 nm and 6.0+/-0.1 nm as measured by fluorescence correlation spectroscopy (FCS)[20] were generated (Figure 5.2a). Before the animal work, the photophysical properties of these particles were thoroughly investigated to establish their performance levels as compared to free dye.

Despite the extremely small size of the particles, the silica-encapsulated dye molecules exhibited several notable photophysical enhancements over free dye, consistent with earlier studies[8, 9, 21]. By absorption and emission spectroscopy (ensemble averages, Figure 5.2b) as well as FCS (single molecule/particle method, Figure 5.2c) significant enhancements in brightness were observed. Furthermore, compared to the free dye, the 3.3 and 6.0 nm diameter dots exhibited roughly 2- and 3-fold increases in photobleaching half-life, respectively, when irradiated with a high-power 635nm laser as shown in Figure 5.2d[22]. In all cases, these improvements of photophysical properties scaled with increasing particle size[22]. Thus, these C dot probes are both brighter and more photostable than their free dye counterparts, creating an excellent fluorescent platform for *in vivo* imaging studies.

Physiological saline solutions of both particle sizes were separately injected intravenously into mice via the tail vein. Following NIRF imaging for determination of *in vivo* particle localization, mice were sacrificed at various time points after injection, ranging from 10 minutes to 48 hrs (n = 3 per time point) for tissue and fluid analysis using a fluorescence plate reader. These homogenized tissues and fluids were analyzed on the basis of calibration curves initially derived by serially diluting a range of particle volumes into control tissue homogenates and fluids from untreated (control) mice (Appendix C, Figure C.1). Although semi-quantitative estimates of *in vivo* nanoparticle behavior are obtained using either device [23], the increased sensitivity and

calibration offered by the fluorescence plate reader was used to confirm observed time-varying changes in relative whole-body particle distributions using NIRF imaging.

The samples were grouped as "retained" (blood, liver, kidney, lung, spleen) and "excreted" (urine) sources of particle fluorescence and all values were background-corrected and converted to percent of the initial dose (% ID) per animal based on the organ/fluid calibration curves. Analysis of the tissue samples showed minimal particle retention in the major organs of the body, with most of the fluorescence attributed to the circulating blood (Figures 5.3a and b). The net particle retention was calculated as the sum of the blood and tissue components, and was fit with an exponential decay curve to determine the kinetics of excretion (Figure 5.3 c). The larger (6.0 nm diameter) particles exhibited a longer tissue half life ($t_{1/2}$(3.3 nm) = 190 min, $t_{1/2}$(6.0 nm) = 350 min) and greater initial organ retention, as expected. After 48 hours (last data points in Figures 5.3c and d) both particle sizes exhibited minimal retention in the body ($R_{total}$(3.3 nm) = 1.0+/-0.1% ID, $R_{total}$(6.0 nm) = 2.4+/-0.6 % ID).

The major route of excretion for these particles is expected to be via renal filtration to the urine, given the small size and neutral surface of the particles. Thus, urine samples collected at the time of sacrifice were analyzed to determine the particle concentration per unit volume using a similar serial dilution calibration scheme as for the tissue homogenates (Appendix C Figure C.1). This information, in turn, was used to estimate the total renal clearance based on a conservative estimate of the average urine volume excreted per unit time[24] (Appendix C Table C.1) by measuring the area under the curve of concentration versus volume excreted. By this method, the percent of the

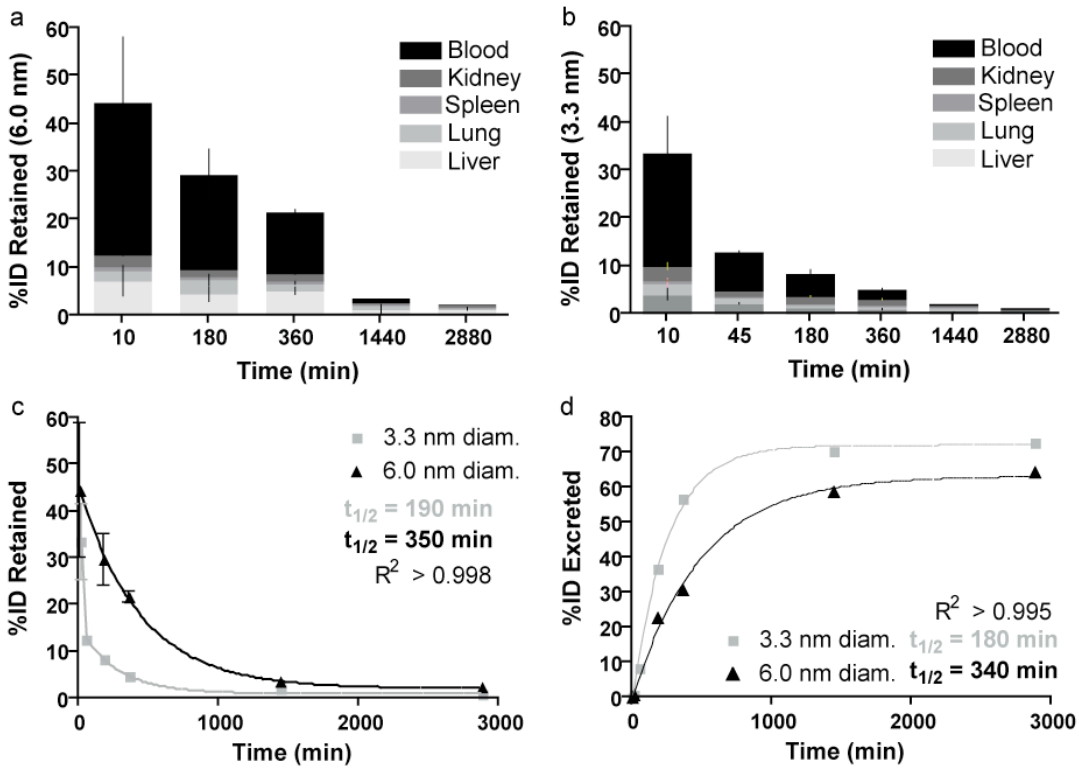


Figure 5.3a,b. Percent of initial particle dose (%ID) retained by blood (black) and tissues: liver (light grey), lung (mid-low grey), spleen (mid grey) and kidney (mid-high grey) for 6.0 nm (a) and 3.3 nm (b) diameter C dots at various time points from 10 minutes to 48 hours post-injection. c. Plot of retained particle concentration for 3.3 nm (light grey) and 6.0 nm (black) diameter C dots and the associated logarithmic decay fits and half-lives. d. Plot of estimated particle excretion for 3.3 nm (light grey) and 6.0 nm (black) diameter dots and the associated logarithmic fits and half-lives.

initial dose excreted over time was estimated as shown in Figure 5.3d for both particle sizes. Exponential fits of the resulting curves corroborated the kinetics seen in the tissue analysis, namely that the smaller (3.3 nm diameter) particles were more quickly and completely excreted. The urine half-lives of the two particle types were quite consistent between the tissue and urine results ($t_{1/2}$(3.3 nm) = 180 min, $t_{1/2}$(6.0 nm) = 360 min). Further, the estimated total excreted fraction ($E_{total}$) after 48 hours was higher for the smaller particles ($E_{total}$(3.3 nm) $\simeq$ 73 %ID versus $E_{total}$(6.0 nm) $\simeq$ 64 %ID), which is consistent with the filtration rates expected for particles of this size range[1, 12]. To account for the variation in urine volume and concentration due to circadian rhythm, animals in each cohort (time-point and treatment) were sacrificed at different times throughout the day.

These results are supported by the whole-body NIRF imaging data collected post mortem for each mouse (representative bladder images, Figure 5.4 and Appendix C Figures 2 and 3), in which particle fluorescence is visible in animals for up to 6 hours post-injection (Figures 5.4a-d and 5.4f-h for 3.3 and 6.0 nm diameter dots, respectively). The images were spectrally demixed based on reference samples to remove background fluorescence (e.g. food fluorescence), as evinced by the low background counts from the control animals (Figure 5.4j). Serial positron emission tomography (microPET) imaging over a 96-hr period following intravenous injection of $^{124}$I labeled coated C-dots corroborated the *in vivo* optical imaging findings (Appendix C Figure 4).

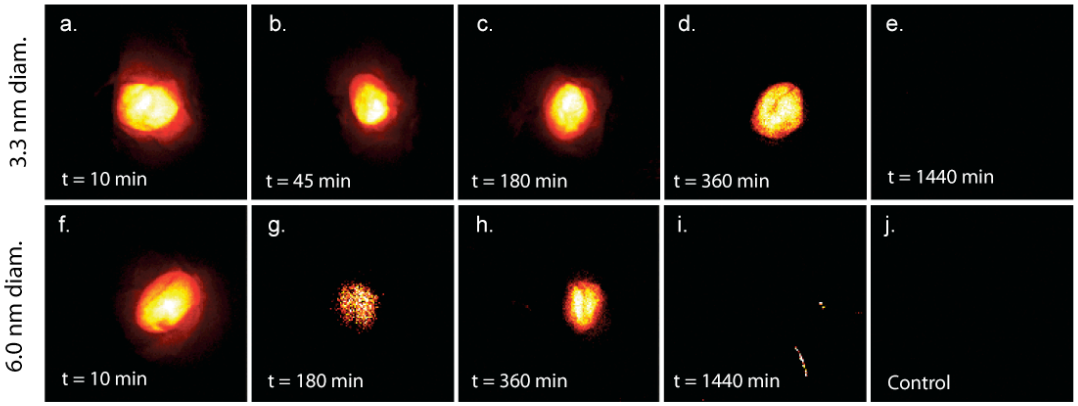


Figure 5.4a-e. False color images of Cy5 fluorescence (demixed) in intact mouse bladders showing the accumulation of 3.3 nm diameter dots over the course of the first six hours post-injection (a-d), followed by the negligible particle fluorescence seen at 24 hours post-injection(e). f-i. False color images of Cy5 fluorescence (demixed) in intact mouse bladders showing the accumulation of 6.0 nm diameter dots in the first six hours post-injection (f-h) and at the 24 hour endpoint (i). j. False-color image of a control mouse bladder. Further fluorescence and anatomical brightfield images can be found in the Supplementary Information Figures 2 and 3.

### *5.3 Conclusions & Outlook*

This study describes the first combination of thorough photophysical characterization (brightness and photobleaching) with the development of more quantitative protocols for fluorescence-based *in vivo* evaluation of a hybrid core-shell silica nanoparticle platform (C dots) containing a NIR fluorescent dye (Cy5). This platform has been designed to simultaneously yield bright fluorescent emission, high photostability and biocompatibility, and efficient renal excretion. Despite the small dot sizes, encapsulation of organic fluorophores in a silica matrix leads to enhancements in their photophysical properties, while, concomitantly achieving efficient renal excretion on the basis of a PEG-coated particle surface, particularly relevant for the larger particle size used here (6.0 versus 3.3 nm diameter). Optimization of the photophysical and biological characteristics of the non-functionalized C dot, as well as the attachment of a suitable radiolabel, serves as an initial step towards the development and deployment of novel, multimodal targeted probes as early detection and/or therapeutic vehicles for a broad range of biomedical applications. The hybrid architectural platform provides a versatile template for the attachment of peptides and other molecular moieties, and allows for incorporation of metal ions for use in combined imaging experiments. Such a multimodal platform may provide complementary information at both the tissue and cellular level, offering distinct advantages for translation to the clinic compared with unbound fluorescent dyes, simple radiolabeled constructs, and quantum dots. The findings of this study pave the way for this and other nano-sized probe technologies to address important biological issues.

### *5.4 Methods*

#### *5.4.1 Synthesis of Core-shell Silica Nanoparticles (C Dots)*

Particles were synthesized by a modified Stöber-type silica condensation as described in detail elsewhere[8, 17, 18]. Bare particles were dialyzed to deionized water, and ethylene glycol-coated particles were dialyzed to physiological saline (0.15M NaCl), through 3500 MWCO Snakeskin Dialysis Membranes (Pierce) and sterile-filtered through 0.2μm syringe filters. All samples were optical density-matched at their peak absorption wavelength (640 nm) prior to injection.

#### *5.4.2 Hydrodynamic Size Measurements by Dynamic Light Scattering (DLS)*

Particles dialyzed to water were measured on a Brookhaven Instruments Company BIC 200SM static/dynamic light scattering system using a HeNe laser ($\lambda$ = 632.8 nm). Due to overlap of the dye absorption with the excitation source, 15 minute integration times were used to achieve acceptable signal to noise ratios.

#### *5.4.3 Hydrodynamic Size Measurements by Fluorescence Correlation Spectroscopy (FCS)*

Particles dialyzed to water were diluted into physiological saline (0.15 M NaCl in $H_2O$) and measured on a Zeiss LSM 510 Confocor 2 FCS using HeNe 633 nm excitation. The instrument was calibrated for size prior to all measurements.

#### *5.4.4 Spectrophotometry and Spectrofluorometry*

Absorption-matched samples were prepared by appropriate dilution of water-dialyzed particles or water-diluted dye and measured in quartz cuvettes on a Varian Cary 5000 spectrophotometer (Varian, Palo Alto, CA). Fluorescence measurements

were performed on a Photon Technologies International Quantamaster Spectrofluorometer (PTI, Birmingham, NJ).

### *5.4.5 Photobleaching*

A custom photobleaching apparatus was constructed in our lab, which consisted of an 8mW (3.5mW at the sample) 635nm diode laser coupled to a 3.5x (0.10 NA) objective. The excitation beam was focused on a 0.4mm internal diameter glass capillary tube aligned parallel to the excitation beam in a custom 3-axis, tilt mount. Two microliters of appropriately diluted particles or dye (0.01 peak OD) were loaded into the capillary tube and irradiated for each trial, with all data shown recorded in triplicate. Emitted light was collected by a Perkin Elmer single photon counting module interfaced with a Correlator.com autocorrelator card. Twenty-minute time series were recorded at 2.5 second intervals, normalized to the peak intensity and analyzed by Prism Version 4.0c to determine photobleaching kinetics.

### *5.4.6 Animal Models*

Male Taconic NCRNU-M-M Homozygous (nu/nu) nude mice were purchased from Taconic Labs and studied at approximately 10 weeks of age. Mice were provided with water and fed Harlan Teklad Global Diet 2016, *ad libitum*, a 16% Protein rodent diet without soy, alfalfa, fish or animal protein to decrease background fluorescence in the spectral window of interest.

### *5.4.7 Biodistribution and Clearance Measurements*

Mice were individually injected intravenously with 200$\mu$l of fluorescent silica nanoparticles in physiological saline (0.15M NaCl) at a peak absorption of 0.30 OD (640 nm), to ensure delivery of equal amounts of contrast agent across the test groups.

Mice were sacrificed at various time points post-injection (10 min, 45 min, 180 min, 360 min 1440 min and 2880 min) by $CO_2$ asphyxiation and imaged post-mortem in a Cambridge Research Instruments Maestro imager. Given the expected slower kinetics of excretion of the larger 6.0 nm diameter particles, a longer 48 hour time point was used in lieu of a 45 minute time point. Images for spectral deconvolution were collected at 2nm intervals from 630nm to 850nm using a 575-605 bandpass excitation filter and a 645 nm longpass emission filter exposed at f/11 for 278ms. Spectral deconvolution algorithms were applied to the images collected to separate particle fluorescence from food-based and other intrinsic (background) emissions using Maestro Imaging Software v. 2.4.

Tissue and fluid samples (liver, kidney, spleen, lung, blood, and urine) were collected and frozen immediately on dry ice for later examination. Tissue samples were thawed and homogenized by ultrasonication following dilution of 3 $\mu$l $H_2O$/mg tissue with a Sonics Vibracell CV188 probe sonicator to facilitate pipetting. Fluid samples were thawed and used as collected. All samples were pipetted into black polystyrene 384-well plates (Thermo Scientific Microtiter Cliniplate 384) in triplicate (as sample volume allowed) and measured on a Tecan Safire plate reader ($\lambda_{ex}$ = 650 nm, $\lambda_{em}$ = 680 nm, 12 nm bandwidths). Fluids and tissue homogenates from control animals were analyzed to determine background levels. Excess fluid and homogenates were used to generate calibration curves by mixing samples with known volumes of particles, followed by serial dilutions with control homogenate or fluid to ensure that any background fluorescence or absorption / scattering would be taken into account. All plate reader data were analyzed and plotted with GraphPad Prism 4.0c. Following background subtraction, calibration curves were generated for each organ or fluid to determine particle concentration in each well. These calibration curves (Appendix C

Figure C.1) were applied to the background-corrected sample data to generate the particle per tissue / fluid data shown in Figure 5.3.

### *5.4.8 C Dot Radioiodination*

Radiolabeling of the PEG-ylated C dots was achieved by conjugation of tyrosine residues to the PEG chains using protocols described in the literature[25]. An aliquot of the coated silica nanoparticles bearing these tyrosine residues was radiolabeled using the IODOGEN method (Pierce, Rockford, IL)[26]. Briefly, 25µl of the coated nanoparticle in deionized water (0.039 mM) was incubated for 10 minutes in a 0.5mCi $^{124}$I in an Iodogen-coated tube. Final purification was performed using size exclusion chromatography (PD-10 column; GE Healthcare) with phosphate-buffered saline (pH 7.4) as the mobile phase. Non-tumor bearing mice (n=3) were intravenously injected with 8 pmol (200 µl) and serial microPET images were acquired using a dedicated small-animal PET scanner (Focus 120 microPET; Siemens Medical Solutions USA, Inc.). Mice were maintained under 2% isoflurane anesthesia in oxygen at 2 L/min during the entire scanning period. Fifteen minute to 1 hour static acquisitions were initiated at the time of injection of 25.9–55.5 MBq (200–300 mCi). An energy window of 410–590 keV and a coincidence timing window of 6 ns were used. Images were iteratively reconstructed using the ordered-subset expectation maximization (OSEM) technique. A 7 minute computed tomography (microCT) scan was additionally obtained 24 hours after injection using routine image acquisition variables (70 kVp, 90 mA-s with 2-mm aluminum filters). The microCT study was acquired immediately following the microPET study for anatomic co-registration purposes using in-house co-registration software and a custom-built imaging bed for immobilizing and fixing a small animal[27].

# REFERENCES


[1] J. V. Frangioni, *Current Opinion in Chemical Biology*, 2003, **7**, 626.

[2] E. Sevick-Muraca, J. Houston, and M. Gurfinkel, *Current Opinion in Chemical Biology*, 2002, **6**, 642.

[3] V. Wagner, A. Dullaart, A.-K. Bock, and A. Zweck, *Nat Biotech*, 2006, **24**, 1211.

[4] J.-L. Bridot, A.-C. Faure, S. Laurent, C. Riviere, C. Billotey, B. Hiba, M. Janier, V. Josserand, J.-L. Coll, L. V. Elst, R. Muller, S. Roux, P. Perriat, and O. Tillement, *J. Am. Chem. Soc.*, 2007, **129**, 5076.

[5] D. Sherbo, E.Merzlyak, T. Chepurnykh, A. Fradkov, G. Ermakova, E. Sollovieva, K. Lukyanov, E. Bogdanova, A. Zaraisky, S. Lukyanov, and D. Chudakov, *Nature Methods*, 2007, **4**, 741.

[6] A. Burns, H. Ow, and U. Wiesner, *Chemical Society Reviews*, 2006, **35**, 1028.

[7] J. Choi, A. Burns, R. Williams, Z. Zhou, A. Flesken-Nikitin, W. Zipfel, U. Wiesner, and A. Nikitin, *Journal of Biomedical Optics*, 2007, **12**, 064007 (1.

[8] D. Larson, H. Ow, H. Vishwasrao, A. Heikal, U. Wiesner, and W. Webb, *Chemistry of Materials*, 2008, **20**, 2677.

[9] H. Ow, D. R. Larson, M. Srivastava, B. A. Baird, W. Webb, and U. Wiesner, *Nano Letters*, 2005, **5**, 113.

[10] X. Zhao, L. Hilliard, S. Mechery, Y. Wang, R. Bagwe, S. Jin, and W. Tan, *Proceedings of the National Academy of Sciences*, 2004, **101**, 15027.

[11] S. M. Moghimi, A. C. Hunter, and J. C. Murray, *Pharmacological Reviews*, 2001, **53**, 283.

[12] H. Kobyashi and M. Brechbiel, *Advanced Drug Delivery Reviews*, 2005, **57**, 2271.

[13] H. S. Choi, W. Liu, P. Misra, E. Tanaka, J. P. Zimmer, B. I. Ipe, M. G. Bawendi, and J. V. Frangioni, *Nature Biotechnology*, 2007, **25**, 1165.

[14] S. Ohnishi, S. Lomnes, R. Laurence, A. Gogbashian, G. Mariani, and J. Frangioni, *Molecular Imaging*, 2005, **4**, 172.

[15] A. Nel, T. Xia, L. Madler, and N. Li, *Science*, 2006, **311**, 622.

[16] A. V. Blaaderen and A. Vrij, *Journal of Colloid and Interface Science*, 1993, **156**, 1.

[17] G. H. Bogush, M. A. Tracy, and I. C. F. Zukoski, *Journal of Non-Crystalline Solids*, 1988, **104**, 95.

[18] S. Sadasivan, A. Dubey, Y. Li, and D. Rasmussen, *Journal of Sol-Gel Science and Technology*, 1998, **12**, 5.

[19] G. Weagle, P. E. Paterson, J. Kennedy, and R. Pottier, *Journal of Photochemistry and Photobiology, B: Biology*, 1988, **2**, 313.

[20] S. T. Hess, S. Huang, A. A. Heikal, and W. W. Webb, *Biochemistry*, 2002, **41**, 697.

[21] E. Herz, H. Ow, D. Bonner, A. Burns, and U. Wiesner, *J. Am. Chem. Soc.*, 2008, **submitted**.

[22] L. Song, E. J. Hennink, I. T. Young, and H. J. Tanke, *Biophys. J.*, 1995, **68**, 2588.

[23] W. Cai, K. Chen, Z.-B. Li, S. Gambhir, and X. Chen, *Journal of Nuclear Medicine*, 2007, **48**, 1862.

[24] L. C. Drickamer, *Journal of Chemical Ecology*, 1995, **21**, 1481.

[25] G. Hermanson, 'Bioconjugate Techniques', Academic Press, 2008.

[26] M. Piatyszek, A. Jarmolowski, and J. Augustyniak, *Anal. Biochem.* , 1988, **172**, 356.

[27] B. Beattie, G. Forster, R. Govantes, C. Le, V. Longo, P. Zanzonico, L. Bidaut, R. Blasburg, and J. Koutcher, *Molecular Imaging*, 2007, **6**, 108.

# CHAPTER 6

# CONCLUSIONS AND OUTLOOK

## *6 Conclusions and Outlook*

The facile and diverse chemistry of silica, along with its innate biocompatibility and chemomechanical robustness make it an excellent materials platform for the development of probes for biological and biomedical applications. In particular, core-shell silica nanoparticles have been shown to be an excellent host material for organic dye molecules for the development of fluorescent probes, generating marked enhancements in the photophysical properties of the encapsulated dyes[1,2], as well as allowing the synthesis of multifunctional and/or multimodal probes[3]. This dissertation has explored two facets of the core-shell silica nanoparticle architecture, namely the development of quantitative ratiometric sensor nanoparticles, and the optimization of the core-shell architecture for *in vivo* applications and potential translation to clinical practice. This conclusion outlines the current state of these fields and discusses some of the remaining challenges and opportunities for these materials.

Recently published work from the Wiesner group elucidated some of the mechanisms of the photophysical enhancements that are hallmarks of the C Dot core-shell silica nanoparticle architecture as discussed in Chapter 1[2]. Specifically, local environment of the dye molecules was varied systematically and a comprehensive photophysical analysis was made of each. Analysis of fluorescence lifetime data revealed that encapsulation of dye in the silica matrix resulted in a suppression of non-radiative decay (*e.g.* isomerization, electron-transfer) along with an increase in the radiative decay rate. The radiative rate increase is consistent across all particle

architectures and may be due to the high local dielectric constant of the silica, compared to the surrounding medium. The non-radiative rate decrease scales with the rigidity of the local surroundings of the dye as measured by rotational anisotropy. For architectures with high-silica and low organic content (high rigidity), the non-radiative reduction was up to 3x higher than in low-silica, high organic content (low rigidity) environments yielding more photoefficient particles[2]. These findings have implications for both the probe particles, as well as the dual-emission sensor particles, where the local environment must be tuned to ensure adequate sensitivity, while ensuring photostability and enhancing per particle brightness.

The quantitative ratiometric sensing demonstrated in Chapters 2, 3 and 4 of this work demonstrates the capability and potential of the ratiometric sensing technique to generate high resolution maps of chemical microenvironments both intra- and extracellularly.

One of the outstanding issues is the balance between the high signal-to-noise ratios needed to effectively reconstruct local chemical gradients and the high speed at which some signaling events occur. In confocal imaging, multiple line averages are often necessary to ensure adequate sensitivity for both calibration and imaging, but these averages take time that could be used to visualize fast (millisecond) events. The balance between image speed and quantitation must be evaluated for each application, and for many applications a semi-quantitative or qualitative measure of the local environment may be sufficient. In either case, the photophysical enhancements conferred by silica encapsulation generate brighter and more photostable probes for imaging. As both sensor and imaging technologies continue to improve, sensitivity will increase and high-resolution maps of chemical microenvironments in multiple dimensions (including time) will become more feasible.

In Chapter 5, 3-6nm diameter fluorescent silica nanoparticles were shown to exhibit fast and efficient renal excretion as well as high brightness and photostability, making them an excellent candidate for *in vivo* imaging studies and potentially as clinically relevant imaging agents. Earlier collaborative work on core-shell silica nanoparticles as *in vivo* imaging agents demonstrated 30 nm diameter silica particles as effective probes for clinically relevant tasks such as sentinel lymph node mapping, using the particles to visualize lymphatic drainage following sub-cutaneous injection[4].

One remaining challenge that must be addressed is targeting. Many biomolecules have been demonstrated as both *in vitro* and *in vivo* targeting agents, such as antibodies and aptamers. To ensure efficient renal excretion of any targeted contrast agent, the contrast agent / targeting agent construct must remain below the renal filtration threshold of ~7 nm diameter. Thus, for *in vivo* probes, small targeting agents such as peptides (*e.g.* RGD) would be ideal. Many oligo-peptide sequences have been developed based on the key protein sequences of proteins and antibodies used for binding *in vivo*. Further, the chemistry for attaching such oligopeptides to silica nanoparticles has already been established in prior work. For example, amino acids 48-57 of the trans-activating transcriptional activator (TAT) sequence from HIV-1 have been shown to confer cell-penetrating capabilities to silica nanoparticles *in vitro* as demonstrated in mouse prostate carcinoma cells in Figure 6.1[4].

Silica is an extremely versatile material and an excellent host for many different functional materials, and has shown itself especially effective for the development of high-performance fluorescent nanoparticles. One of the benefits of using a host material like silica is the potential to incorporate many different functional materials into individual particles. Beginning with the co-localization of imaging with chemical sensitivity, this concept can be expanded to incorporate alternative imaging and/or sensing modalities (*e.g.* MRI or PET), as well as potential

therapeutic capabilities. As discussed in Chapter 1, these "lab on a particle" and "single particle laboratory" architectures may be realized using silica as a host material and could enable advancements in understanding disease states as well as the processes behind their treatment.

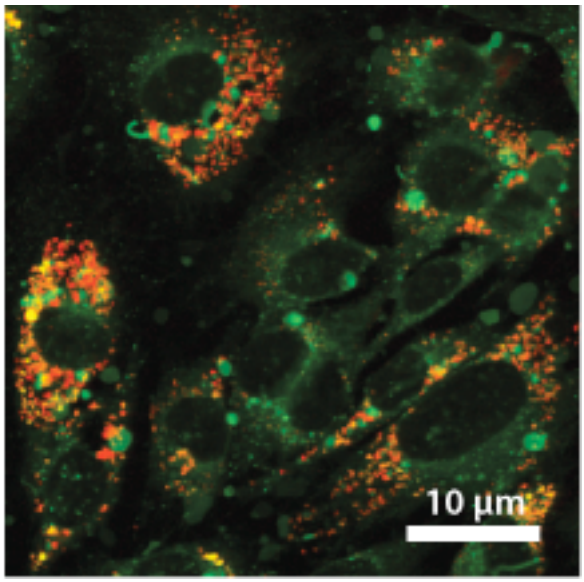


Figure 6.1 - Mouse prostate carcinoma cells labeled with C dots (red) functionalized with the cell-penetrating HIV-1 TAT oligopeptide, used to trace cell position, counterstained with DiO membrane stain (green) to visualize membrane structure

# REFERENCES


[1] H. Ow, D. R. Larson, M. Srivastava, B. A. Baird, W. Webb, and U. Wiesner, *Nano Letters*, 2005, **5**, 113.

[2] D. Larson, H. Ow, H. Vishwasrao, A. Heikal, U. Wiesner, and W. Webb, *Chemistry of Materials*, 2008, **20**, 2677.

[3] A. Burns, H. Ow, and U. Wiesner, *Chemical Society Reviews*, 2006, **35**, 1028.

[4] J. Choi, A. Burns, R. Williams, Z. Zhou, A. Flesken-Nikitin, W. Zipfel, U. Wiesner, and A. Nikitin, *Journal of Biomedical Optics*, 2007, **12**, 064007

# APPENDIX A

## Supplementary Information for Chapter 2

### *A.1. Sensor Particle Calibration:*

The pH sensitivity of these particles (Figure 2.2) was determined based upon the ratio between the peak sensor intensity (fluorescein: 520nm at 488nm excitation) and the peak reference intensity (rhodamine: 575nm at 540nm excitation) in a series of sodium phosphate buffers from pH 5.0 to 8.5.

### *A.2. Confocal Microscopy:*

All fluorescence microscopy was conducted using separate excitation lines for green (488nm) and red (543nm) of an Argon ion laser using a 63X 0.9 NA water immersion objective. In each instance, emission was collected sequentially for green (500-545nm) and red (555-615nm) channels as well as a bright field image, which were subsequently background corrected, analyzed and overlaid in MATLAB 6.12 and Adobe Photoshop 7.0. For each cell experiment a minimum of ten cells were individually imaged to ensure a representative image is shown.

### *A.3 Cell Handling Protocols:*

RBL-2H3 cells were maintained in monolayer cultures and harvested with trypsin-EDTA (Life Technologies, Rockville, MD) 3–5 days after passage. Prior to harvesting, cells were labeled with AlexaFluor®488-labeled Cholera Toxin B (5 mg/ml, 37ºC) for half an hour and then washed to remove the unbound cholera toxin. The cells were resuspended in 1mg/ml BSA in BSS (BSA-BSS) at a density of $5x10^6$ cells/ml and then incubated with $1.6x10^{11}$/ml of 70 nm sensor (Figure 2.4) or analogue

(Figure 2.3) particles for 1 hour at 37ºC. To induce endocytosis, cells were treated with Phorbol dibutyrate (5µg/ml, 20 min, 37ºC) during the incubation with particles. The cells were then washed thrice with BSA-BSS and plated in 35-mm Petri dishes with coverglass bottom (0.16–0.19 mm; MatTek, Ashland, MA) at $1.25x10^5$ cells/ml and visualized by confocal microscopy.

# APPENDIX B

## Supplemental Information for Chapter 4

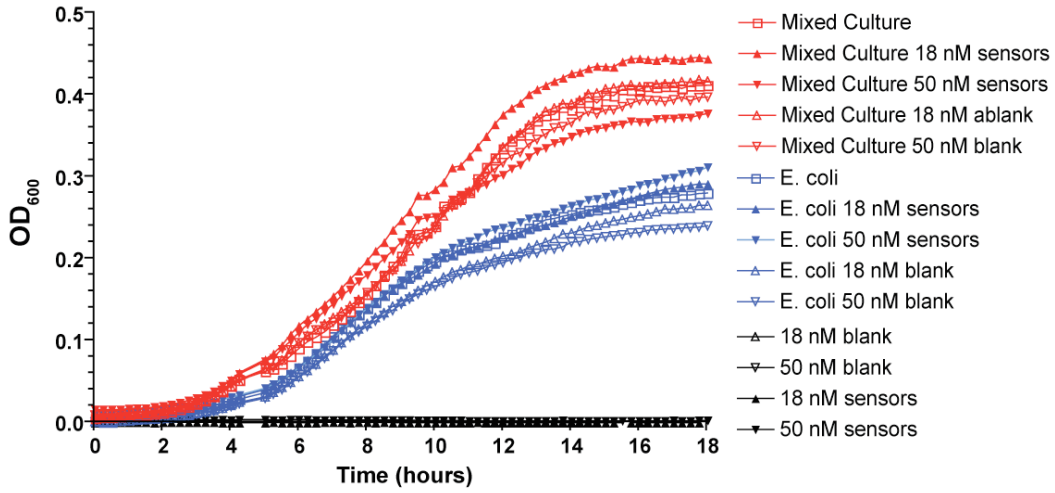


Figure B.1 Concentration-dependent growth curves for E. coli and mixed cultures. Demonstrates the minimal perturbations induced in the microbial environment by addition of 10 nm diameter bare silica sensors (filled) and 10 nm diameter bare silica particles without dye (outline) at 18 and 50 nM in E. coli (blue) and wastewater (red) cultures along with sterile controls (black).

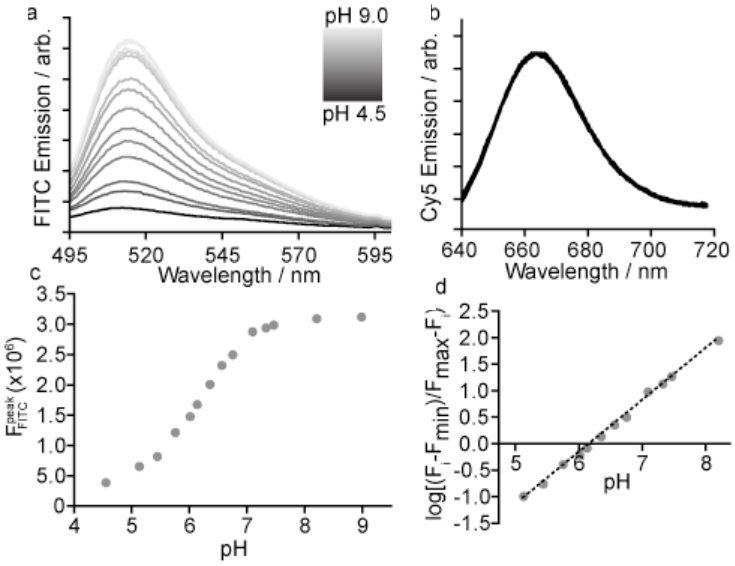


Figure B.2 Spectrofluorometric Calibration of C Dot Sensors. a, sensor and b, reference emission spectra upon excitation at 488 and 638 nm, respectively in calibration buffers of varying pH. c, plot of pH versus peak intensity ratio ($F_i = I_{FITC} / I_{Cy5}$) and d, a modified Henderson-Hasselbalch analysis (Eq. 4.1) of the data used to generate the calibration curve used in Figures 4.2 b and d.

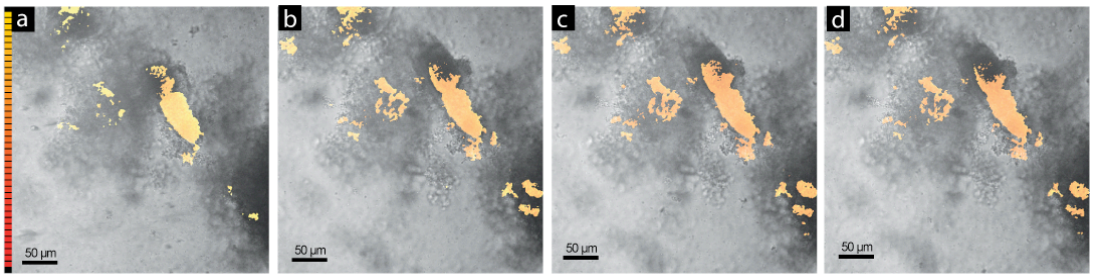


Figure B.3 Time-resolved *in situ* pH measurements in biofilms. pH imaging post injection of 90 mM glucose to biofilms to *E. coli* PHL628 at 0, 30, 60 and 90 minutes post injection. (Color scale corresponds to pH values from 4 to 8)

Matlab Files (background, calibration, volumetric and time-resolved m-codes)

```
%Background image analysis and averaging of WW Image Settings 041608
%for Leica Confocal Images 512x512 12-bit
%ww Image Settings => PMT2=X, PMT3 = X
%input = images
%output = averages & standard deviations of whole images
%         averaged images

%read in filenames
filesg = dir('*backgd *00.tif');        % green images from ch00
filesr = dir('*backgd *01.tif');        % red images from ch01

%set zeros
cg=double(zeros(512,512));
cr=double(zeros(512,512));
c=double(zeros(512,512));
avg24=double(zeros(1,2));
stdev24=double(zeros(1,2));

%read in images
    for k=1:numel(filesg);
       c=double(imread(filesg(k).name));   %read in green image files
        cg=cg+medfilt2(c);                  %add up pixel values after
                                            %median filtering (remove high
                                            %variance noise)
        c=double(imread(filesr(k).name));
        cr=cr+medfilt2(c);
    end
%divide sums by number of images
cr=cr/(numel(filesr));
cg=cg/(numel(filesg));

%compute averages & save
avg24(1,1)=mean(nonzeros(reshape(cg,262144,1)));
avg24(1,2)=mean(nonzeros(reshape(cr,262144,1)));
stdev24(1,1)=std(nonzeros(reshape(cg,262144,1)));
stdev24(1,2)=std(nonzeros(reshape(cr,262144,1)));

%upconvert and output images
imwrite(uint16(cg*16),'bgWW8g.tif');
imwrite(uint16(cr*16),'bgWW8r.tif');
```

```
%Calibration Analysis for WW8 Imaging Settings
%for Leica Confocal Images 512x512 12-bit
%WWImage Settings
%ww Image Settings => PMT2=X, PMT3 = X
%input = images
%output = averages & standard deviations of different pH calibration solns
%         averaged ratiometric images

%set zeros
cg=double(zeros(512,512));                      %holder for green,
bg=double(zeros(512,512));                      %background for green
cr=double(zeros(512,512));                      %holder for red
br=double(zeros(512,512));                      %background for red
c=double(zeros(512,512));                       %intermediate result file
CavgWW8=double(zeros(1,19));                    %average
CstdevWW8=double(zeros(1,19));                  %stdev over average image
Cmax=double(zeros(1,19));               %max of each ratio image
Cmin=double(zeros(1,19));               %min of each ratio image
j=0;k=0;a=0;ratio=0;                    %index counters & various variables

%Read in filenames
filesg=[dir('*phlow*ch00*.tif'),dir('*ph01*ch00*.tif')...dir('*phhi*ch00*.tif')];
%green files from ch00
filesr=[dir('*phlow*ch01*.tif'),dir('*ph01*ch01*.tif')...dir('*phhi*ch01*.tif')];
%red files from ch02
bg=double(imread('bgWW8g.tif'))/16;         %read in background green
br=double(imread('bgWW8r.tif'))/16;         %read in background red

%Read in images
    for a=1:19;
        j=20-a;  j                          %show counter progress (adjust for # calib
points)
        cg=double(zeros(512,512));          %re-zero green before each image read
sequence
        cr=double(zeros(512,512));          %re-zero red before each image read sequence
        c=double(zeros(512,512));
        for k=1:3
            c=double(imread(filesg(k,j).name));     % read in green images
            cg=cg+medfilt2(c)-br;                  %add successive green images and
                                                    %subtract avg background
            c=double(zeros(512,512));
            c=double(imread(filesr(k,j).name));
            cr=cr+medfilt2(c)-br;
            c=double(zeros(512,512));
        end
    %Math on images
        cg=cg/3;                                %divide by number of added images
        cr=cr/3;
        c=medfilt2(cg./cr);    %determine pixel-wise ratio
        Cmax(1,j)=max(max(c)); Cmin(1,j)=min(min(c));
    %Upconvert and export images
        ratio=Cmax(1,15)/64000;   %upconversion ratio number calculated from max of
highest pH sample
        imwrite(uint16(c/ratio),sprintf('calWW8_ph%02d.tif',j));  %output calibration
images
    %Avg & Stdev
        c=c(isfinite(c));
        CavgWW8(1,j)=mean(reshape(c,numel(c),1));    %determine average value across
                                                     %ratiometric image and add to
array
        CstdevWW8(1,j)=std(reshape(c,numel(c),1));   %determine standard dev across
rat.
                                                     %image and add to array

    end
```

```
%Volumetric Image Analysis for WW8 Imaging Settings
%for Leica Confocal Images 512x512 12-bit
%%ww Image Settings => PMT2=X, PMT3 = X
%input = images
%output = averages & standard deviations of different pH calibration solns
%         averaged ratiometric images
%This file is for non-z-series data as it averages over all images (which
%are assumed to be coplanar)

%set zeros
cg=double(zeros(512,512));              %holder for green
bg=double(zeros(512,512));              %background for green
cr=double(zeros(512,512));              %holder for red
br=double(zeros(512,512));              %background for red
c=double(zeros(512,512));               %intermediate result file
j=0;k=0;a=0;ratio=0;                    %index counters & variables

%Read in filenames
filesg = [dir('*ch00*.tif')];
%green files from ch00
filesr = [dir('*ch01*.tif')];
%red files from ch01
bg=double(imread('bgWW8g.tif'));
br=double(imread('bgWW8r.tif'));
threshold=median(median(br));
meansalt=double(zeros(numel(filesg),1));
bob = double(zeros(512,512));
avgg = double(zeros(numel(filesg),1));
avgr = double(zeros(numel(filesg),1));
ratio=X;                                %upconversion ratio number calculated
                                        %from max of highest pH sample
%Generate pH scalebar
bob = double(zeros(512,10));
blank = bob;
    for i = 1:41
        for j=1:11
            bob((12*i+j),:) = (3.9+0.1*i);
        end
    end

%Read in images
    for a=1:numel(filesg);
        a                               %show counter progress
        cg=double(zeros(512,512));      %re-zero green before each image read sequence
        cr=double(zeros(512,512));      %re-zero red before each image read sequence
        c=double(zeros(512,512));
        c=double(imread(filesg(a).name));
        cg=medfilt2(c)-bg;                %add successive green images
                                        %and subtract avg background
        c=double(zeros(512,512));
        c=double(imread(filesr(a).name));
        cr=medfilt2(c)-br;                %add successive red images
                                        %and subtract avg background
        c=double(zeros(512,512));
        avgg(a,1)=mean(nonzeros(cg));
        avgr(a,1)=mean(nonzeros(cr));

        %Math on images
        for j=1:512
            for k=1:512
                g=cg(j,k);
                r=cr(j,k);
                b=((g/r-Fmin)/(Fmax-g/r));

                if (r > threshold) && (b>0)
                    % Analysis of green 1 channel vs red 1 channel gives:
                    %

                    c(j,k) = Slope*log(b) + Intercept;
                    %r
                else
```

```
                c(j,k) = 0;
                %k
            end
        end
    end

%Upconvert and export images including pH bar

    imwrite(uint16([bob,blank,c]/(ratio)),sprintf('WW%03d.tif',a));
end
```

```
%Time-resolved Image Analysis for WW8 Imaging Settings
%for Leica Confocal Images 512x512 12-bit
%WW8 Image Settings
%ww Image Settings => PMT2=X, PMT3 = X
%input = images
%output = averages & standard deviations of different pH calibration solns
%         averaged ratiometric images
%This file is for non-z-series data as it averages over all images (which
%are assumed to be coplanar)

%set zeros
cg=double(zeros(512,512));              %holder for green
bg=double(zeros(512,512));              %background for green
cr=double(zeros(512,512));              %holder for red
br=double(zeros(512,512));              %background for red
c=double(zeros(512,512));               %intermediate result file
j=0;k=0;a=0;ratio=0;                    %index counters & variables
bob = double(zeros(512,10));
blank = bob;

%Read in filenames
filesg = [dir('*t00*ch00*.tif'), ... dir('*tfinal*ch00*.tif')];
%green files from ch00
filesr = [dir('*t00*ch01*.tif'), ... dir('*tfinal*ch01*.tif')];
%red files from ch01
bg=double(imread('bgWW8g.tif'));
br=double(imread('bgWW8r.tif'));
threshold=median(median(br))/5;      %determine what background level to use
CmaxEC1=double(zeros(4,1));
CminEC1=double(zeros(4,1));

%Read in images
for j=1:numel(filesg(1,:));
    for a=1:numel(filesg(:,j));
        cg=double(zeros(512,512));
        cr=double(zeros(512,512));
        c=double(zeros(512,512));
        c=double(imread(filesg(a,j).name));
        cg=cg+medfilt2(c)-bg;
        c=double(zeros(512,512));
        c=double(imread(filesr(a,j).name));
        cr=cr+medfilt2(c)-br;
        c=double(zeros(512,512));
    end
    %Math on images
        cg=cg/numel(filesg(:,j)); cr=cr/numel(filesg(:,j));
        for i=1:512
            for k=1:512
                g=cg(i,k);
                r=cr(i,k);
                b=((g/r-Fmin)/(Fmax-g/r));

                if (r > threshold/10) && (b>0)
                    % Analysis of green 1 channel vs red 1 channel gives:
                    c(i,k) = slope*log(b) + intercept;
                else
                    c(i,k) = 0;
                    %k
                end
            end
        end
         CmaxEC1(j)=max(max(c)); CminEC1(j)=min(min(c));
        %convert to pH


    %Upconvert and export images
        ratio=X;
    for l = 1:41
        for m=1:11
            bob((12*l+m),:) = (3.9+0.1*l);
        end
```

```
    end
        imwrite(uint16([bob,blank,c]/(1.5*ratio)),sprintf('WWt%01d.tif',j));
    %Avg & Stdev
        CmedianWW(j)=mean(nonzeros(c));
        CstdevWW(j)=std(nonzeros(c));
end
```

APPENDIX C
Supplementary Information for Chapter 5

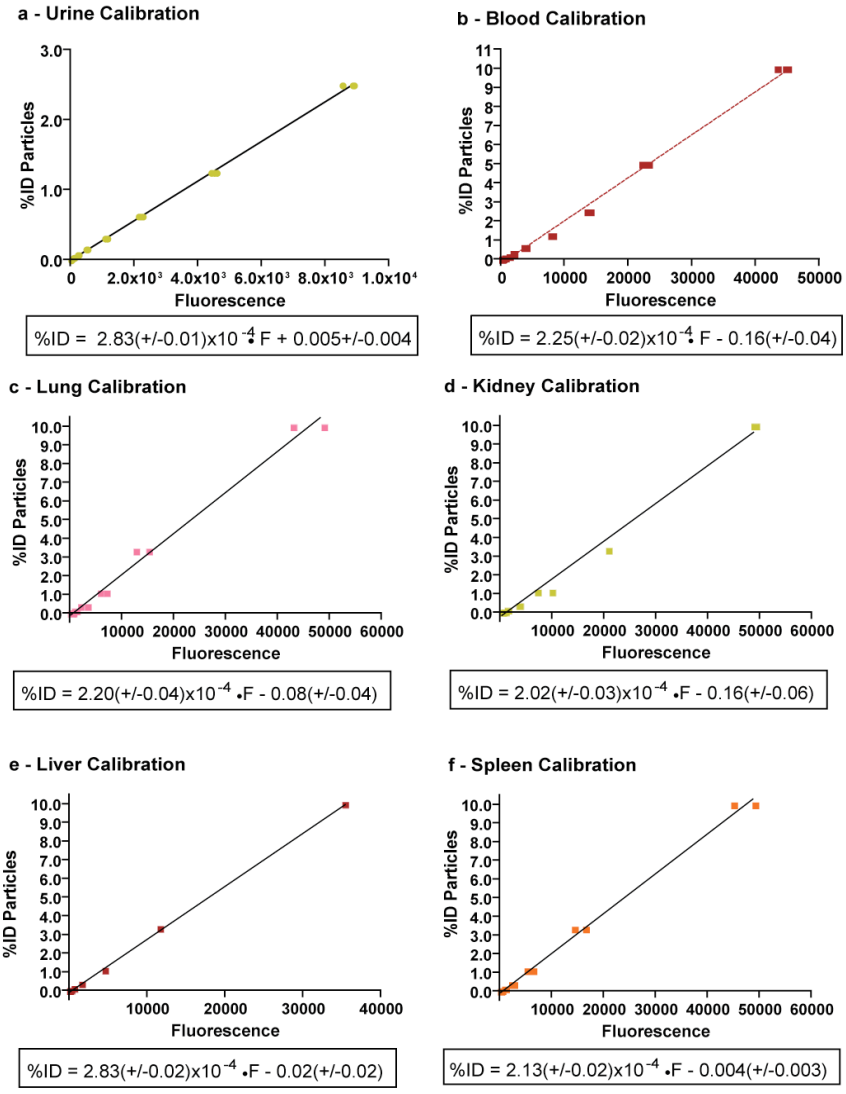


Figure C.1 - Calibration Curves. a-b. Calibration curves for urine and blood comparing %ID with the plate reader fluorescence per 384 well plate well and associated equations. c-f. Calibration curves for lung, kidney, liver and spleen comparing %ID to plate reader intensity and associated equations. For all samples fits are linear with $R^2 > 0.99$. Due to the negligible difference between emission intensity of absorption matched samples of 3.3 nm and 6.0 nm diameter particles, one set of calibration curves was generated using 3.3 nm diameter particles in physiological saline (0.15M NaCl).

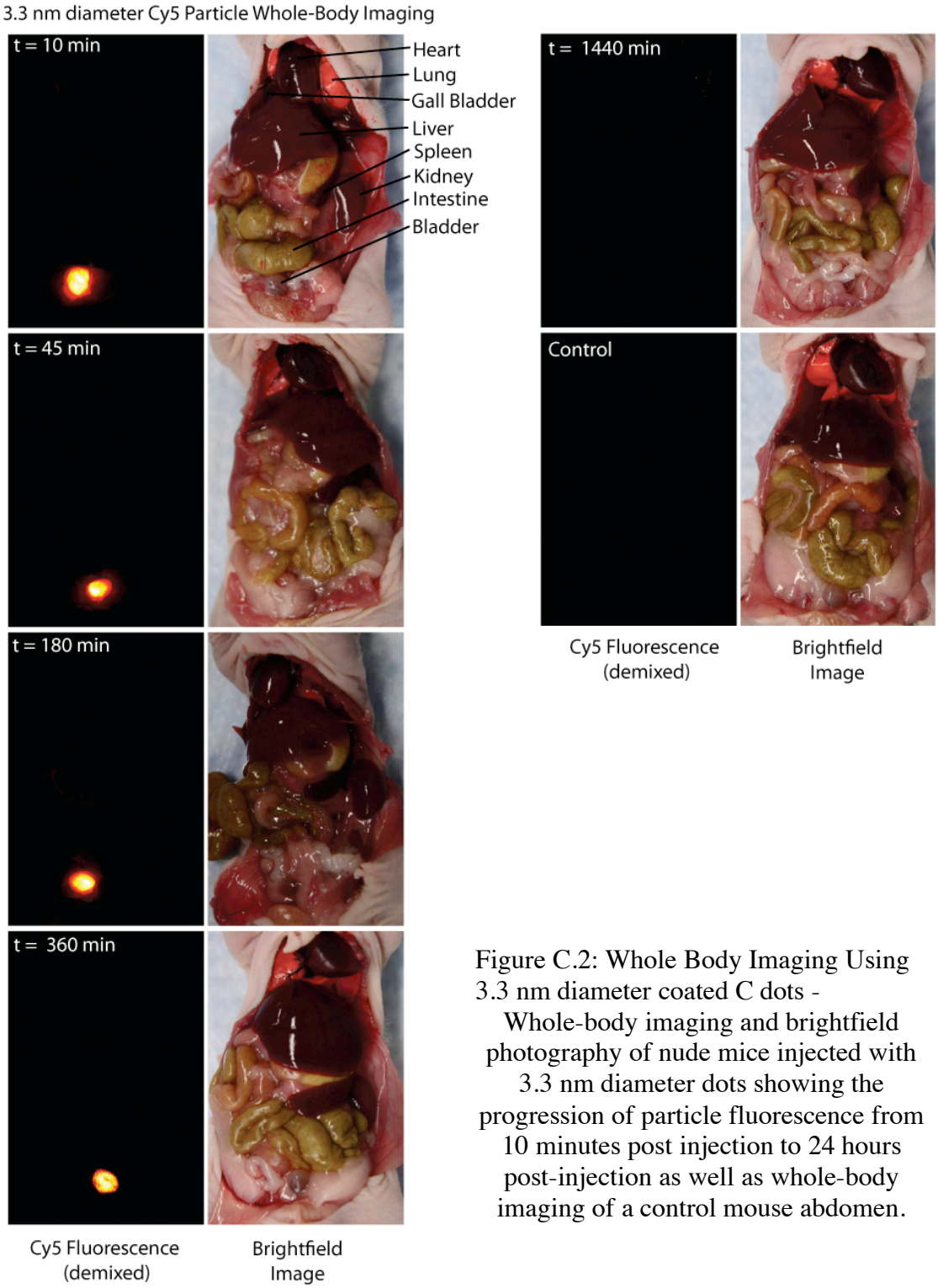


Figure C.2: Whole Body Imaging Using 3.3 nm diameter coated C dots - Whole-body imaging and brightfield photography of nude mice injected with 3.3 nm diameter dots showing the progression of particle fluorescence from 10 minutes post injection to 24 hours post-injection as well as whole-body imaging of a control mouse abdomen.

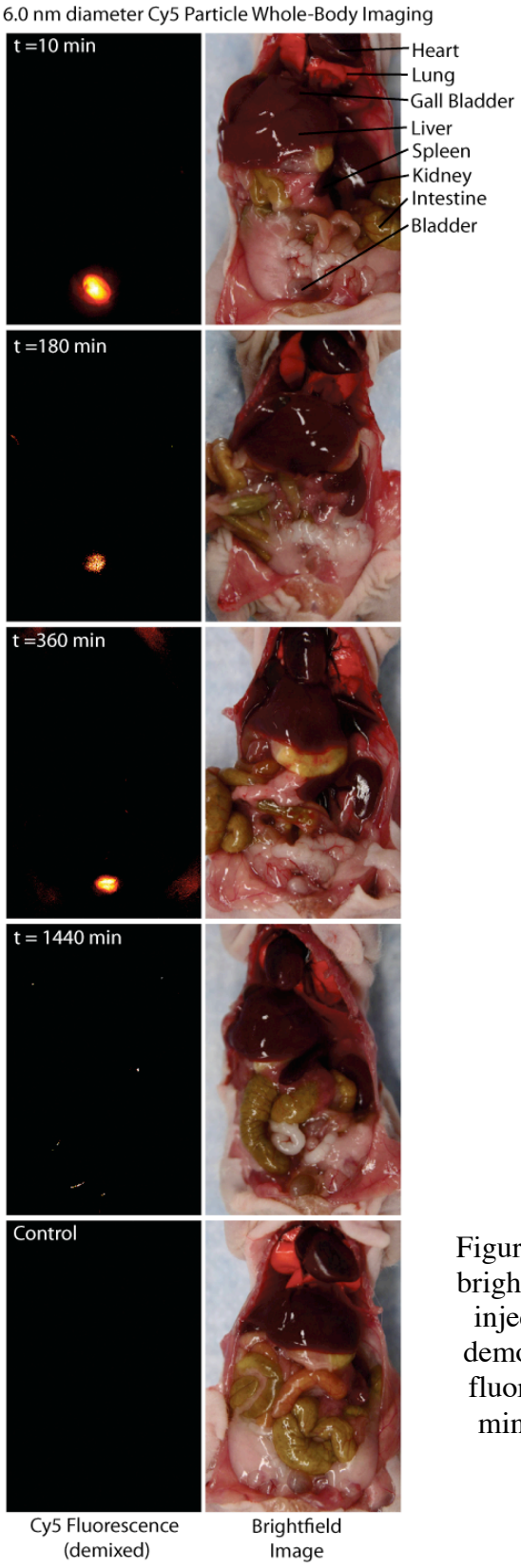


Figure C.3: Whole-body imaging and brightfield photography of nude mice injected with 6.0 nm diameter dots demonstrating the change in particle fluorescence in the bladder from 10 minutes post injection to 24 hours post-injection.

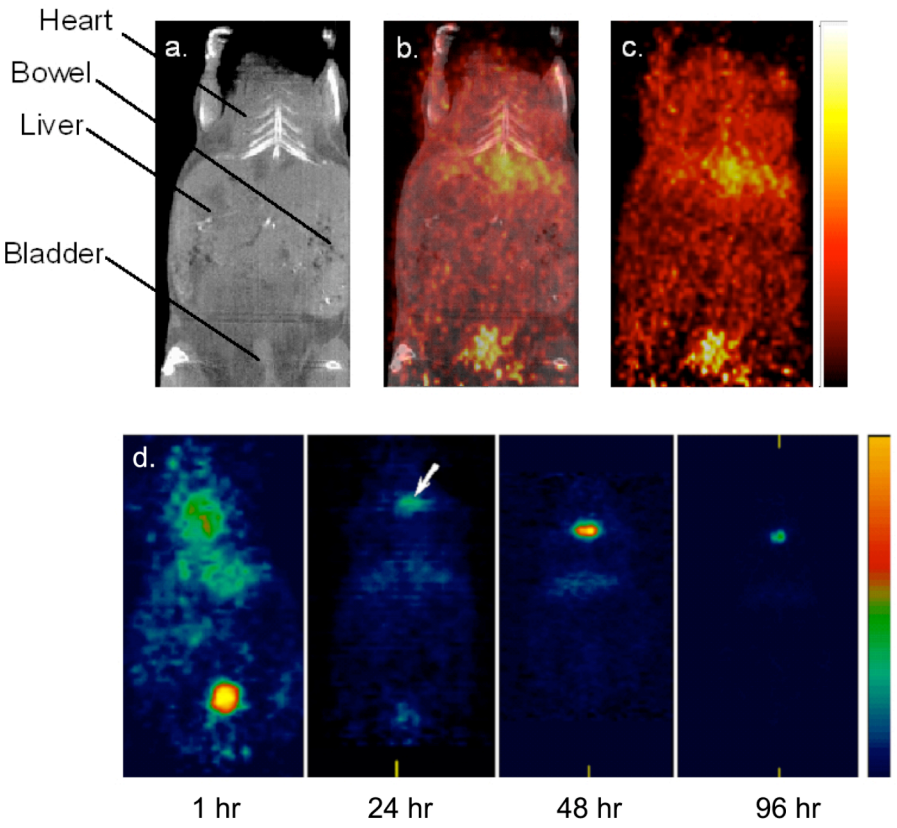


Figure C. 4 - Serial *In Vivo* Biodistribution Study Using Co-Registered PET-CT. a-c. Co-registered PET-CT image 24-hr after injection of $^{124}$I-labeled coated C-dots demonstrating a small amount of activity remaining within the bladder and overlying the liver/gastrointestinal tract (center), and flanked by the independently acquired microCT and microPET scans. d. Serial microPET images demonstrating progressive loss of radiolabeled particles over the course of a 96 hour period, with only a tiny amount or residual activity remaining in the thyroid gland (arrow) at 96 hours. Uptake of radiolabeled particles by the thyroid gland was not blocked, and demonstrated maximum uptake at 48 hours.

Table C.1 – Urine Concentration and Excretion Data

| Sample | Time (min) | Concentration (%ID/µl) | Avg. Urine Volume (µl) | Estimated %ID Excreted |
|---|---|---|---|---|
| 3.3 nm diameter | 0.0 | 0.0 | 0.0 | 0.0 |
| | 10 | 0.28 +/- 0.04 | 6.94 | 1.05 |
| | 45 | 0.30 +/- 0.05 | 31.25 | 8.565 |
| | 180 | 0.26 +/- 0.05 | 125 | 36.84 |
| | 360 | 0.04 +/- 0.01 | 250 | 56.83 |
| | 1440 | 0.02 +/- 0.01 | 1000 | 70.55 |
| | 2880 | $7.8(+/- 0.5) \times 10^{-4}$ | 2000 | 73.04 |
| 6.0 nm diameter | 0.0 | 0.0 | 0.0 | 0.0 |
| | 10 | 0.30 +/- 0.1 | 6.94 | 1.053 |
| | 180 | 0.07 +/- 0.02 | 125 | 22.78 |
| | 360 | 0.06 +/- 0.01 | 250 | 30.89 |
| | 1440 | 0.01 +/- 0.001 | 1000 | 58.82 |
| | 2880 | 0.01 +/- 0.002 | 2000 | 64.27 |